

Physical Properties of Nanomaterials

Juh Tzeng Lue

Department of Physics, National Tsing Hua University, Hsin Chu, Taiwan

CONTENTS

1. Introduction
 2. Physical Properties
 3. Nanodevices
 4. Conclusions
- References

1. INTRODUCTION

Nanomaterials and Nanotechnologies attract tremendous attention in recent researches. New physical properties and new technologies both in sample preparation and device fabrication evoke on account of the development of nanoscience. Various research fields including physics, chemists, material scientists, and engineers of mechanical and electrical are involved in this research. In this review various methods of preparing nanomaterials including insulators, semiconductors, and metals are discussed. We express the exotic physical properties concerning the linear and nonlinear optical spectra, temperature dependence of resistivities, spin resonance spectra, and magnetic susceptibility measurements. A number of fascinating and provocative results have been developed that lead our perspective understanding of quantum tunneling, quantum phase transition, surface effect, quantum size-effect confinement and nonlinear susceptibility enhancements.

1.1. Sample Preparation

The first discovered nanomaterials was prepared by vacuum evaporation of iron in inert gas and condensed in cooled substrates [1]. After then many methods to fabricate nanoparticles including inorganic ceramics and organic compound are developed, such as arc plasma torch to produce metallic powder [2, 3], laser induced chemical vapor deposition method (CVD) to produce special compounds [4], and microwave plasma enhanced CVD to produce hard and brittle materials. Instead of chemical vapor, the liquid co-precipitation can produce single-phase compounds [5] and the solid-state thermal decomposition can produce single-phase oxide metals [6]. Some specified methods are illustrated.

1.1.1. Metallic Nanoparticles

Various methods in preparation metallic nanoparticles invoke different properties with desired purposes. The widely exploited methods are:

The sol-gel method [7]: Silver nanoparticles, for example, is prepared by mixing the AgNO_3 solution with tetraethylorthosilicate ($\text{Si}(\text{OC}_2\text{H}_5)_4$, TEOS), ethanol and water then with a few drops of HNO_3 as a catalyst. The mixed solution was dispersed and dried. The dried gels were reduced at a temperature of 400°C for 30 min in hydrogen gas. The Ag particles have a size of about 5~10 nm with a profile distribution in the form of lognormal distribution. The nanoparticles are embedded in silica glass in well-separated and protected matrix. The preparation of iron nanoparticles embedded in glass can be prepared with the same method by substituting FeCl_3 for the silver salt [8-10]. The sol-gel method has advantages of yielding high purity, isotropic, and low temperature annealing while with shortage of cracking after dried by heavy doping. The free water absorbed in the porous gel and the H—O bonds desorbed on the porous surface or the chemical absorbed hydroxyl groups which affects the optical absorption within the wavelengths of 160~4500 nm can be removed by high temperature sintering.

Hydrosol/magnetic fluid method: The pure metallic suspension particles such as noble metals can be prepared by hydrosol method by using reducing agent to embed in protective gelatin [11]. The advantage of the hydrosol method is that relatively narrow size distribution with average diameter of 20 \AA can be achieved. The magnetic fluid with Fe_3O_4 particles surrounded by oleic acid as surfactant for protection from their aggregation and dispersed in water can be prepared as described in Refs. [12, 13].

Vacuum deposition method: The presence of inert gas in vacuum chamber and lowering down the substrate temperature to liquid nitrogen temperature during thermal evaporation can reduce the momentum of the evaporated metallic atoms or clusters by collision with gas to obviate their further aggregation on the substrate. The evaporated metal atoms condensed just at where they reached without migration to the potential minimum thereby lose van der attraction between particles. The resulting smokes can be collected from the substrate or walls of the evaporation

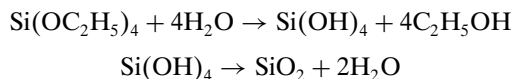
chamber with the particle sizes can be easily controlled between 30~1000 Å depending on the gas pressure, the evaporation speed, the type of gas used, and the substrate temperature [14–15]. Direct (DC) or radio frequency (RF) sputtering with the structure of deposited films mostly to be amorphous without substrate heating can successfully deposit refractory metals and alloys.

Ball milling method: Hard and brittle ceramic materials can be ball-milled into nanoparticles to produce nanocrystals, noncrystals, and pseudocrystals. Powders of 500 nm sizes can be milled into several nm by strong vibrations when mixed with tungsten-carbide (WC) spheres. The shortages of ball milling are the surface contamination of the products and nonuniformity of the structure but is a simple method. Sometimes an addition of 1~2% of methanol or phenol can prevent diffusion and solid reaction of the nanoparticles.

1.1.2. Nanoparticles: Insulators

Silicon dioxide is popularly distributed on the earth. The crystalline and non-crystalline forms of silicon dioxides are well known to be named as quartz and fused silica, respectively. The interface of amorphous silica had been extensively investigated since silica surfaces play important roles in catalysis, chemical reactions, and micro electronic fabrications. A meticulous study of the optical properties of amorphous silica surfaces is crucial for the accessing of more pragmatic applications of these well pervasive materials.

The sol-gel technique has been implemented to prepare silver nanoparticles and silica nsnaospheres [16]. This method involves the hydrolysis of salts. Ultra pure or homogeneous multi-component glasses can be made by sintering at a temperature well below the liquid temperature of the system. The process usually begins from alkoxide compounds through hydrolysis and polycondensation at room temperature. One particular example is the reaction of tetraethylorthosilicate (TEOS), $\text{Si}(\text{OC}_2\text{H}_5)_4$, ethanol and water. These three reactants form one phase solution after stirring. The fundamental reactions of sol-gel process are shown below.



In practice, water drops of 4 to 20 mols are introduced per mol of TEOS to assure the complete hydrolysis. When a sufficient number of interconnected Si–O–Si bonds are formed in a region, they interact cooperatively to form colloidal particles, or a sol. Sedimentation for several days, the colloidal particles link up to form a three-dimension network. There are many studies on the effects that the addition of acid or base catalyzes the process and leads to gels with different structures and morphologies. Acid-catalyzed ($\text{PH} \sim 2$) forms linear polymers that entangle together resulting in gelatin. Base-catalyzed ($\text{PH} > 11$) forms more branch clusters. In general, acid-catalyzed gels are transparent, while base-catalyzed solutions are cloudy.

The major drawback to the sol-gel method is the problem of fracturing due to extended shrinkage during the drying of the gel. The heating of a gel at a very slow rate is one way of avoiding fracture. A more effective technique is

to hold the gel isothermally at the appropriate temperature to allow the reactions to complete before going ahead to the next step. Lochhead and Bray [17] introduced a simple drying and densification process. The samples, after gelatin, were sealed and stored at 60° for two days. Then they were dried by slowly ramping the temperature at (5°/h) to 90° and keeping at that temperature without sealing for two days. Ramping the temperature at 1°/min to 200, 400 performed subsequently thermal densification, and 600° with one-day dwell time at each temperature. Finally the samples were heated to 800 and 900° for 12 hours at each temperature. Nevertheless, the cracking problem was still found in some samples.

In 1968 Stober et al. [18] published a paper describing a method of making monodispersive SiO_2 particles from ammonia catalyzed TEOS. The word monodispersive refers to families of particles whose diameters only vary by a few percent. These particles can be coalesced into a close packed structure analogous to an ordinary close packed crystal. It is possible to obtain a long-range (>1 mm) ordered silica monodispersive particles so that radiation can be diffracted from them. Many researchers have tried to explain the process that leads to a largely monodispersive particles. Among them Bogush and Zukoski [19] suggested that after the initial formation of small clusters by the reactants, the formation of larger particles take place by the aggregation of these small clusters.

Mayoral et al. [20] used sedimentation to assemble monodispersive SiO_2 spheres and to form ordered structures. The sedimentation takes place over a period of up to several weeks. Regular close packed structures are observed by scanning electron microscopy (SEM) and atomic force microscopy (AFM). The structure is face centered cubic aligning (111) faces parallel to the substrate surface. The sedimentation structures have little mechanical strength. However it can be sintered at temperatures of the order of 900°. This has the effects of forming a neck joining between adjacent spheres and reducing lattice parameter as much as 10%. It is difficult to control the sedimentation of deposition. The sedimentation rate depends on gravity and viscosity of the solution so that the velocity of the particles is proportional to the square of their diameters. For particles having a diameter less than about 300 nm, the process is extremely slow whereas particles have a diameter larger than 550 nm, the process is too fast to form a proper ordered structure.

On the other hand, Karmakar et al. [21] used acid-catalyzed TEOS and produced glass-like silica micro spheres, density in the ranges 2.10~2.16 g/cm³. In contrast to the Stober process, the monodispersive spheres obtained are porous silica particles. The size of the microspheres varies in the range of 10~60 μm. The sizes and size distributions are difficult to control. In addition, the particles are connected one another by necks. They can be separated from one another by washing with ethanol and acetone successively. Moran et al. [22] reported the synthesis of silica sub-microspheres and micro spheres doped with Pr^{+3} and Er^{+3} .

Cerium-doped silica glasses that are expected to yield higher optics nonlinearity are prepared by acid-catalyzed method. The molar ratio of $\text{TEOS}:\text{H}_2\text{O}:\text{CeCl}_3 \cdot 7\text{H}_2\text{O}$ is 1:16:0.1. After the cerium salt is fully dissolved in water, small amounts of nitric acid are added until the solution

PH reached approximately <2 . TEOS is added slowly to the solution under stirring. The mixture has two phases at the initial period. After around 15 minutes of stirring, as ethanol generated by the hydrolysis reaction, the mixture becomes one phase. It is further stirred for half an hour. The clear mixture is sealed and left for a few days till gelatin. The gel is dried in air for one week and kept in desiccators for another week. It shrinks and fractures. The as-dried sample is heated in a furnace to 400, 800, and 1000°. Its colors transform from transparent to yellow, greenish-brown, and purple, respectively. When the molar ratio of Cerium Chloride is decreased to 1% the color changes to light purple. The result shows the sizes of the coated shell particles, larger than 300 nm in diameter as shown in Figure 1 [23] are larger than the original core particles.

1.1.3. Semiconductor Quantum Dots

Semiconductor quantum dots (QD) with tunable optical emission frequencies due to the quantum size confinement present the utmost challenge and point of culmination of semiconductor physics. A modified Stranski-Krastanow growth method driven by self-organization phenomena at the surface of strongly strained heterostructure driven was realized [24]. A thin layer of InAs was grown on the GaAs substrate by molecular beam epitaxy method. On account of the 7% lattice mismatch between GaAs and InAs, the strain on the interface increases as the InAs film increases, which evoke a locally three-dimensional growth of InAs to release the strain. The obtained defect-free quantum-dots yield a high efficient light emission with low laser threshold current. The surface of InAs usually overgrown an InGaAs layer to generate the emission wavelength between 1.29~1.3 μm that is usually exploited in optics communication. Patterning of quantum wells by lithography was considered to be the most straightforward way of QD fabrication, which includes the electron beam interference technique [25], focused ion beam lithograph [26], optical lithography [27], and X-ray lithograph [28]. The self-organized nanodots with controlled size, defect free, strong carrier localization, and quantum Stark effect formation on strained heteroepitaxial surface evokes an interesting applications in arrayed laser emission with desired wavelength and extremely low threshold

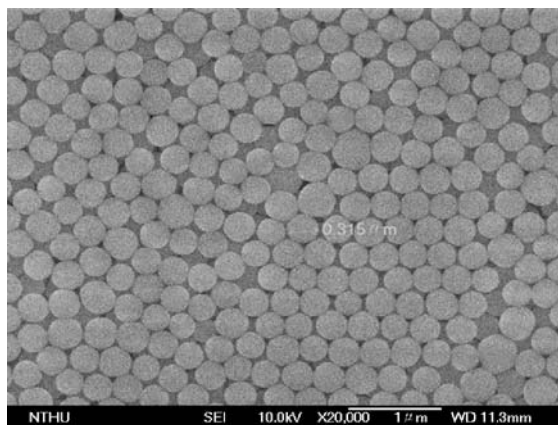


Figure 1. The SEM photographs of silica plates prepared at PH = 9.2 after 4 days.

driving current [29]. Various attempts have been demonstrated towards improving site control along multi-atomic steps [30] and the alignment of QDs along surface steps of (001) GaAs substrates disoriented a few degree toward [010], [110] directions [31]. Besides exploiting the atomic force microscopy (AFM) to characterize the quantum structure, though, the theoretical works on semiconductor quantum dots have been largely recognized, the experimental investigation was limited by insufficient technologies. Gwo's group [32] had recently developed a new silicon microlens fabrication technique utilizing the AFM gray-scale oxidation under ambient conditions. Using their AFM gray-scale oxidation technique, refractive, diffractive, and hybrid microlens profiles can be created by means of programming the oxidation voltage between the AFM tip (cathode) and the silicon substrate (anode) while scanning the tip across the surface, thus creating gray-scale surface oxide patterns for subsequent pattern transfer.

Compared with conventional photolithography or direct-writing method that uses a focused laser beam, the AFM technique can be used to fabricate microlenses with a pixel size and pitch on the order of 10 nm (two orders of magnitude improvement). In addition, by using an oxidation voltage function for a special oxide pattern, a continuous, arbitrarily shaped gray-scale structure can be built (see Figure). The greatest strength of AFM gray-scale oxidation technique is its ability to create high-resolution, arbitrarily designed micro-relief structures, which can be used as masters for replication of micro-optical elements. In the future, the throughput of this technique can be further improved by using parallel-probe arrays.

1.1.4. Magnetic Ferrite Nanoparticles

The Ag or Fe_2O_3 nanoparticles embedded in silica matrix can be prepared by the sol-gel method. The co-precipitation

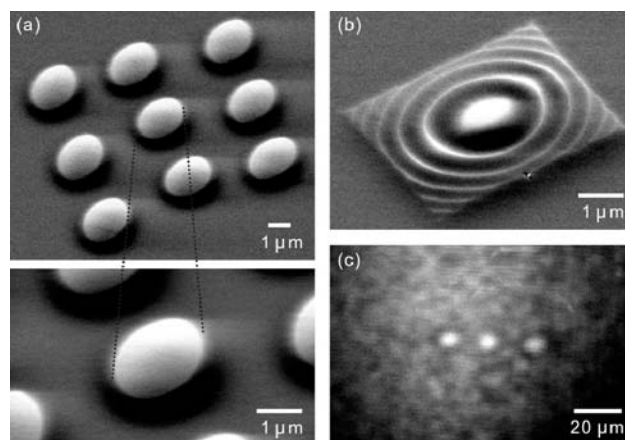


Figure 2. (a) Scanning electron micrograph. Using an atomic-force-microscope (AFM) gray-scale patterning technique, microlens arrays can be fabricated with superior focal length capability and low surface roughness values of approximately 1 nm. (b) Scanning electron micrograph. The process also allows for fabrication of unusual or arbitrarily shaped microlenses, and is difficult if not impossible to create using standard resist reflow techniques. (c) Infrared optical image of one 1×3 microlens array, confirming the focusing function of AFM-patterned Si microlenses.

method usually polls precipitates (e.g., OH^- , $\text{C}_2\text{O}_4^{2-}$, or CO_3^{2-}) into one or several soluble ionic salt solutions and waits for the precipitation of insoluble OH groups, hydrated oxides and salts. Washing out the negative complex and dehydrated thermally to yield the oxidized magnetic particles [33, 34]. The organometallic alcoholate $[\text{M}(\text{OR})^n]$ method yields products of complex oxidized metals [35] with a higher purity. Many novel electrical [36], magnetic [37], and optical [38] properties of metallic nanoparticles have been investigated recently. A synthetic technique was completed by the sol-gel method [39], which produces metallic particles embedded in glass with much uniformity in size. The complex solution was prepared by initially mixing various weights of $\text{FeCl}_3 \cdot 6\text{H}_2\text{O}$ with 4 ml of alcohol, and then adding 20 ml of tetraethylorthosilicate $\text{Si}(\text{OC}_2\text{H}_5)_4$ (TEOS) and 16 ml of deionized water and two drops of HNO_3 as a catalyst. The solution began to gel for about one day and was then dried at room temperature for one week. The dried gels were heated to 40–50 °C under the illumination of a 100 W bulb for two hours with the color changing from yellow transparent to opaque and then back to a transparent color. The FeCl_3 ions were reduced to Fe or Fe_2O_3 nanoparticles under the heat treatment in hydrogen or air at various temperatures for twenty minutes.

Magnetic nanoparticles embedded in fluids can be prepared by co-precipitation method as conventionally implemented to make ferrofluids in the past [40]. A mixture of 2 g of hydrated ferrous chloride ($\text{FeCl}_2 \cdot 4\text{H}_2\text{O}$) and 5.4 g of hydrated ferric chloride ($\text{FeCl}_3 \cdot 6\text{H}_2\text{O}$) was dissolved in 300 c.c. Hot water, in which a solution of 5 g of sodium hydroxide was added with constant stirring. Black Fe_3O_4 particles were precipitated in water with a little remnant of sodium hydroxide. By adding oil acid and heating, Fe_3O_4 nanoparticles surrounded by surfactant were aggregated after adding hydrochloric acid. Washing the precipitation with water and then adding a solvent such as cyclohexane, the ferrofluid is finally produced. Repeatedly washing to purify the precipitated nanoparticles is crucial to obtain the upgrade ferrofluids. Other spinel ferrites can be prepared by replacing FeCl_2 by NiSO_4 , MnCl_2 , or MgSO_4 . The ferrofluid of nanometer size looks apparently transparent. The shapes of most nanoparticles appear spherical, leading to non-demagnetization effect as examined by a transmission electron microscope (TEM).

1.2. Nanotubes and Nanowires

Carbon nanotube becomes one of the most promising materials in recently developed materials on account of its superior properties of rigidity, strength, elasticity, electric conductivity, and field emission. In this work we are devoted to grow multi-wall carbon nanotubes on metallic substrates for field emission, which are prospected to have pragmatic uses in display and light illumination. Most existing substrates for growth of carbon nanotubes (CNTs) by chemical vapor deposition (CVD) process are silicon wafers deposited of a thin film of transition metal catalysts on which carbons are dissolved and precipitated in hexagonally packed graphite on the cooling surface side. Different ways for producing CNTs possess different genetic characters, such as single wall, multiple wall, conducting and semi-conducting

etc., that are important items of research required in industrial applications of CNTs. Nowadays, it has not yet come to a conclusion about the real growth mechanism of CNT [41–45], even about how to adjust the size and growth density [46] and structural qualities of CNTs.

The growth mechanisms of CNTs by CVD process reported in literatures [47–48] delineate the important size effect of catalyst nanoparticles on production quality and quantity of CNTs. The size of catalyst nanoparticles deposited on substrates has a deterministic effect to produce single wall nanotubes (SWNTs). It is recognized that nanoparticles of iron group metals can dissolve more carbon elements and reduce the melting temperature. The supersaturated carbons are precipitated at the cooled contact side in corporation of curvature-induced surface tension. Buffat [49] and Gorbunov [50] reported a maximum catalyst size of 100 nm for successful growth of single wall CNTs.

The arc discharge method [43] has the advantages of mass production and an inexpensive installation while requiring laborious purification due to tremendous products. Laser ablation [44, 51] illustrates a production of high quality CNTs with a low yield and expensive equipments. The combination of the catalyst method [52] and the CVD method [53] becomes the main thrust of growing CNTs because the catalyst method can strengthen the growth and the CVD method can improve the upright alignment and simplify the products.

In the radio-frequency hot-filament chemical vapor deposition (RFHFCVD) system [54], the reactant gases are first dissociated by the microwave field before entering the chamber ensuing that CNTs can grow densely from catalyst particles ($\sim 1 \mu\text{m}$). In replacing the deposition catalyst film on silicon surface, we may implement substrates made by polished Cu–Ni and Cu–Ni–Fe–Co bulk alloys with an assistance of a radio frequency (RF) induced self bias to grow well-aligned carbon nanotubes that potentially can be exploited as electron emission [55] tips with a privilege of easy manipulation. Bunched and multi-circularly wrapped carbon nanotubes CNT are observed to grow on alloys of iron group and metal by microwave enhanced hot-filament method with a dilute gas of ammonia at a RF induced bias of -200 V . The growth of CNTs on copper based iron group alloys provides a higher resistance of erosion during high current emission with a benefit of larger heat conduction than those of conventional substates.

A copper based iron group alloy (CuM_x , $M = \text{Fe, Co, Ni}$, $x = 10\text{--}20 \text{ wt}\%$) was arc melted in vacuum furnace, well polished, and wire cut into small pieces of size $10 \times 5 \times 0.5 \text{ mm}^3$. The catalyst iron performs melting, dissolving, precipitating carbon to elongate the tube, and then sucking inside the tube to adduce the vapor-liquid-solid (VLS) growth model. The pictorial view of the VLS model growth mechanism [50] is shown in the right and left columns of Figure 3, respectively, for the presence of pure hydrogen and coexistence of ammonia. Figure 3(1) shows hydrogen etching on surface, and Figure 3(2) represent nano-catalyst particles formed and rearranged on the alloy substrate surface after hydrogen etching. Nano-catalyst particles dissolve carbon atoms are dictated in Figure 3(3) while carbon atoms are precipitated and lift-up as shown in Figure 3(4). This sophisticated growth mechanism addresses that the liquefaction of catalyst

particles is different from the conclusion of Buffat et al. [43] who illustrated that metal particles must be less than the size of 10 nm, while this result is in comply with the conclusion of Gorbunov et al. [41] expressing the catalyst size window of smaller than 100 nm.

The real growth result confirms the controllability of diameter of CNT at the growth condition as shown above except changing the growth time to 15 min and RF self-bias to -450 V with the alloy substrate being composed of Cu-10 wt% Fe-10 wt% Co-10 wt% Ni. The CNTs are about $3 \mu\text{m}$ long, and grow evenly and upright precisely on the dendrite. On the right side of Figure 4(a) where the dendrite density is higher attributing to the hydrogen etching of a higher concentration of iron based elements (Fe, Co, Ni) illustrates flourished growth of CNTs. On the left part of Figure 4(a) where the dendrite concentration of catalyst is about 50% lower than that of the right part as examined by an electron probe X-ray micro-analyzer (EPMA) showing the CNT growth rarely. The CNTs are uniformly grown with diameters of about 70 nm as shown in Figure 4(b).

A solo carbon nanotube (CNT) can also successfully be grown on nickel electrodes [56] by a microwave plasma enhanced chemical vapor deposition (MPECVD) method equipped with an impedance-matched substrate holder with the reaction gases composed of hydrogen (H_2), carbon dioxide (CO_2), and methane (CH_4) mixtures. An introduction of carbon dioxide gas before CNTs growth, the substrate temperature can easily be reached above 610°C even heated at a low microwave power. This can be enunciated from fact that carbon dioxide inherits with higher bond energy

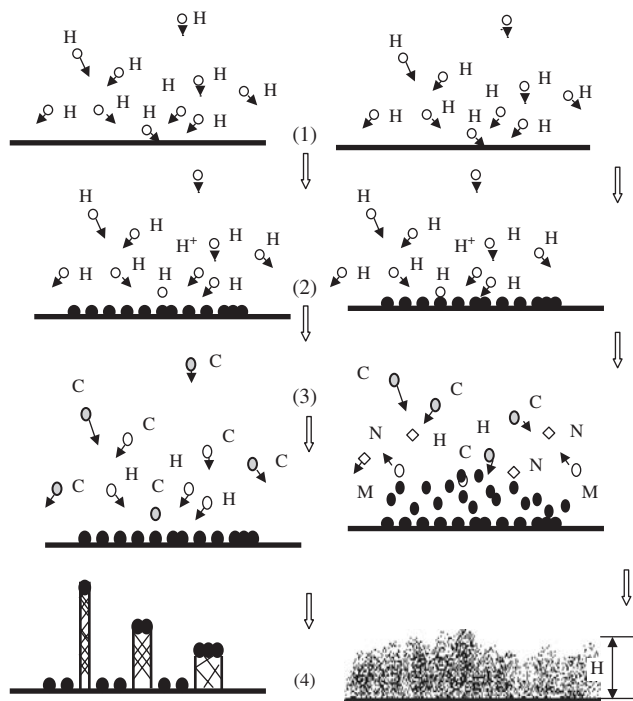


Figure 3. Pictorial mechanisms for CNT growth for dilute gas in (right column) pure hydrogen, (left column) hydrogen and ammonia. Substrates are etched at steps from up to down to produce nanostructured surface. Reprinted with permission from [50], A. Gorbunov et al., *Appl. Surf. Sci.* 197–198, 563 (2002). © 2002, Elsevier.

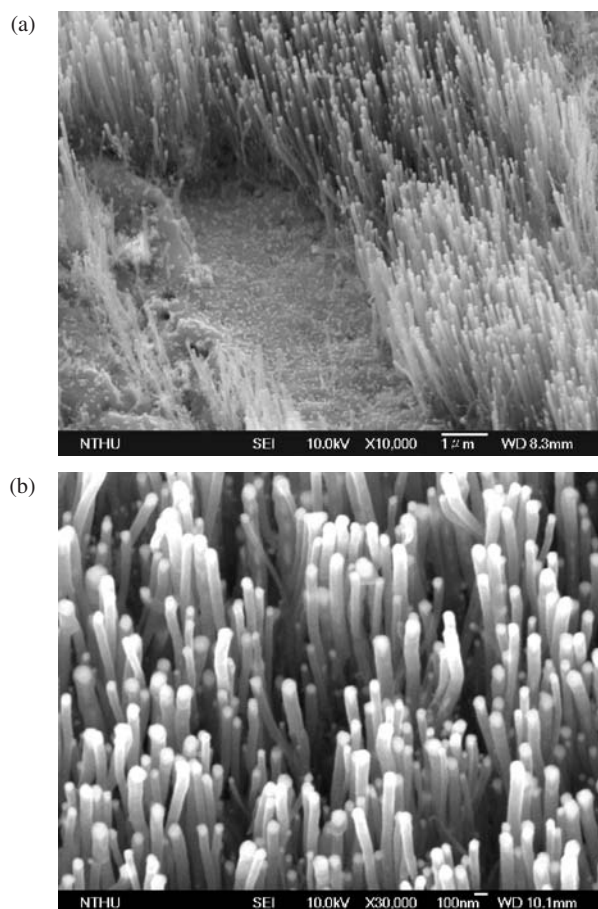


Figure 4. SEM of (a) well aligned and flourished growth of CNTs on a Cu-10 wt% Fe-10 wt% Co-10 wt% Ni bulk alloy substrate, and (b) exaggeration of the right part of (a) showing upright tubes embedded with catalyst particle at tips. Reprinted with permission from [53], S. Y. Chen et al., *J. Phys. D.: Appl. Phys.* 37, 273 (2003). © 2003, Institute of Physics.

for molecular dissociation, lower thermal conductivity, and higher heat capacity in comparing to other gases. To successfully grow CNTs with the MPECVD method under a low microwave power by introducing a passivation of carbon dioxide. The colors of the plasma balls for flow gases to be hydrogen and carbon dioxide are shown on the left and right columns in Figure 5, respectively, where the flow of carbon dioxide can sharply increase the plasma temperature to white color.

A tedious and delicate work of the SEM selected the appropriate sample with a sole CNF presenting across the gap between the electrodes as shown in Figure 6(a). The CNF was multi-connected to be firmly grown on the nickel electrodes (Fig. 6(b)), which becomes much straight as the electrode gap is reduced while with the drawback of growing multi-fibers.

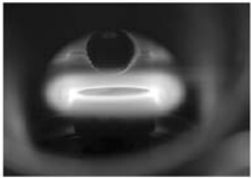
Nanotubes of length longer than $1 \mu\text{m}$ are usually called nanowires or nanofibers. They can be prepared by physics, chemistry or the mixture to produce metallic wires [57, 58], and semiconductors [59–61]. Gold nanowires can be chemically deposited in porous alumina, which was anodized improper solution, the bare gold wire is obtained by wet etching of the alumina [62]. Laser ablation on target formed

Adding CO₂: #Growth method of CNT

microwave power	100w	120w	140w	180w	200w	250w
gases ratio (sccm)						
H ₂ :40	285°C	315°C				
H ₂ :20 · CO ₂ :20		446°C	544°C	607°C	658°C	710°C
H ₂ :20 · CH ₄ :20		340°C	367°C	424°C	456°C	



H₂



CO₂

Figure 5. The colors of the plasma balls for flow gases to be hydrogen and carbon dioxide are shown on the left and right columns in Figure 4(a), respectively, where the flow of carbon dioxide can sharply increase the plasma temperature to white color. Reprinted with permission from [56], S. Y. Chen et al., *J. Nanosci. Nanotechnol.* 5, 1987 (2005). © 2005, American Scientific Publishers.

by a mixture of Si, Ni, and Co target can successfully produce silicon nanowires of diameter about 15 nm and several decades of μm in length [63, 64].

1.2.1. Porous Silicon

Porous silicon was discovered by Uhli [65] and Turner [66]. They observed a dark red material is formed on the surface

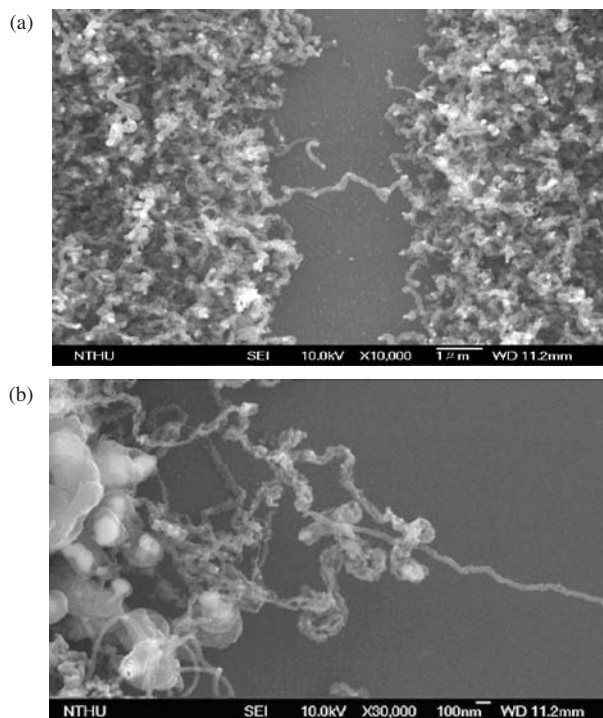


Figure 6. (a) A single carbon nanofiber grown across isolated electrodes as a current conduction bridge, (b) the root of the single fiber is multi-connected to nickel electrodes. Reprinted with permission from [56], S. Y. Chen et al., *J. Nanosci. Nanotechnol.* 5, 1987 (2005). © 2005, American Scientific Publishers.

of silicon during electrochemical polishing with the current density less than a critical value. The experimental procedure is expressed as follows. The unpolished sides of (111) or (100) *p*-typesilicon wafer are deposited with silver film by dc sputtering for obtain a good ohmic contact. The PS layers are formed by anodizing these wafers in 48 wt% HF and 98 wt% C₂H₅OH solution with a constant a current density of 50~110 mAcm² at an etching time of 15 min. The scanning electron microraphs (SEM) of top and cross view of the (100) PS layers are shown in Figures 7(a) and 7(b), respectively [67]. Figure 8 illustrates the SEM picture of the roots of the PS. A silica film with well-aligned mesochannels similar to photonic crystals can be formed through sol-gel dip coating of a silica precursor with non-ionic ethylene oxide surfactant [68]. A mixture of C₁₆EO₁₀ [C₁₆H₃₃(OCH₂CH₂)₁₀OH] amphiphilic block copolymer and TROS [(C₂H₅O)₄Si] in acidic media was used to prepare templated silica sol. The sol was then dip coated on a pre-cleaned silicon wafer under saturated ethanol vapor to produce a crack free and continuous SiO₂ of ~0.2–0.3 μm in thickness. Heat treatment by backing under 30% relative humidity at temperatures of near 353 to 383 K and cleaning at 723 K establishes the interfacial bonding between the coated film and the substrate, thus preventing the in-plane shrinkage of the film [69]. Schematic illustration of the XRD experiments and three dimensional pore structure in SiO₂ film and the TEM images are shown in Figure 9.

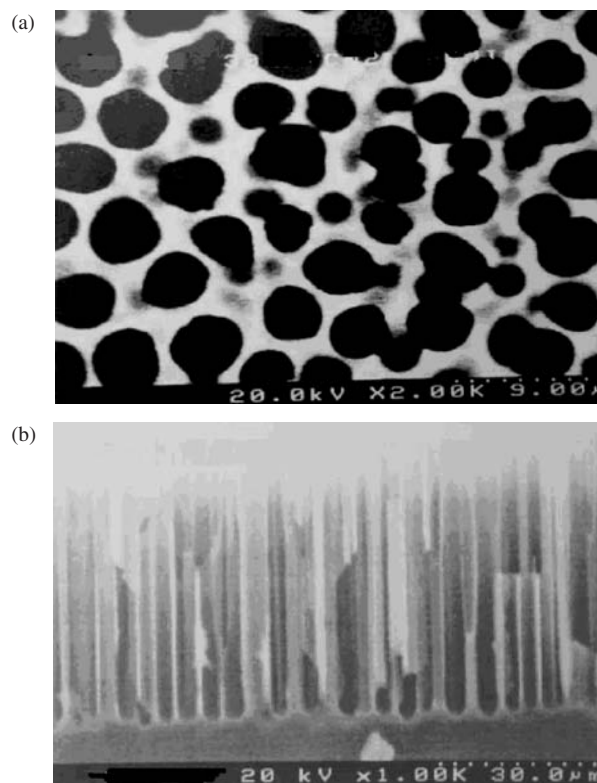


Figure 7. (a) The scanning electron microraphs (SEM) of top and (b) cross view of the (100) PS layers. Reprinted with permission from [67], C. S. Chang and J. T. Lue, *Thin Solid Films* 259, 275 (1995). © 1995, Elsevier.

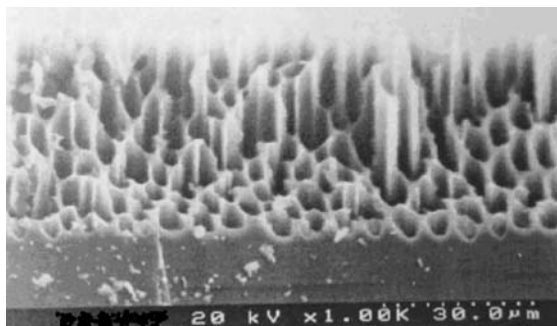


Figure 8. SEM picture of the roots of the porous silicon. Reprinted with permission from [67], C. S. Chang and J. T. Lue, *Thin Solid Films* 259, 275 (1995). © 1995, Elsevier.

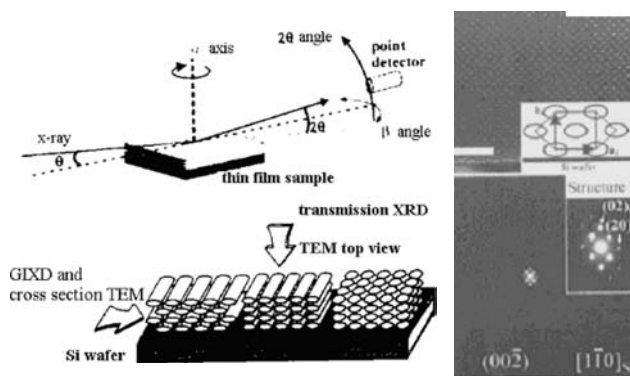


Figure 9. Schematic illustration of the XRD experiments, the three-dimensional pore structure in SiO_2 film, and the TEM images. Reprinted with permission from [68], P. T. Liu et al., *J. Appl. Cryst.* 38, 211 (2005). © 2005.

2. PHYSICAL PROPERTIES

2.1. Structures

Auger electron spectroscopy (AES) and X-ray photoelectron spectroscopy (XPS) can be utilized to characterize the surface impurities to a depth of $0.5\sim 1$ nm with a spatial resolution of $0.2\ \mu\text{m}$ for AES and $0.2\ \text{mm}$ for XPS, and a sensitivity of 0.3% [70] for both analyzers. The TEM electron diffraction pattern and the powder X-ray diffraction pattern can clearly display the crystal composition and structure. The Scherer's equation can be exploited to estimate the average grain size R for a knowing X-ray wavelength λ at the diffraction angle θ from the equation as given by [71]

$$\text{FWHM} = 0.94\lambda/R \cos \theta \quad (1)$$

where the FWHM is the full width at the half maximum of the characteristic spectrum in units of radians, R and λ are in nm. The impurity levels can be quickly examined by the electron probe micro-analysis (EPMA) from a scanning electron microscope (SEM). The chemical bonding modes that attached on the surface of the metal particles can be enunciated by the observation of the infrared absorption spectra. The metallic nanoparticles or the grounded powder of sol gel glass embedded with metal particles are mixed with

transparent KBr or polyethylene glycol powders for observing at wavelengths of $400\sim 500\ \text{cm}^{-1}$ and $650\sim 200\ \text{cm}^{-1}$, respectively, in a 1:10 volume ratio and then pressed into disks.

Carbon nanotubes [72] with the inlet of ammonia gas, the growth on Cu-20 wt% Fe substrate reveals a thick layer of cotton-like substance. The outlook is a blue-purple, fluffy structure with a thickness more than 3 mm. The SEM image as shown in Figure 10 illustrates an extremely delicate filament of 500 nm in length. We can juxtapose the electron diffraction and morphology of the HR-TEM as shown in Figure 11. The inset shows weak diffraction rings due to embedded polycrystalline metal particles and each spot composed of five parts arising from tubes of different sizes. It clearly indicates the chiral structure and the tube diameter of about 25 nm with longitudinal black-and-white strias of 0.29 nm in width. As counting from the point of white arrow, repetitive five-layers of tube-body-like carbon atoms follow two-layers of wall-like with a canted angle between wall and body being 45° . It is similar to a chiral tube as reported by Dresselhaus [73]. There are 7~8 chiral tubes present throughout the whole cross-section. Apparently, the reports of Dresselhaus yield succinct recapitulation to the projection of single tube and single wall tube. However, there are exceptions in this study where many extremely delicate tubes accumulate in a bundle.

The Raman spectrum as shown in indicates that the intensity of G band is obviously higher than D band which also occurs a shoulder at $1620\ \text{cm}^{-1}$ implying a structure of graphite layer. Whereas the selected diffraction pattern as shown in the inset of Figure 11 reveals a hexagonal close packed (HCP) pattern of multi-tubes and a strong ring caused by carbon gel on copper net in accompany with two vague concentric-rings meaning that the amorphous carbon layers are still remnant in the sample. In this scenario single and multi-wall carbon tubes are accumulated in bundles embedded with amorphous carbon between tubes. This "carbon nano-polytubes" (CNPT) are expected to have the best hydrogen storing for CNTs for their

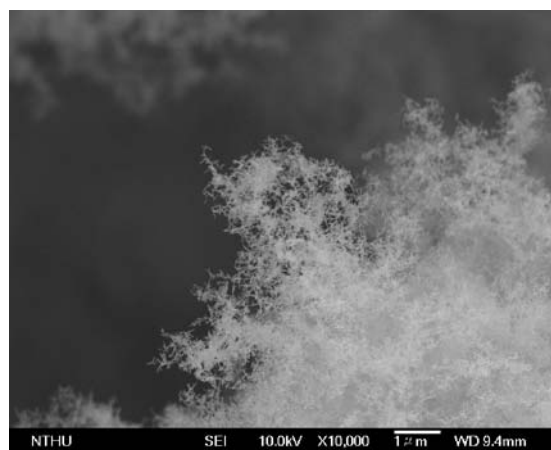


Figure 10. SEM of carbon polytubes (CNPTs) grown on Cu-20 wt% Fe bulk alloy substrate with H_2 and NH_4 as diluted gas. Reprinted with permission from [72], S. Y. Miao et al., *Eur. Phys. J. Appl. Phys.* 29, 153 (2005). © 2005.

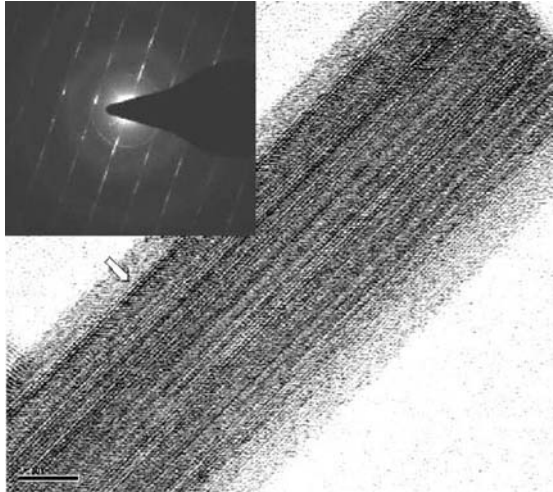


Figure 11. HRTEM lattice image and the inset is the selected diffraction pattern.

pure physical process as reported by Frankland et al. [74]. A tedious and genius experiment of the HRTEM as illustrated in Figure 12(a) for the solid cross-section of a bundle reveals the well-arranged concentric strias. The inset indicates white-background black-centered little hexagon spots for the exaggeration of the arrowed point. The diameter of these spots is about 0.53~1.25 nm with angled, singled, or doubled tubes bunched together. At the center part of the cross-section appearing in gray, more tubes accumulated with closer wall-to-wall resulting from fewer embedded amorphous carbon than those at the periphery parts.

Another laborious HRTEM picture as shown in Figure 12(b) illustrates a multi wrapped bundle of CNT for the sample deposited at substrate temperature of about 50° lower than that of Figure 12(a). Since the column is inclined at about 15° to the electron beam, we can see simultaneously the column and the cross-section.

Carbon-related films are expected to have important applications in electronic devices owing to their inheriting with the strong electron field emission. Conventionally in many reports [75–77], the Fowler-Nordheim (F-N) equation [78] was controvertibly implemented to delineate the results of field emission of diamond films and to calculate the work function. The F-N equation is derived for electron field emission from normal metal surfaces at high fields and low temperatures, and cannot delineate the temperature effect of the field emission for diamond films [79]. There were some improved theoretical models [80–82] for studying the field emission of diamond films. Further, some experimental results were reported [83–85] illustrating the temperature dependence on the field emission of phosphorus-doped diamond films. But, there are few literatures studying the temperature dependent on field emission of boron-doped diamond films by theoretical models. We have developed [86] a theoretical model for solving the field emission of semiconductor which conclusively can express the experimental works of the temperature dependence on field emission of boron doped diamond and diamond-like films.

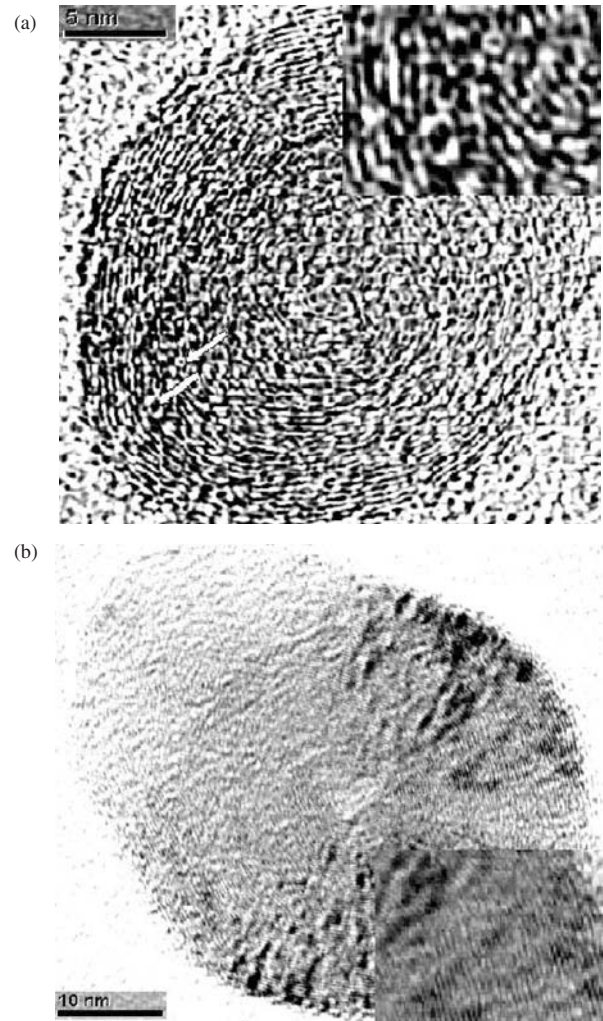


Figure 12. (a) The HRTEM for the solid cross-section of a bundle reveals the well-arranged concentric strias. The inset indicates white-background black-centered little hexagon spots for the exaggeration of the arrowed point. (b) HRTEM of a multi-circularly wrapped nanobundle (TWCNT). The insets are the exaggerated local points. Reprinted with permission from [72], S. Y. Miao et al., *Eur. Phys. J. Appl. Phys.* 29, 153 (2005). © 2005.

2.2. Field Emission

Firstly polycrystalline boron-doped diamond films were grown on *p*-type (100)-oriented Si substrate by an Astex 5400 microwave plasma enhanced chemical vapor deposition (MPECVD) system. The detail procedure was described in previous report [87]. To study the temperature effect on the field emission, the samples were mounted on the cooling station of a helium closed-cycle refrigerator. The diamond film was separated from the anode (indium-tin oxide coated glass), by a 50 μm Teflon spacer. Typical measurements were made as the sample cooled down from room temperature to 20 °K. A programmable current source provides a step-wise constant current with output voltages varying from 0 to 1100 V. On account of the low electron affinity, electrons emitted from *p*-type semiconductor can be presumed to comply with the emission current of metal-insulator semiconductor (MIS) Schottky barrier diode [88] with total

emission current density as giving by

$$J_{\text{total}} = J_c + J_v + J_s \quad (2)$$

where J_c , J_v , and J_s are the emission current densities, which are proportional to the tunneling probabilities T_c , T_v , and T_s from the conduction band, the valence band and surface state, respectively. Using the WKB approximation. The transmission probability [88] for electrons to tunnel through the potential barrier can be readily derived to yield the current density as given by $J_c = A^* T^2 T_c e^{-q(\phi_{Bn} - V_s)/KT}$, where A^* is the Richardson constant, T_c is the electron tunneling coefficient, ϕ_{Bn} is the barrier height of n -type semiconductor, and V_s is the applied voltage developed across the semiconductor. Bandis et al. [89] had alluded that field emission from surface states is unlikely implying the negligibility of J_s . A tedious manipulation of Eq. (1) can yield a simple formalism [90] as given by

$$J_{\text{total}} = a_1 T^2 e^{-\theta/kT} e^{-b_1 \chi^3 / F} + a_2 \frac{1}{\chi + E_g} F^2 e^{-b_2 (\chi + E_g)^{3/2} / F} \quad (3)$$

where

$$a_1 = \frac{qmk^2}{2\pi^2 \hbar^3}, \quad b_1 = \frac{4\sqrt{2}m}{3q\hbar} v(y),$$

$$a_2 = \frac{\pi q^3 m_p \hbar^2}{2mt^2(y)}, \quad b_2 = \frac{4\sqrt{2}m}{3q\hbar} v(y)$$

$v(y)$ is a tabulated function involving elliptic integrals, χ is the electron affinity, $t(y)$ is another tabulated function, θ is the difference energy between surface conduction band minimum and Fermi level, and F is the external electric field.

Previously [90], we tacitly assumed that the emission current dropped due to the increase of surface barrier height as temperature decreases attributed to the result from the prediction of F-N equation. But the F-N equation contains only one parameter of the material, the effective surface barrier ϕ , is insufficient to describe the band diagram of diamond. In this study, we include two fundamental parameters, the electron affinity χ and surface band bending $E_{cs} - E_f$ which can clearly elucidate the band diagram as shown in Figure 13 for field emission process. It illustrates electrons tunnel through the surface barrier. In cases of the presence of density of states with the Fermi level higher than those of P -type bulk diamond films, the electrons flow cause band bending near the surface. If the Fermi level of surface states lowers down as temperature increases, less electrons flow from surface state to bulk p -diamond film. Consequently the bending down of surface band becomes shallow. The threshold turn-on voltage rises as temperatures decrease due to the enhancement of band bending down. The catastrophic bending down of surface conduction band at lower temperatures results in a lower electron emission. Similar result of B-doped diamond-like films is shown in Figure 14 [90]. The electron affinity retains its original value at various temperatures. The work function of diamond-like films has a larger value than that of diamond films resulting in a lower electron emission current at the same applied bias.

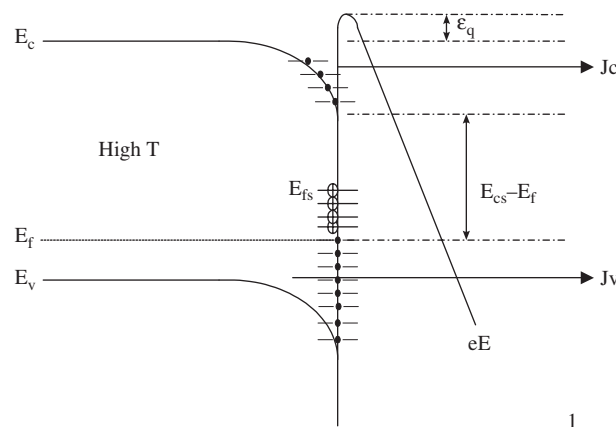


Figure 13. Schematic energy band diagrams for (a) high temperature; and (b) low temperature, respectively. Reprinted with permission from [98], S. Y. Chen et al., *J. Phys. D: Appl. Phys.* 37, 273 (2004). © 2004, Institute of Physics.

This work illustrates that the field emission current from the valence band has negligible dependence on temperatures and is negligibly small for p -type diamond and diamond-like films which dominates the emission current at low temperatures, while the field emission current from the conduction band depends on temperature largely. The conventional F-N equation is applicable to address the emission current at high field and low temperatures. Although the F-N equation can fit the emission current–voltage curve with various work functions at different ranges of temperatures, whilst the work function is an intrinsic invariant constants. We proposed that the behavior of the field emission characteristics can be well expressed by a similar theory of the thermionic emission current of MIS Schottky barrier diodes. The empirical fitting results show that the electron affinity is unaffected

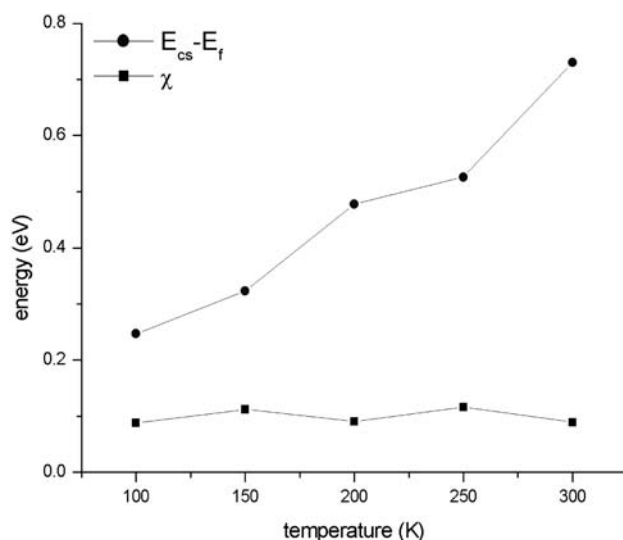


Figure 14. Theoretical fitting for B-doped diamond-like films with χ the electron affinity, $E_{cs} - E_f$ the energy difference between surface conduction level and Fermi level. Reprinted with permission from [90], J. T. Lue et al., *J. Non-Cryst. Solids* 265, 230 (2000). © 2000.

while the bending down of surface states increases as the temperature decrease.

To study the temperature effect of field emission properties of CNTs, the emission current was measured in cycles of cooling down and warming up. The fitting results of the electric field dependence on current density at various temperatures are depicted in Figure 15. The curves illustrate that the emission currents sensitively depend on temperatures. This behavior is quite different from the temperature dependence of the FE characteristic of well-aligned CNT films [80, 84]. The semiconductor thermionic equation that can successfully address the field emission of CNTs involves three fundamental parameters of material properties i.e., the electron affinity χ , the energy gap E_g , and the interface barrier height $E_{cs}-E_f$. Figure 16 illustrates theoretical fitting parameters as deduced from the data of Figure 15, in which β is 367. It implies that the energy difference between the conduction band and the Fermi level ($E_{cs}-E_f$) decreases as temperature decreases, while the electron affinity χ and the energy gap E_g (~ 2.5 eV) is almost independent of temperatures. Thus we can elucidate the FE mechanism of random aligned R-CNT, which is similar to the results of well aligned A-CNT [72]. At low temperatures, few electrons flow out from the semiconductor tip of the metallic multi-wall carbon nanotubes (MWCNTs) to surface localized states due to less ionization of localized state. The Fermi level of interface-localized states is high resulting in lowering the interface barrier-height as the temperature decreases.

As compared to the field emission properties of well-aligned CNTs as shown in Figure 17, it is beyond our consensus that the threshold voltage of randomly oriented CNT films is smaller than that of well-aligned CNTs. The threshold field of randomly oriented CNT is about 27000 V/cm, while that of well-aligned CNT is about 33000 V/cm. The corresponding emission current density of R-CNT is 5.5×10^{-4} A/cm², while that for A-CNT is 1.0×10^{-5} A/cm². The enhancement factor of R-CNT ($\beta = 367$) is also larger than

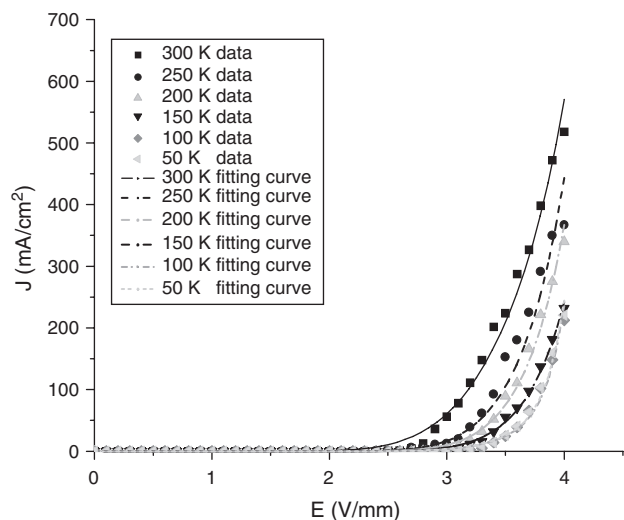


Figure 15. The temperature dependence of field emission for randomly oriented MWCNT films. Reprinted with permission from [98], S. Y. Chen et al., *J. Phys. D: Appl. Phys.* 37, 273 (2004). © 2004, Institute of Physics.

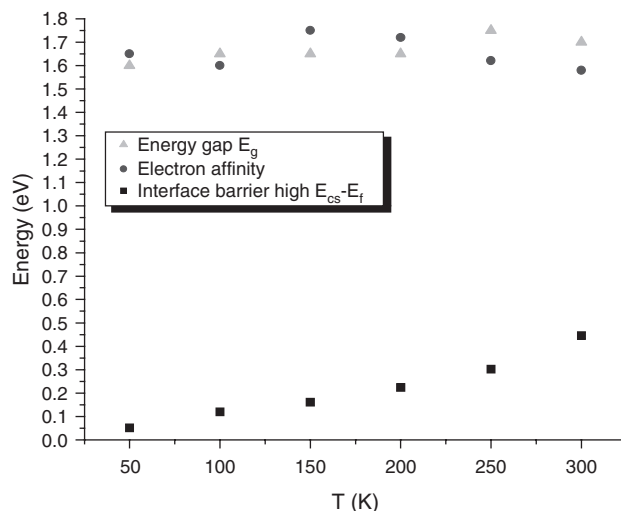


Figure 16. The theoretical fitting for randomly-oriented MWCNT films.

that of A-CNT that is also controvertible to physical consensus. The ideal value of enhancement factor β of CNT is the ratio of the average height h to the radius r of the tube that is crucially determined by the geometry of the body, and independent to the material. For randomly oriented CNT, the β is nearly equal to 1. Theoretically, the field emission current only contributes from the tube-end not from the tube-body [91]. However, some authors [92] reported that randomly distributed CNTs have impressive field emission capabilities.

The enhancement factor is attributed to the CNTs that are aligned perpendicular to the substrate. The experimental result is contradictory to the apparent consensus that the enhancement factor of R-CNTs will be less than that of A-CNTs. Though there are some CNTs that are perpendicular to the substrate, where the screening effect can be

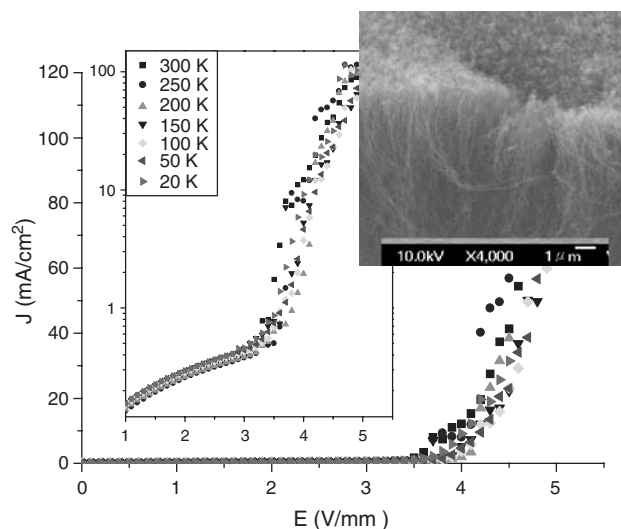


Figure 17. The temperature dependence of field emission for aligned MWNT films. The inset is the SEM image of densely aligned CNT films. Reprinted with permission from [98], S. Y. Chen et al., *J. Phys. D: Appl. Phys.* 37, 273 (2004). © 2004, Institute of Physics.

ignored. Zou [91] tacitly assumed that the contribution of field emission efficiency from the local π electrons decreases from the tip to the body. However, some experiments [93–94] and theoretical results [95] appraised that defects distributed on the body play essential role in field emission. Envisaging the screen effect of the well aligned CNTs, the emission efficiency will be degraded. Furthermore, the fitted work function of CNT is about 1.65 eV, which probably results from the average of two terms attributing to amorphous carbon and defects. Amorphous carbon is the dominant part of the film with an energy gap of about 1~3 eV while defects localize the electron wave vectors of CNTs along tube axes and have an energy gap about 2.5 eV in the tube end.

The Raman spectra of CNT are similar to the graphite layered structure whilst with the exact shift and line shapes depending on the real structure. Both single and multi-wall CNTs reveal strong Stokes Raman peak near 1580 cm^{-1} relating to the E_{2g} active modes. On accounting the defect structure of the multi-wall CNTs, the Raman D-line near 1350 cm^{-1} shall be accompanied. The breathing modes of SWCNT ranging from $100\sim 300\text{ cm}^{-1}$, with real shifts closely relating to the inverse of tube diameter d are usually implemented to mechanical and electrical properties, whilst the entangled tangential stretching modes near 1589 cm^{-1} are used to determine the number of structures [92–94]. Figure 18 shows a typical Raman spectrum of MWNTs indicating two characteristic peaks. The G-line peak at 1580 cm^{-1} corresponds to the high-frequency Raman-active E_{2g} mode of graphite. The strong and broad D-line at 1350 cm^{-1} and a weak D'-band at around 1621 cm^{-1} was sophisticatedly attributed to disorder-induced carbon features arising from finite particle size effect or lattice distortion [95–96]. Another prospect of the origins of D-line is attributed to defects in the curved graphite sheets, tube ends, and finite size crystalline domains of the tubes [97]. The films contain many curled CNTs as shown in Figure 19(a), while Figure 19(b) demonstrates the popularly existed graphite nanoparticles and amorphous carbon [98]. The corresponding micro Raman spectra are shown in Figure 20 for different species. The observed G-line (at 1580 cm^{-1}) illustrates that these two zones popularly contain graphite sheet structures, while CNT nanoparticles or curled

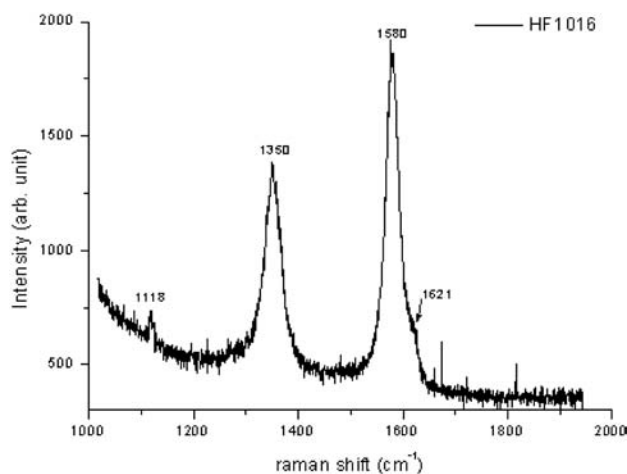


Figure 18. A typical Raman spectrum of MWNTs.

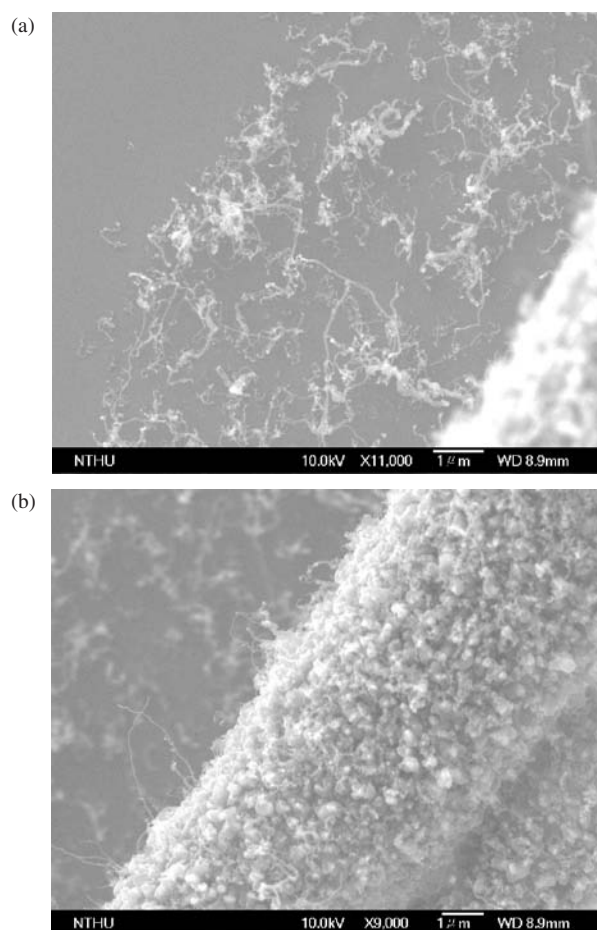


Figure 19. The SEM images for the sample at (a) HF1113-NiFe-wb zone, and (b) at HF1113-NiFe-B zone, respectively. Reprinted with permission from [98], S. Y. Chen et al., *J. Phys. D: Appl. Phys.* 37, 273 (2004). © 2004, Institute of Physics.

structures reveal the characteristic peak at 1350 cm^{-1} resulting from the breakdown of translational and point lattice symmetries at the edge plane. In one zone popularly distributed with curve MWCNTs, the G-line shifts to a higher frequency from 1580 cm^{-1} embodied in the significant existence of sp^2 short-range order in the tubes [99]. The appearing of stronger D-line intensity than the G-line is interpreted as due to the presence of finite size (nanometer order) of the crystalline domains or defects. As an evidence from the micro-Raman spectra, it concludes that the frequency shift of the G-line and the stronger D-line intensity in one sample is caused by defects in the tube which is also alluded by the SEM showing that the wall of curled tubes contain many defects like pentagons. In other another zone distributed graphite grains the characteristic peaks are similar to disordered graphite. The decrease of the intensity ratio of D-line and G-line (I_D/I_G) is attributed to the accompanied large amounts of amorphous carbon particles. From above discussions, the presence of G line with a small bump at the high-energy side (1620 cm^{-1}) justifies the sample being MWCNTs as compared to the data dwelled in literatures [100, 101].

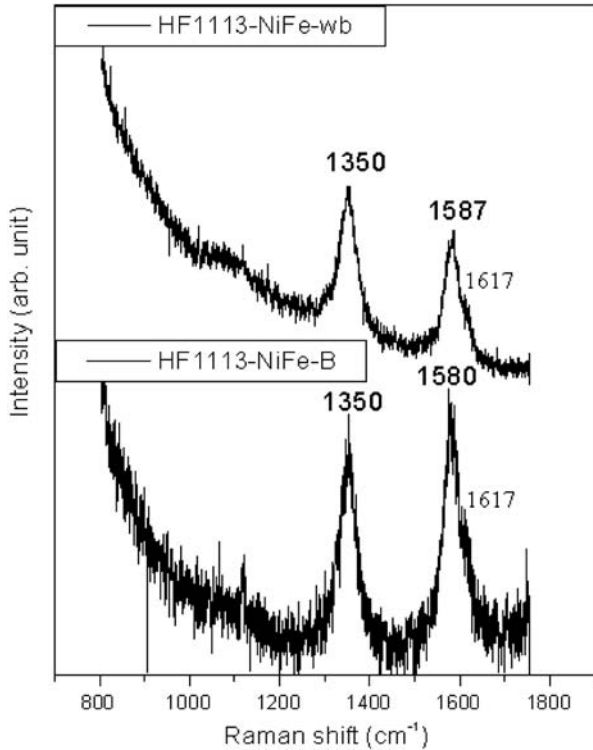


Figure 20. The micro Raman spectrum corresponding to above samples. Reprinted with permission from [98], S. Y. Chen et al., *J. Phys. D: Appl. Phys.* 37, 273 (2004). © 2004, Institute of Physics.

2.3. Electrical Properties

2.3.1. Conduction of Metallic Nanoparticles

The electrical conductance for the agglomerated metallic particles or the deposited nano-sized thin films depends on the filling factor of the connected and empty spaces. At low filling factor, the particles may be separated individually. The mechanism of conductivity on the thin film can be extensively addressed by a simple tunneling between localized insulating states [102, 103] that imply a high resistivity at low temperatures. When the filling factor is large enough for the particles to aggregate into clusters, and at least a conducting path is connected from one side of the sample to the other, the sample begins to exhibit current conduction. The resistivity $\rho(R, f, A)$ will be dependent on the particle size R , the filling factor f , and the aggregation factor A , which represents the extent to which the particles are connected with each other to those are discrete. Potential barriers usually occur between the boundaries of particles to particles, therefore the conduction electrons subjected to grain boundary scattering. For the electron mean free path ℓ within each particle being larger than the grain size R , the Monte Carlo simulation [104] by the random process yields a semi-empirical law for the electrical conductivity as

$$\sigma_g = \frac{ne^2l}{mv_F} \Gamma^{1/R} \quad (4)$$

within the grain boundary, where Γ is the transmission probability for electrons to tunneling through the grain boundary, v_F are the Fermi velocity, and l is the electron mean free

path. The grain boundary scattering as expressed in Eq. (4) required the grain size must be larger than the electron mean free path. In each metal particle, the mean free path is determined by the electron phonon scattering. With proper values of the above fitting parameters, the temperature coefficient of resistivity (TCR), $\partial\rho/\rho\partial T$ can be retrieved with either a positive or negative value at certain temperatures.

Reducing the metallic particle size further into nano-size, the experimental data on metallic nanoparticle films [105, 106] composing of aggregated nanoparticles in conducting form indicate a linear Bloch-Grüneisen equation for absorption or emission a phonon at high temperatures, which can be fitted successfully with an effective Debye temperature Θ_D . The Θ_D is softened from its bulk values in the presence of particles, which decreases as the particle size is reduced. However, the resistivity measurements indicate anomalous breaks occurring at the lower temperature end of the linear Bloch-Grüneisen plot. A sophisticated explanation is the contribution of the Kondo effect resulting from spin flip-flop scattering of conduction electrons with the magnetic impurities in the sample.

The diamagnetic metals behaves paramagnetic state as the bulk metal is dispersed into nanoparticles due to the inherited even or odd number of electrons retained in each nanoparticles. The collection of nanoparticles with a large number of spin-unpaired states behaves a spin glass states [107]. The nanoparticles inherited with unpaired spin behave as magnetic impurities to contribute spin scattering. The Kondo resistivity [108] arising from spin-flip scattering is given by

$$\rho_{\text{spin}}(T) = \rho_1 - \rho_2 |J| \ln(T) \quad (5)$$

where ρ_1 and ρ_2 are independent of temperatures, and J is the exchange integral between s and d electrons. The electron numbers contained inside each metallic nanoparticle can be even or odd with equal probabilities. The particles occupied with odd number of electrons have a net electron spin and behave like paramagnetic impurities. The electron spin resonance and magnetic susceptibility measurements of silver nanoparticles all verify the existence of local magnetic moments in the diamagnetic material.

The strategy of dealing the Kondo resistivity in nanoparticles crucially depends on the assumption that the Kondo temperature T_k decreases as the particle size is reduced which is tacitly assumed as

$$T_k \approx T_{k0} e^{-R_0/R} \quad (6)$$

where T_{k0} is for the bulk value and R_0 is a constant. This equation is under the consensus that T_k approaches zero as R approaches zero and $T_k \rightarrow T_{k0}$ as the particle size approaches the dimension of bulk solid. The particle size distribution will follow the log-Gaussian form and a statistical function $f(T_k)$ is introduced to employ the distribution of T_k due to different particle sizes being presumed to be the same form as the particle size distribution which is normalized to be

$$f(T_k) = \frac{1}{\sqrt{2\pi}} \frac{1}{\ln \sigma_k} \frac{1}{T_k} \exp \left\{ - \left(\frac{\ln T_k / \bar{T}_k}{\sqrt{2 \ln \sigma_k}} \right)^2 \right\} \quad (7)$$

The total resistivity $\rho_{\text{total}}(T)$ can be the sum of the residual resistivity ρ_0 which is due to defect and impurity scattering, the Bloch-Gruneissen resistivity [104] $\rho_L(T)$ and the Kondo resistivity $\rho_{\text{spin}}(T)$ as given by

$$\rho_{\text{total}}(T) = \rho_0 + \rho_L(T) + \int_T^{\infty} \rho_1 f(T_k) dT_k - \int_T^{\infty} \rho_2 |J| \ln(T) f(T_k) dT_k \quad (8)$$

The theoretical result as illustrated in Figure 21 fits congruently with the experimental data.

Percolation theory has been utilized to delineate the conductivity of island films with connected or disconnected agglomeration of metallic nanoparticles. The fractal dimension D of granular thin film is given by

$$N(L) \propto L^D \quad (9)$$

where $N(L)$ is the number of metallic particles which are in a square with side L . Defining a probability P for filling the plane of the granular thin films resulting from the point view of percolation, the possibility of conduction electrons to pass through from one edge to the other is given by [109]

$$\theta(P) \propto (P - P_c)^\beta \quad (10)$$

where P_c is the critical probability above which the thin film exhibits metallic conduction, and β is a constant depending on the property of the film. Evidently the electrical resistivity of the granular thin film is

$$\rho \propto (P - P_c)^{-\beta} \quad (11)$$

The resistivity convincingly decreases with the filling factor.

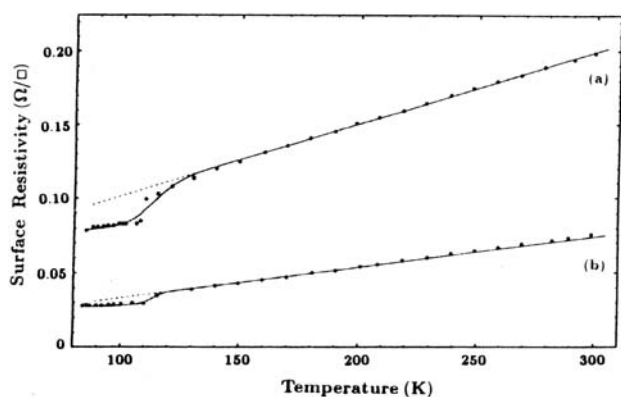


Figure 21. The experimental resistivity for films containing Ag nanoparticles with (a) $\bar{R} = 4.35$ nm, $\sigma = 0.6$ nm and (b) $\bar{R} = 5.7$ nm, $\sigma = 0.6$ nm. This fitting parameters for (a) $\rho_1 = 0.1$ Ω , $\rho_2|J| = 0.026$ Ω , $\bar{T}_k = 113$ K, $\rho_k = 1.072$ K, $\Theta_D = 163$ K, and $\rho_0 = 0.06$ Ω . Reprinted with permission from [107], J. T. Lue et al., *Phys. Rev. B* 51, 14570 (1995). © 1995, APS Org.

2.3.2. Electrical Conduction of Nanotubes

Carbon nanotubes (CNT), as examples of a quasi-one-dimensional conductor have attracted considerable attention since its discovery. Local conductance measurements of carbon nanotube networks with the nanometer scale resolution illustrate a rough discrete-drop in conductance with distance that is attributed to junctions of metallic and semiconducting tubes [110]. Electronic properties of crossed single-walled carbon nanotubes [111] were studied, which reveal Schottky barrier behavior for a metal-semiconductor contact [112].

The ferromagnetic properties might be attributed to the magnetic catalyst nanoparticles embedded in the tube, whereas the paramagnetic behavior comes from free spins of the unbounded sp^1 and sp^2 orbits of carbon atoms. The electron spin resonance lineshapes for some of the multi-wall carbon nanotubes are rather similar to be inherited to conduction electrons rather than to free electron spins. It is plausible that the exchange coupling of free spins between neighboring carbon atoms within the nanostructured tube evokes ferromagnetic state. To study their conductivities, most scientists applied electrophoresis method by dissolving carbon nanotubes in ethanol or 1,2-dichloroethane solutions and directly spin the solution onto the prefabricated metal electrodes after mild ultra-sonication. A single tube floating on the electrodes is selected to measure their current-voltage (I - V) characteristics, which usually envisages with intimate contact and the detachable problem at high currents [113-115]. Tunneling currents to surmount the barrier between contacts results in non-ohmic resistivity of nanotubes as dictated in many literatures [115-117]. Direct assembly of integrated carbon nanotube circuits using selective area chemical vapor deposition of prepatterned catalyst electrodes had been reported recently [118], which reveal a gap and a nonlinear response of the conductance at low temperatures. A solo carbon nanofibre was directly grown on the ends of two microelectrodes that were fabricated by the photolithographic method. The sample with a single CNT across the nickel electrodes was tediously selected by a scanning electron microscope (SEM) to measure the I - V characteristic at a closed cycle He refrigerator. A discontinuous step of the I - V curve was observed [119] at low temperatures as the current is above certain values. This high current is inaccessible by conventional deposition method that cannot firmly attach the CNT on electrodes, which also characterizes with high contact resistance.

The conductivity of the electrodes before CNT growth is almost negligible small inferring the insulation of the SiO_2 layer. The gap width is 3 μm and the CNT wire diameter is about 100 nm from an inspection of a SEM. The structure of the carbon nanofibre is not straight as expected. The ideal ohmic contact is verified by measuring the contact resistance after growth. Figure 22 dictates the current-voltage (I - V) characteristics at various temperatures with each data to be the averaged of twenty repetitive measurements.

The curves illustrate a step at temperatures below 100 K occurring at a rather high current density implicitly inferring that this phenomenon is difficult to be observed if the CNT is not so rigidly grown from the catalyst electrodes. The straight line within this current range reveals the ohmic contact whilst the nonlinear properties at even higher currents might be due to the space charge limits. The threshold

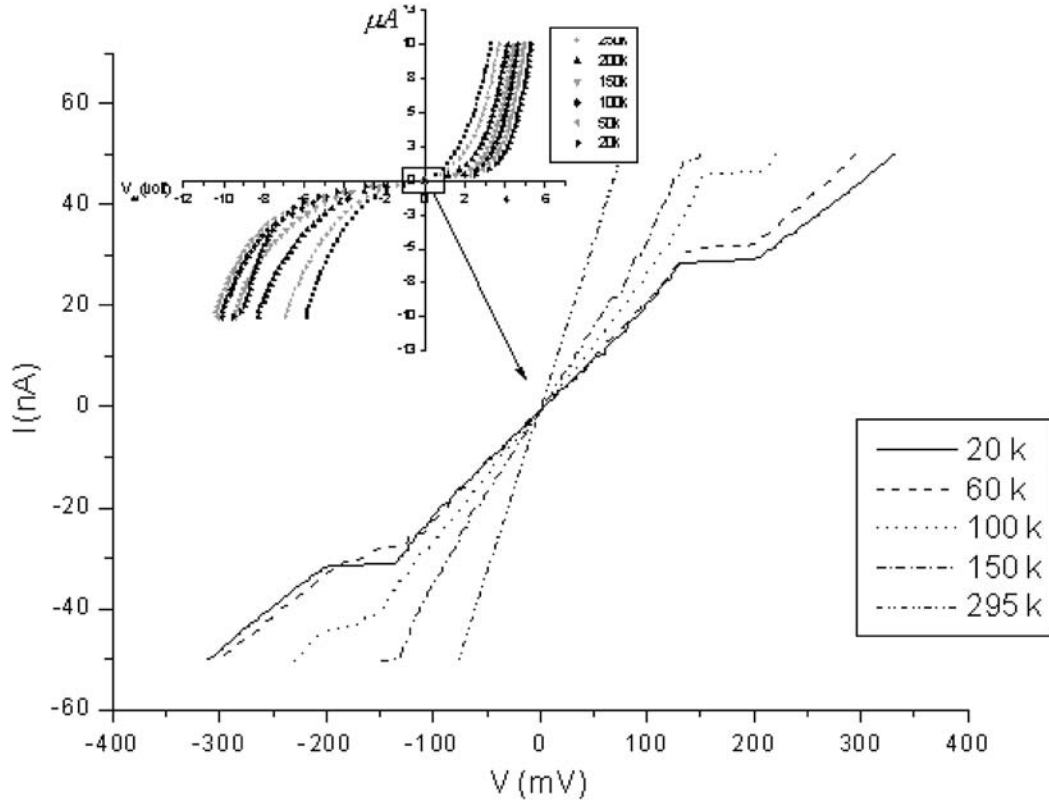


Figure 22. The I - V characteristic of one carbon nanofiber. Reprinted with permission from [119], L. W. Chang and J. T. Lue, *J. Nanosci. Nanotechnol.* 5, 1672 (2005). © 2005, American Scientific Publishers.

current at the step conductance decreases as the measuring temperature becomes lower and the step becomes prominent. At 20 K the step occurs at the bias of ± 150 mV that is justified by the carrier jump from one quantum level to another exhibiting a discontinuous of transport at this voltage. The logarithm of the normalized conductance at the specified voltage $\log(G/G_0)$ expressing a sharp dip at ± 150 mV, where G is the conductance.

A simple quantum theory [119] of one-dimensional conductors is illustrated to dwell the discontinuous jump of the conductance. The multiwall carbon nanotube can be simulated as a one-dimensional nano-wire with carriers to be quantum confined [200] under a dc bias as shown in Figure 23. The boundary conditions of the electron wave function ϕ at the wall surface with the azimuthal radius $\rho = a$ and at the ends of the tube for $z = 0$ and L are

$$\Phi(\rho = a) = 0, \quad \Phi(z = L) = 0 \quad (11a)$$

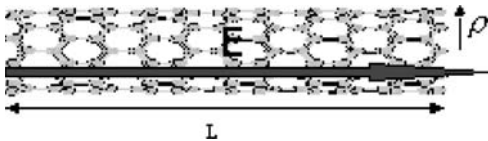


Figure 23. The conduction of 1D carbon nanotube with a length L , and azimuthal coordinate ρ . Reprinted with permission from [119], L. W. Chang and J. T. Lue, *J. Nanosci. Nanotechnol.* 5, 1672 (2005). © 2005, American Scientific Publishers.

Neglecting the electron-phonon interaction at low temperatures, the electrons only suffer the Coulomb energy eEz for the dc electric field E parallel to the z -axis. The Schrodinger equation in cylindrical symmetry coordinates is

$$\left[-\frac{\hbar^2}{2m_e^*} \left(\frac{\partial^2}{\partial \rho^2} + \frac{1}{\rho} \frac{\partial}{\partial \rho} + \frac{\partial^2}{\partial z^2} \right) - eEz \right] \Phi(\rho, z) = E_n \Phi(\rho, z) \quad (12)$$

where m_e^* is the effective mass of electrons, E_n is the eigen energy. Assuming the axial and radial components of the wave function to be non-interacting, we can propose a solution of form $\Phi(\rho, z) = R(\rho)Z(z)$. With the change of parameters

$$E_n = \frac{\hbar^2}{2m^*} (k^2 + k_z^2), \quad \text{and} \quad \gamma = \frac{2m^*}{\hbar^2} eE \quad (13)$$

we can have the radial and azimuth parts of the solution as given by

$$\frac{d^2 R}{d\rho^2} + \frac{1}{\rho} \frac{dR}{d\rho} + k^2 R = 0, \quad \text{and} \quad \frac{d^2 Z}{dz^2} + \gamma z Z + k_z^2 Z = 0 \quad (14)$$

where $R(\rho) = DJ_0(k\rho)$ is the first kind Bessel function with k satisfying the boundary condition $J_0(ka) = 0$. We obtain the eigen value $k = k_{0m} = x_{0m}/a$, where m is integers. On the other hand, the axial solution is the Airy function of type $Z(\xi_z) = a_n A_i(\xi_z)$ where $\xi_z = -\gamma^{-2/3}(\gamma z + k_z^2)$. We

can substitute the boundary condition $Z(z = L) = 0$ and $Z(z = 0) = 0$ to solve the wave vector k_z from $k_z^2 = -\gamma L + [(3\pi\gamma/2)(n - (1/4))]^{2/3}$, where $n = 0, 1, 2, \dots$. The total wave function includes two quantum numbers m and n .

The conductivity σ can be derived from the Kubo-Greenwood Formula [20]. In the independent electron model, the conductivity at frequency ω is given by the Kubo-Greenwood formula in conjunction with the transport of electrons from fill to empty state as given by

$$\sigma_E(\omega) = \frac{2\pi e^2 \hbar^2 \Omega}{m_e^* \omega} \int \{f(E)[1 - f(E + \hbar\omega)] - f(E + \hbar\omega) \times [1 - f(E)]\} |D|_{av}^2 N(E) N(E + \hbar\omega) dE \quad (15)$$

where Ω is the system volume, ω is the incident frequency, f is the Fermi-Dirac distribution, and the quantum current density $D = \int \phi_E^* \frac{\partial}{\partial z} \phi_E dV$. At low temperatures and dc bias, the conductivity is $\sigma_{E_F}(0) = ((2\pi e^2 \hbar^3 \Omega) / m_e^* |D|_{av}^2 \{N(E_F)\}^2$ and $N(E_F) = (m_e^* k_F) / (2\pi^2 \hbar)$. We then substitute the radial and axial solution to calculate the conductivity. Firstly, the Airy function in differential form $A_i(z) = -(z/(\pi\sqrt{3})) K_{2/3}((2/3)z^{3/2})$ is used to replace the $|D|_{av}$. A tedious calculation by utilization of a well-developed software program “Mathematica” can manipulate this complex equation to the result. The quantum jump of the conductivity at low temperature as observed in this experiment can be justified from above complicate formula. With these values substituted into Eq. (15) we can calculate the $|D|_{av}$ and then to retrieve the quantum states m and n . Although this quantum theory is premature to address the true conductance for the curly wire, we can sophisticatedly assume that the lengthy wire can be cut into several sections of straight tubes. It is probable that the conductance between one of the junctions subjects to a quantum jump for the current transport. We expect that the smaller the tube diameter the lower the quantum number. For multi-fibres bridging across the electrodes, the change of quantum states is smeared out for the vast proliferation of allowed change of quantum states. This low temperature (~ 600 K) MPECVD grown CNTs provided a much clean and versatile self-assembly of nanowires on micro-devices than the molecular jet chemical vapor deposition [118].

2.3.3. Dielectric Constants of Metallic Nanoparticles in Microwave Frequencies

The dielectric constant, the reponse function of the measured external field (the displacement) to the local electric field, closely relates to the conductivity and optical properties of materials. The dielectric constants of metallic nanoparticles in the microwave frequency range have rarely been reported [201]. The high microwave-field absorption of the metallic particles involves using the conventional method of inserting a powder-pressed thin disk in a microwave guide to determine the dielectric constant by measuring the attenuation and phase delay of the penetrating wave, which cannot be used. The author [202] proposed a method of measuring the dielectric constants of metallic nanoparticles using a microwave double-cavity dielectric resonator. The metal nanoparticles were mixed with alumina powder that was filled

and pressed in the inner hole of a sapphire disc. The resonant frequency and Q factor were measured at the TE_{011} mode to derive the complex dielectric constant. Dielectric constants specify the response of the dipole displacement in an external applied field in terms of ion and electron motion. Incident electromagnetic (EM) fields of different frequencies cause different responses from ions and electrons. As the size of the metal films or particles declines, the mean free path becomes constrained by surface scattering. The classical size effect [203], which affects the dielectric constant, occurs as the metal film thickness or the particle size becomes smaller than or similar to, the mean free path l of the carriers inside the metal. The quantum size effect arises as the particle size decreases further below the Bohr radius [204] where the continuous conduction band becomes discrete. In the simple quantum sphere model (QSM) for small metallic particles embedded in inert gas or air, the quantum confined electrons can be considered as nearly free electrons but with discrete energy levels. For metallic nanoparticles embedded in an active matrix, the diffusion model is adopted [205]. The conductivity of metallic nanoparticles decreases as the particle size decreases and behaves as non-conducting below a critical size and temperatures. Since the real part of the dielectric constant ϵ of metals is negative, the magnitude of the real ϵ evidently decreases with the particle size and approaches positive in accord with the material that behaves as an insulator.

A dielectric resonator (DR) that is composed of alumina powder with a high dielectric constant can significantly reduce the cavity volume and yield a high quality factor. The construction detail of the DR is shown in Figure 24 where a cylindrical rod of diameter b that comprises a mixture of metallic nanoparticles, alumina powder and paraffin with an effective dielectric constant ϵ_2 is installed into the center of a copper-made cavity that has an inner diameter d . The electromagnetic fields that can propagate inside the cavity can be solved from Maxwell’s equations with proper boundary conditions. The transverse electric (TE) mode, the transverse magnetic (TM) mode, and the hybrid mode (HEM) can normally be excited in a cavity. The TM_{010} mode has the advantages of a lowest resonant frequency that is independent of cavity length L and is easily identifiable. The TM_{010} mode is exploited because stronger electric fields are present

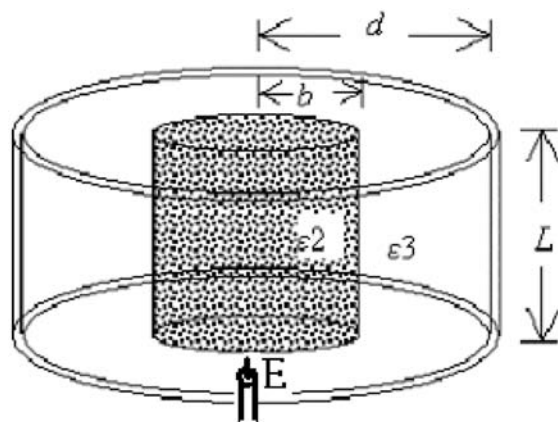


Figure 24. The cylindrical concentric cavity where ϵ_2 and ϵ_3 are the dielectric constants of the sample rod and the air gap, respectively.

near the axis than are present in the TE_{010} mode, resulting in a higher sensitivity due to metal conduction loss.

In addition to the measurement of the resonant frequency to derive the real part of the dielectric constant ϵ , we also measure the quality factor Q to derive the loss tangent and the imaginary part of ϵ . The total energy stored in the cavity is W_r . The quality factors are expressed as in Ref. [202] where Q_0 and Q_L are the unloaded cavity Q factors containing, respectively, without and with external wirings such as the transmission-line connector and the antenna. The Q_0 can be expressed as

$$\begin{aligned} \frac{1}{Q_0} &= \frac{P_C + P_d + P_{\text{nano}} + P_r}{\omega \cdot W_r} \\ &= \frac{1}{Q_C} + \frac{1}{Q_d} + \frac{1}{Q_{\text{nano}}} + \frac{1}{Q_r} \end{aligned} \quad (16)$$

where Q_C is the conducting loss of the copper wall, Q_d is the dielectric loss from paraffin and alumina, Q_{nano} is the loss from the metallic nanoparticles and Q_r is the radiation loss.

The Q_L can be directly measured from the -3db position of the transmission spectra, which is given by $Q_L = f_0/(f_2 - f_1)$. The unloaded Q_0 is simply derived from the formula [206] as $Q_0 = Q_L/(1 - |S_{21}(f_0)|) = Q_L/(1 - 10^{-\text{IL}(\text{db})/20})$, where $\text{IL}(\text{db})$ is the inserting loss, which can be directly read from the network analyzer.

The dielectric losses of the metallic nanoparticles is given by

$$\begin{aligned} Q_{\text{nano}} &= \frac{\omega \times W}{P_{\text{nano}}} = \frac{\omega \times (\epsilon_0 \cdot \epsilon_{\text{eff}} \cdot \int |E|^2 dV)}{\sigma \int |E|^2 d(V)} \\ &= \frac{\omega \cdot \epsilon_0 \cdot \epsilon_{\text{eff}}}{\sigma \cdot f} = \frac{\epsilon_{\text{eff}}}{\epsilon_i \cdot f} \\ &= \frac{W_r}{f W_2} \frac{1}{\tan \delta_{\text{nano}}} = \frac{W_r}{f W_2} \frac{\epsilon_{2r}}{\epsilon_{2i}} \end{aligned} \quad (17)$$

where ϵ_{2i} is the imaginary part of the effective dielectric constant, which is contributed mostly from metallic nanoparticles.

The dielectric constant of metallic nanoparticles is derived from the effective value of the total mixture. The effective medium theory, which considers the depolarization (the internal fields are distorted) of the medium by the presence of the local field induced by impurities, is valid only for a very small fraction of the impurity component. For a cylindrical rod that is composed of three components A, B, and C with two of them having comparable volume ratio, the effective dielectric is much appropriate to be expressed by the effective medium approximation (EMA) as given by [207]

$$f_A \frac{\epsilon_A - \epsilon_{\text{eff}}}{\epsilon_A + 2\epsilon_{\text{eff}}} + f_B \frac{\epsilon_B - \epsilon_{\text{eff}}}{\epsilon_B + 2\epsilon_{\text{eff}}} + f_C \frac{\epsilon_C - \epsilon_{\text{eff}}}{\epsilon_C + 2\epsilon_{\text{eff}}} = 0 \quad (18)$$

where f_i and ϵ_i are the volume ratio and dielectric constant of the i -th component, and ϵ_{eff} is the effective value of the mixture. The EM fields is concentrated in the dielectric rod as the ϵ of the alumina component is high. To retain the high quality factor, the volume ratio of metallic nanoparticles should be below 1% otherwise the resonant spectrum is difficult to be analyzed.

Considering the fact that the decrease of the electron relaxation time as the particle size reduces, the dielectric function at low frequency and long wavelength (at microwave frequency) derived from random phase approximation is derived as [208]

$$\begin{aligned} \lim_{\omega \rightarrow 0, q \rightarrow 0} \epsilon(q, \omega) &= \epsilon_0 - 0.1061(k_F a_0)[R/a_0]^2 \\ &\quad + i0.1061(k_F a_0)[R/a_0]^2 \end{aligned} \quad (19)$$

where a_0 is the Bohr radius, ϵ_0 is the dielectric for bulk value and k_F is the Fermi wave vector. This equation illustrates that the magnitudes of the real and imaginary parts of ϵ decrease with the decrease of the particle size behaving similarly to the electrical conduction.

Figure 25 schematically depicts the size dependence of ϵ on size. Equations (17)–(19) demonstrates that the imaginary part is derived through several manipulations of different Q factors so the error is larger than that of the real part, which is determined directly from the resonant frequency. We have also measured the dielectric constants of the same samples at liquid nitrogen temperature that reveals the increase of electric conduction at low temperatures implying an increase of the negative value of the real part. An abnormal peak of the imaginary part occurs for the particle size around 20 nm measured both at room and liquid nitrogen temperatures, which is sophisticatedly presumed due to a large distribution width of the particle size resulting in an indeterminacy of the EMA theory.

The blackish appearance of metallic nanoparticles (even for noble silver and gold metals) demonstrates that the electromagnetic properties for optical absorption remain similar over a wide range of wavelengths that may even extend to the microwave frequency. The complex dielectric constants depend on the particle size, the surface oxidation and the measured frequency. To our knowledge, no attempt to measure the dielectric constants of metallic nanoparticles at microwave frequencies is available for comparison. The effective dielectric constants for ultra thin silver films simulated from the optical second harmonic spectrum by exploiting the attenuated total reflection method are ranging from $-5.0 + 8.3i$ to $-20 + 15.0i$ within the wavelength from 5.32 to 10.64 nm for film thickness of 10 nm [209, 210] that are compatible to this work.

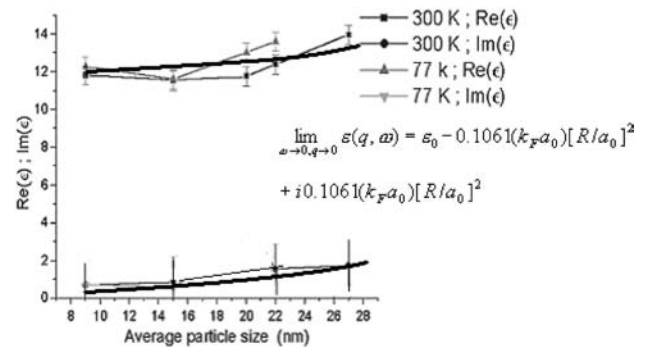


Figure 25. The size dependence on the absolute value of the real and imaginary parts of the dielectric constants for silver nanoparticles at room and liquid nitrogen temperatures. The heavy curves are the theoretical fitting of Eq. (19) employing with $a_0 \approx 10$ nm, and $k_F^{-1} \approx 4.8$ nm.

The magnitude of the real part of ϵ for metallic nanoparticles decreases with a decreasing particle size, suggesting that the particles become less conducting as the particle size decreases. The microwave absorption depends on the shape and size distribution, making extremely difficult to determine the imaginary part. The darkish appearance of many different metallic nanoparticles illustrates that the measured dielectric constants, even of silver and iron nanoparticles, are close in proximity.

2.4. Magnetic Properties

2.4.1. Quantum Tunneling in Magnetic Nanoparticles

Magnetite Fe_3O_4 nanoparticles have been popularly found in animal cells for cruising. One of the fascinating properties of magnetic nanoparticles is the reduction from multi-domains to a single domain as the particle size reduces to some limit values. Besides the vanishing of magneto hysteresis and the large reduction of coercive field for nanoparticles, the macroscopic quantum tunneling of the magnetic moment becomes possible. A quantum phase transition can differ fundamentally from a classical thermal transition because of its non-analyticity in the ground state energy of the infinite lattice system [211]. Unusual electronic and magnetic characteristics are prevalent at nonzero temperatures such as the metal-insulator transition in transition-metal oxides [212], non Fermi-liquid behavior of highly correlated f -electron compounds [213, 214], abnormal symmetry states of high- T_c superconducting cuprates [215, 216], and novel bistability of semiconductor heterostructures. The investigation of the remarkable properties of these systems attracts great efforts of researchers in condensed matter physics. The physics underlying the quantum phase transitions described above is quite involved and in many cases, has not been completely understood so far. In the high- T_c superconductors, for example, the superconductivity gives a direct way to study the quantum order-disorder transition. In heavy-Fermion materials, the characterization of the magnetic instability at $T = 0$ is complicated due to the presence of charge carriers and substitutional disorder. In spin glasses [217], one can vary the strength of quantum fluctuations to tune the spin glass phase into the paramagnetic phase.

A surface spin-glass layer is proven to be ubiquitous in magnetic nanoparticles at low temperatures [218]. A larger surface to volume ratio of the small nanoparticles implies a stronger surface anisotropic field to frustrate and disorder the inner spins, causing quantum tunneling at higher temperatures [219–221]. The phase diagram showing the quantum critical point at $T = 0$ with a dimensionless coupling function $g = g_c$, in which the Hamiltonian $H(g) = H_0 + gH_1$ at the presence of transverse anisotropic field H_1 , is sketched in Figure 26 where the anisotropic field-induced quantum tunneling due to the surface spin-glass layer is also speculatively plotted. There can be a level-crossing field where an excited state becomes the ground state at the critical field and creates a point of nonanalyticity of the ground state energy. The second-order phase transition for quantum driven phase transition usually occurs at the physically inaccessible $T = 0$ where it freezes into a fluctuationless ground

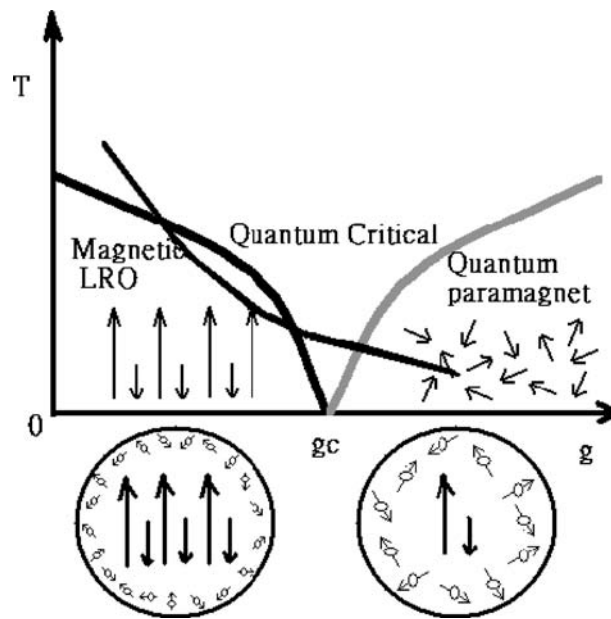


Figure 26. The phase diagram of quantum critical behavior and the anisotropic surface spin glass induced superparamagnetic states. Reprinted with permission from [227], C. T. Hsieh and J. T. Lue, *Phys. Lett. A* 36, 329 (2003). © 2003, Elsevier.

state. The critical field emanating thermally driven phase transition occurring at $T > 0$ is smaller than the critical value g_c for $T = 0$ and decreases as the particle sizes reduce or the transverse field increases.

The low temperature magnetic viscosity of these systems shows a constant value below a finite temperature reflecting the independence of thermally over-barrier transitions and is the signature of quantum tunneling of the magnetization. Although there are some related evidences [222, 223] about our results, we provide an alternative theory and experimental tool to survey analytically. Electron spin resonance (ESR) spectrometry is exploited to study the magnetic states of single domain spinel ferrite nanoparticles. As the temperature decreases, the spectrum changes from superparamagnetic resonance (SPR) to blocked SPR and arrives at quantum SPR as the temperature lowers down further. A nanoparticle system of a highly anisotropic magnet can be qualitatively specified by a simple quantum spin model, or the Heisenberg model with strong easy-plane anisotropy [224]. Disordered spin-glass-like nanoparticles [225] become quantum paramagnets under anisotropy-assisted quantum tunneling. We tacitly assumed that an alternative approach would lead to a better understanding of the fascinating interplay in the vicinity of the quantum critical point in magnetic nanoparticles.

A surface spin-glass layer is proven to be ubiquitous in magnetic nanoparticles at low temperatures. A larger surface to volume ratio of the small nanoparticles implies a stronger surface anisotropic field to frustrate and disorder the inner spins, causing quantum tunneling at higher temperatures. The phase diagram showing the quantum critical point at $T = 0$ with a dimensionless coupling function $g = g_c$, in which the Hamiltonian $H(g) = H_0 + gH_1$ at a presence of transverse anisotropic field H_1 , is sketched in

Figure 26 where the anisotropic field-induced quantum tunneling due to the surface spin-glass layer is also speculatively plotted. There can be a level-crossing field where an excited state becomes the ground state at the critical field and creates a point of nonanalyticity of the ground state energy. The second-order phase transition for quantum driven phase transition usually occurs at the physically inaccessible $T = 0$ where it freezes into a fluctuationless ground state. The critical field emanating thermally driven phase transition occurring at $T > 0$ is smaller than the critical value g_c for $T = 0$ and decreases as the particle sizes reduce or the transverse field increases.

The Hamiltonian [226, 227] of the Heisenberg model with strong easy-plane anisotropy with internal transverse fields σ_i^x without applying an external field is given by

$$H = - \sum_{i,j}^N J_{ij} \sigma_i \sigma_j - \Gamma \sum_i^N (\sigma_i^x)^2 \quad (20)$$

where σ 's are the Pauli spin matrices, $J_{ij} > 0$ are the longitudinal exchange couplings and Γ is the transverse anisotropy parameter for the spin-spin interaction causing quantum tunneling. Long-range force dominates the system for $J_{ij} \gg \Gamma$. We can express $H = H_0 + H_1$, where H_0 and H_1 correspond, respectively, to the first and second terms in the right hand side of Eq. (20) and commute with each other. The ground state of H_0 is long-range magnetically ordered and prefers ferromagnetism at low temperatures, while the ground state of H_1 favors the quantum paramagnetism. As the particle size decreases, the anisotropic field Γ increases up to a critical value, [228, 229] upon which a point of non-analyticity in the ground state energy is generated. The ground state of the total system varies from the magnetic long-range-order ground state H_0 to the paramagnetic ground state H_1 . This means that the ground state energy is not continuous across the critical point at $T = 0$. But many experiments demonstrated that at some nonzero temperatures, though very low, an interplay between quantum and thermal fluctuations occurs.

In the case of applying an external transverse field, we consider the corresponding Hamiltonian in the same Heisenberg model [226] as

$$H = - \sum_{i,j}^N J_{ij} \sigma_i \sigma_j - \Gamma' \sum_i^N \sigma_i^x \quad (21)$$

The ground state of the first term prefers that the spins on neighboring ions are parallel to each other and become ferromagnetic for $J_{ij} \gg \Gamma$, whereas the second term allows quantum tunneling between the spin up $|\uparrow\rangle_j$ and spin down $|\downarrow\rangle_j$ states with amplitudes being proportional to the transverse field Γ' . Both the off-diagonal terms σ_i^x in Eqs. (20) and (21) flip the orientation of the spin on a site by quantum tunneling. There can be a level-crossing field where an excited state becomes the ground state at the critical field and creates a point of nonanalyticity of the ground state energy as a function of Γ' . The second-order quantum phase transition usually occurs at the physically inaccessible $T = 0$ where it freezes into a fluctuationless ground state. The transverse critical field emanating a quantum phase transition occurring at $T > 0$ is smaller than the critical

value Γ_c for $T = 0$ which decreases as the particle sizes reduce.

At high temperatures, single domain magnetic nanoparticles are thermally free to orient their spin directions and exhibit superparamagnetic properties. The superparamagnetic state is blocked as temperature lowers down to enhance the exchange interactions between particles. This critical temperature increases with the particle volume V and the magnetic anisotropic constant K_a . Below the blocking temperature T_B , depending on a typical time scale of measurements τ , the slow down of thermal motion implies the magnetic nanoparticles to undergo a transition from superparamagnetic to blocked SPR which behaves like a ferromagnetic state for the total system. However, the zero-field-cooled magnetization measurement indicates that the superparamagnetic relaxation time is estimated to be $\tau_m \sim 10^2$ s. Since the time scale for observing the ESR spectra is much shorter than that for magnetization measurements, the blocking temperature T_B^E for ESR is much higher than that of the magnetization measurements T_B^m . The ESR provides an excellent method to detect the quantum phase transition at temperatures higher than $T = 0$.

The temperature dependent EPR spectra for Fe_3O_4 nanoparticles obtained from 220 K to 4 K are specified by curves as shown in Figure 27. The tiny spectrum centered at $g \sim 4.3$ is attributed to the isolated spin ${}^6\text{S}_{5/2}$ of the remnant Fe^{3+} ions when the second-order crystal field coefficient with axial symmetry vanishes while that with rhombic symmetry persists [230]. The relatively narrow SPR line (~ 100 Gauss) fades and the broad blocked SPR resonance line (~ 1500 Gauss) manifests as the temperature decreases to about 35 K. The linewidth reveals abnormal broadening (~ 1500 Gauss) below the blocking temperature (63 K) and the broad line grows and becomes prevalent until the temperature reaches 22 K. The narrowing of the SPR linewidth at high temperatures is attributed to the thermal fluctuations of the magnetic nanoparticles while the broadening of the blocked SPR results from the line up of the magnetizations of all particles that enhances the anisotropic field at low temperatures. As temperatures decrease to 20 K, there is a renaissance of an anomalous paramagnetic resonance with the amplitude growing and decaying until the temperature decreases to about 8 K. An anomalous paramagnetic resonance prevails behaving like a free exchange-coupled giant spin, as expressed to be a quantum superparamagnetic state. The anisotropic field K_\perp increases as temperature decreases resulting in a higher tunneling rate. The domain size of the quantum SP particle decreases attributing to prominent transfer of magnetic domains into surface spin glass state.

Considering that the strong surface anisotropic field would destroy the internal exchange force making the long-range ferromagnetic state to become paramagnetic can better elucidate this quantum paramagnetic state existing at low temperatures. Below 8 K, the amplitude of paramagnetic resonance decreases resulting from the commencement of maximizing the anisotropic field and the reducing of thermally assisted paramagnetic resonance.

Figure 28 illustrates the occurrence of the amplitude peak at low temperatures and the linewidth variations for superparamagnetic, ferrimagnetic, and quantum paramagnetic resonance, which are about 100 G, 1500 G, and 10 G,

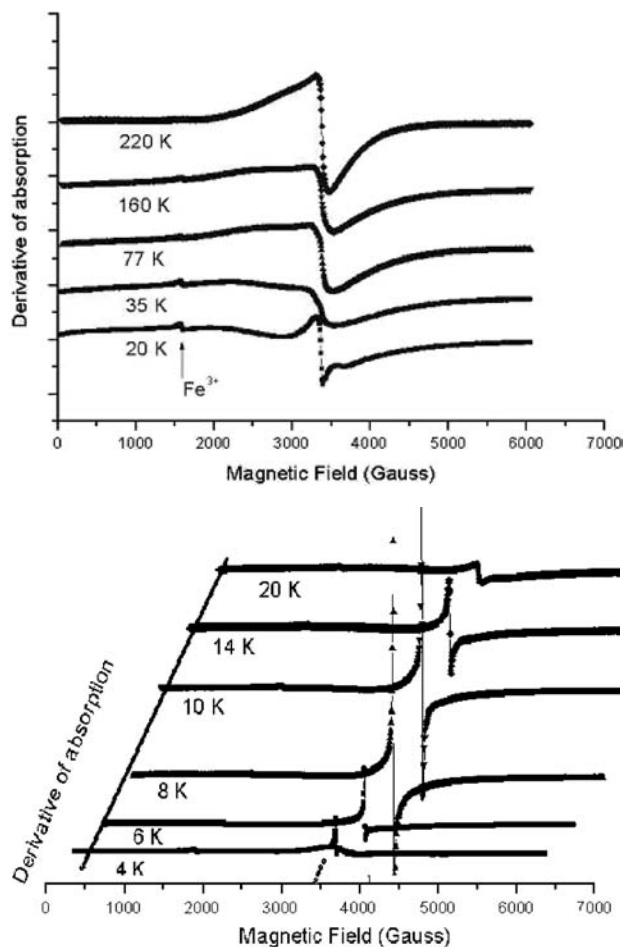


Figure 27. The ESR spectra for Fe_3O_4 ferrofluid measured at various temperatures between 220 K and 4 K. The spectra below 20 K are canted to express the same resonance position without turbidity of signals. Reprinted with permission from [232], C. T. Hsieh and J. T. Lue, *European J. Phys. B* 35, 357 (2003). © 2003, EDP Sciences.

respectively. The spin susceptibility which is proportional to the integration of the intensity is hidden in the very broad spectrum line at low temperatures. The line width of the paramagnetic resonance signal arising from quantum fluctuations is independent of temperatures. Two prominent critical points associated with the classically thermally driven from SPR to blocked SPR and the quantum tunneling from magnetic long-range order to quantum paramagnet are appraised. The sharply narrowing down of the linewidth for quantum SPR may be attributed to largely reducing of the domain size by quantum tunneling.

Finally we compare the ESR results to the magnetization measurements governed by apparently slower observing time scales. To justify the existence of SP, blocked SP and quantum SP states at various temperatures, we used the Co-ferrite nanoparticles which have a much larger anisotropic field. The magnetization for CoFe_2O_4 ferro fluid as a function of temperatures was measured by a MPMS2 superconducting quantum unit interference device (SQUID) as shown in Figure 29. Above T_B the particles are superparamagnetic where the field cooled (FC) and zero field cooled (ZFC) curves merge that elucidates the alignment of the

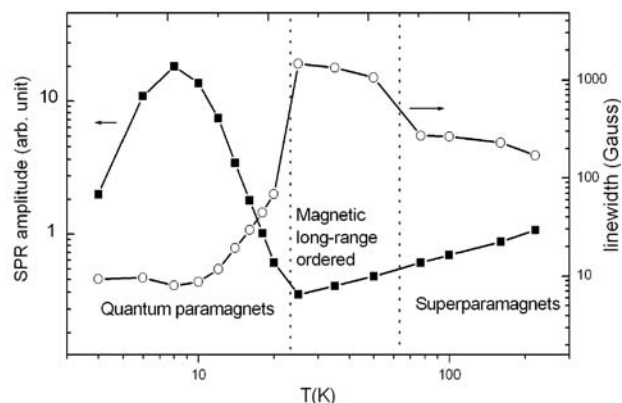


Figure 28. The ESR line widths and amplitudes at various temperatures for Fe_2O_3 ferrofluid are displayed to specify three magnetic states. Reprinted with permission from [232], C. T. Hsieh and J. T. Lue, *European J. Phys. B* 35, 357 (2003). © 2003, EDP Sciences.

anisotropic spins for the field cooled spectrum. Two remarkable transition points were denoted as T_B and T_c in the ZFC curve to represent the blocking state between 24 K and 11 K and the cross temperature at 11 K. Above T_B , the Co-ferrite nanoparticles exhibit superparamagnetism due to thermal fluctuations of the magnetic moments while blocked to the original ferrimagnetic order at temperatures below T_B .

We have studied the ESR response of ferrofluid Fe_3O_4 samples as a function of temperature [232]. The experimental data can be consistently explained in the framework of a qualitative model of the evolution of the nanoparticle magnetic system with decreasing temperature from the superparamagnetic, to blocked superparamagnetic and finally to the quantum tunneling regime. Size and anisotropy dependence of the transition temperatures agree with the Heisenberg model with strong

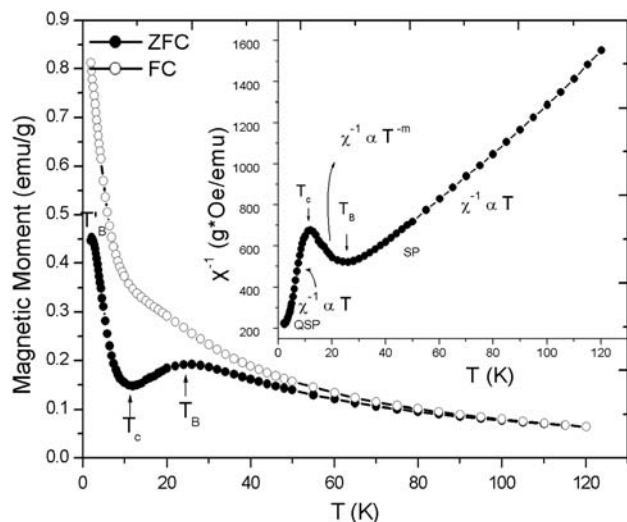


Figure 29. Temperature dependence of the magnetization of CoFe_2O_4 measured in modes of FC at an external field of 10G (open circles) and ZFC (closed circles). The inset illustrates the reciprocal susceptibility versus T. Two remarkable points, T_B , and T_c , indicate the transition from SP to blocked SP, and from blocked SP into quantum SP. Reprinted with permission from [227], C. T. Hsieh and J. T. Lue, *Phys. Lett. A* 36, 329 (2003). © 2003, Elsevier.

easy-plane anisotropy. The critical temperatures of the quantum superparamagnetic resonance spectra are also proportional to the intensity of transverse magnetic field in accord to the *Heisenberg model in the external transverse field*. Plausibility of a quantum phase transition might occur as a consequence of the critical exponent $\gamma = 1.7 \sim 2.3$. More evidences for clues of this eventual QT should be provided such as measurements of heat capacity and ac susceptibility. The possibility of QPT in magnetic nanoparticles is vital in theoretical and experimental point of view.

2.4.2. Domain Walls in Thin Magnetic Films

For thin magnetic films, the mostly interested problems are magnetic domain formation and the related magneto-resistance. An magnetic force microscopy MFM with a high image resolution is required for both scientific explorations and technical applications associated with the study of highly dense thin-magnetic-film recording media, whose density is limited by domain walls and ripple structures that cause noises in the feedback signal. Magnetization perpendicular to the surface has been found in the ultra-thin films of sandwich structures such as Fe/Ag [233], (Co/Pt)_N[234], (Co/Au)_N[235], and Cu/Ni/Cu(001) [236] where N is the number of repetition layers. In a magnetic field parallel to the film plane, the magnetic domain size initially decreases and then increases as the film thickness increases. The in-plane magnetization for films with thicknesses greater than five monomolecular layers (ML) reveals a reduction of the magneto static energy. In MFM images, the distribution of magnetization parallel or anti-parallel inside the walls appears dark or bright lines, respectively. Various domain structures, including Bloch walls, Neel walls, Bloch lines [237], cross-ties [238, 239], and 360° walls [240] have been observed in Co, Fe, and permalloy films [241]. The formation mechanism for the 360° domain walls has not yet been clearly understood. The 360° domain walls are generally believed to form normally near the defects where the interaction between a wall and an inclusion is strong [241, 242] In spite of many reports on MFM images of magnetic thin films, an investigation of a high resolution (with sizes) of domain structure is still desirable.

A demarcation occurs when the Ni film thickness is around 50 nm, at which film thickness, Neel walls are usually observed. Striped Bloch walls are dominated for thicker films. Both the domain area of the Neel wall and the spaces between the striped lines in the Bloch walls are proportional to the square root of the film thickness. The periodic spaces between the striped domains increases with the applied field perpendicular to the surface. The spaces become zigzag for thick films. The formation of magnetic domain walls crucially depends on the anisotropy energy, the magneto static energy and the mechanical stress of magnetic thin films. Magnetic energies comprise of

- (1) the domain-wall energy E_w due to the exchange energy between nearest neighbors characterized by the exchange coupling constant J (erg/cm);
- (2) the magneto crystalline anisotropy energy E_a expressing the interaction of the magnetic moment with the crystal field characterized by the constant K_v (erg/cm³);

- (3) the magneto static energy E_m arising from the interaction of the magnetic moments with discontinuous magnetization across the bulk and the surface;
- (4) the surface magneto crystalline anisotropy energy E_{ks} resulting from a correction of symmetry broken near the surface characterized by a constant K_s (erg/cm²); and
- (5) the magneto-restrictive energy E_r arising from mechanical stress or defect-induced force on the film resulting in an introduction of effective anisotropy into the system characterized by K_m (erg/cm³).

A competition of above energies implies various domain walls including Bloch walls, Neel walls, asymmetric Bloch walls, Bloch lines, cap switches, and 360° domain walls. For stripe domains, the magnetic potential follow the Laplace function within the periodic stripe spaces, and the static magneto-energy is expressed as [244]

$$\epsilon_m = \frac{I_s^2 d}{\pi^2 \mu_0} \sum_{n=0}^{\infty} \frac{1}{n^2 d} \int_0^d \sin n \left(\frac{\pi}{d} \right) x dx = \frac{2I_s^2 d}{\pi^3 \mu_0} \sum_{n:odd}^{\infty} \frac{1}{n^3} = 5.40 \times 10^4 I_s^2 d \text{ J/m}^2 \quad (22)$$

where I_s is the saturation magnetization, d is the period of stripe lines, and μ_0 is the permeability. The domain wall energy for thin stripe domains can be approximated as

$$\epsilon_w = \frac{\gamma \ell}{d} \quad (23)$$

where γ is the surface energy per unit area of the domain and ℓ is the film thickness. Neglecting the anisotropic energy for stripe domains, the minimizing of the free energy implies the most probable width of the domain walls as

$$d = 3.04 \times 10^{-3} \frac{\sqrt{\gamma \ell}}{I_s} \quad \text{in MKS unit of } d \propto \sqrt{\ell} \quad (24)$$

In thick films inherited with Bloch walls, considering the finite width for spins that rotate from one direction to the opposite direction, the wall energy E_w including the exchange energy E_{ex} and anisotropic energy within the Bloch walls existed in thick films is

$$E_w = E_{ex} + E_a = \frac{\pi^2 JS^2}{Da} + \frac{K_1 D}{2} \quad (25)$$

where S is the spin, D is wall thickness, a is the lattice constant, and K_1 is the anisotropic field. A minimize of E_w with respect to D implies an equilibrium value of

$$E_w = \pi(AK_1)^{1/2}, \quad \text{and} \quad D = \pi \left(\frac{A}{K_1} \right)^{1/2} \quad (26)$$

where $A = (2JS^2)/a$. With the value of K_1 , we can evaluate the wall thickness D .

For magnetic thin films of thickness larger than 5 monolayers (ML), the magnetization prefers to lie on the plane to reduce the magneto static energy exhibiting the Bloch wall with the total magnetic energy as

$$E_B = E_m + E_w = A \left(\frac{\pi}{D} \right)^2 D + \frac{K_1}{2} D + \frac{2\pi D^2}{\ell + D} M_c^2 \quad (27)$$

where M_c is the effective magnetization perpendicular to the domain plane. The magnetization for Bloch walls occurring in thick films is normal to the surface while that for Neel walls occurring in thin films is parallel to the film surface. The Neel walls prevail to minimize the free energy at sufficiently low thickness to wall-width ratio. The total magnetic energy for Neel walls is

$$E_N = E_m + E_w = A \left(\frac{\pi}{D} \right)^2 D + \frac{K_1}{2} D + \frac{\pi D \ell}{D + T} M_S^2 \quad (28)$$

Asymmetric Bloch wall contains a Bloch core in the film center surrounded by a Neel surface cap [23]. The Bloch line behaves such that the wall contrast changes abruptly from bright to dark within a distance of 1 nm [245]. No micromagnetic theory of Bloch lines has been established. A cap switch undergoes a change of the sense of the rotation of wall surface magnetism ensuing a change in Kerr contrast. A 360° domain means that the magnetization rotates 360° within a wall.

The structure of the magnetic domain changes in complying with the applied external field to balance the increment of the work due to domain wall displacement. The stripe walls in a sufficiently high field become zigzag resulting in increasing the negative wall energy to balance the static energy. The radius of curvature r of the domain wall relates to the magnetic pressure on the wall as

$$\frac{\gamma}{r} = 2I_S H \cos \theta \quad (29)$$

where γ is surface energy density on the wall, and θ is the cant angle between the external field H and the normal of the film. The wall changes from stripe to zigzag for $r = \ell/2$ suggesting the estimated critical value of H .

Magnetic domains are of various kinds, and competitively contribute to the anisotropy energies. The transition region between the domains, called the domain wall, is not continuous across a single atomic plane. Profiles of a domain wall can be defined according to the sign of the magneto static interaction between the local surface position and the tip.

The AFM topography and the corresponding MFM images for Ni films deposited at room temperature is shown in Figure 30. A typical circular domain wall was performed in Figure 30, which had been carried out with several different scan speeds, scan positions, directions and tip magnetizations. An alternative Bloch line was observed in the same plate, which also shows ripples suffered from strong tip-sample interaction as expressed by the micromagnetic calculation [237, 240].

The relationship between the topography and local magnetic properties can be established by a combination of the high surface resolutions of DFM and MFM. The line profile of the wall suppression by local particles as shown in Figure 31 adduces that the surface topography affects the wall formation. The wall terminated by an inclusion as a white dot and indicated by “a”. Domain configurations in general would be disturbed by the presence of particles and domain walls that will be kept away from an inclusion. The arrow “b” indicates a little shift of the Bloch wall with a cap switch due to the presence of a particle. The plausible reason may be that it dissipates less anisotropy energies for

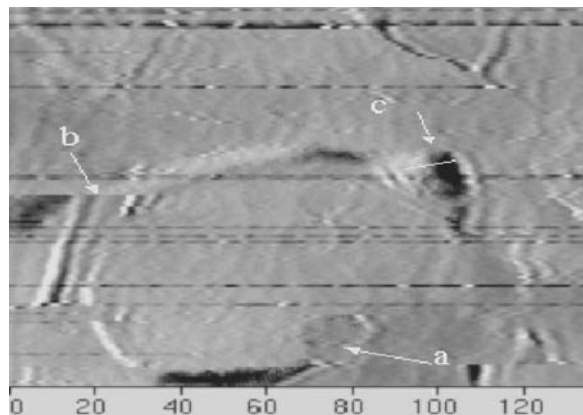


Figure 30. The corresponding MFM image. The dimensions are in nm. Reprinted with permission from [224], C. T. Hsieh et al., *Appl. Surf. Sci.* 252, 1899 (2005). © 2005, Elsevier.

the wall to walk in thin films. Another explanation is that the inclusion prevents the occurrence of the wall-cross. The tilting of the wall is due to the local inclined anisotropy. The arrow “c” illustrates that the spin orientation change by 180° degrees under a lateral distance of only 3 nm. It also reported in references [241–242] showing a lateral distance only of 1–2 nm. The basic assumption of micromagnetic theory, i.e., a small canting angle between adjacent Heisenberg spins, is no longer valid. The formation of this alternative Bloch line seems to be originated from the rotational nature of magnetization due to stress, oblique anisotropy, impurity, vacant space, and irregular ingredients.

The domain size increases with the film thickness according to the formula $d \propto \sqrt{\ell}$ [243] as proposed by Kittel [244] as expressed in Eq. (3) where d is the domain size, and ℓ is the film thickness as developed in Figure 32. In deriving this formula, Kittel considered only the magneto static energy, the exchange energy, and the magneto crystalline anisotropy energy. This simplified theory can not express the deviation of the results of the experiment from the theoretical curve for the domain size of about $291 \text{ nm} \pm 25 \text{ nm}$ at film thickness of 75 nm. Neglecting the anisotropy caused by the existence of defects and inclusions in thicker films may be responsible for the deviation from the ideal square-root law.

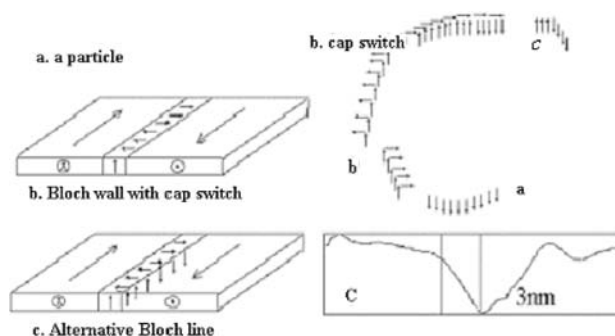


Figure 31. The corresponding line profile and spin orientations. Reprinted with permission from [224], C. T. Hsieh et al., *Appl. Surf. Sci.* 252, 1899 (2005). © 2005, Elsevier.

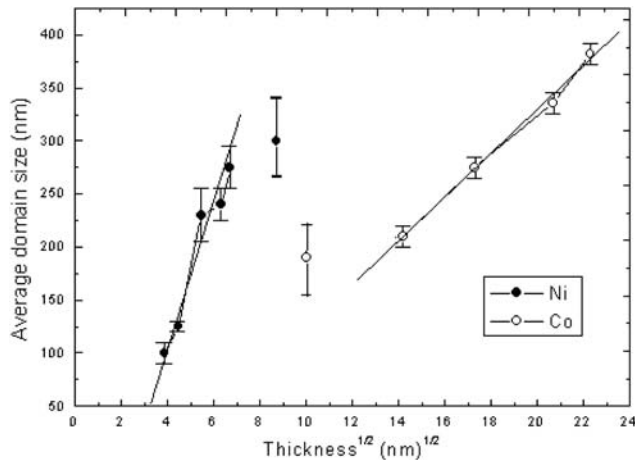


Figure 32. A plot of domain sizes as functions of the square-root of nickel and cobalt film thickness. Reprinted with permission from [224], C. T. Hsieh et al., *Appl. Surf. Sci.* 252, 1899 (2005). © 2005, Elsevier.

2.4.3. Magnetoresistance in Thin Films

Researches in domain wall resistance have grown dramatically in recent owing to the great advances in the fabrication of magnetic memory devices. Specifically, large negative magnetoresistance (MR) observed at room temperature in cobalt films behaving with strip-domain walls was hotly investigated and reported in terms of giant domain-wall (DW) scattering that contributes to the resistivity. Measurements of resistivity for currents conducting parallel (CIW) and perpendicular to DW's play the essential role of MR studies. Two excellent reviews concerning the domain-wall scattering of magneto resistance were reported [245, 246]. Berger [245] proposed that on account of the shorter wavelength of conduction electrons in comparing to the domain wall-width, the electronic spin follows the local magnetization adiabatically and gradually as it traverses across the wall. Whereas Cabrera and Falicov [246] treated the problem of domain-wall-induced electrical resistivity in iron analytically by examining the difference in reflection coefficients at a domain wall for up and down spin electrons. The domain wall essentially presents a potential barrier where the barrier heights are different for the two-spin channels owing to the existence of exchange field.

The magnetoresistance (MR) measurement yields detailed information concerning small magnetization changes. Recently, several groups studied the width dependence of the magnetization reversal process in narrow ferromagnetic wires by measuring the MR, and reported that the coercive force and the switching field are proportional to the diamagnetic field along the wire axis [247–249]. Figure 33 represented the MFM images with a $5\ \mu\text{m} \times 5\ \mu\text{m}$ size of magnetic domains for a 100 nm-thick Ni film under various directions of magnetic fields. The dark and bright contrasts can be identified with the up and down magnetic domains showing (a) straight line distributed along the y -direction (parallel to the strip-line) for $H = 0$, (b) domain-width increased for applying $H = 1.5\ \text{T}$ along the y -direction, (c) the strip-domain oriented to the x -direction (transverse to the strip-line) for applying a $H = 1.5\ \text{T}$ perpendicular to the y -direction, and (d) the stripe domains

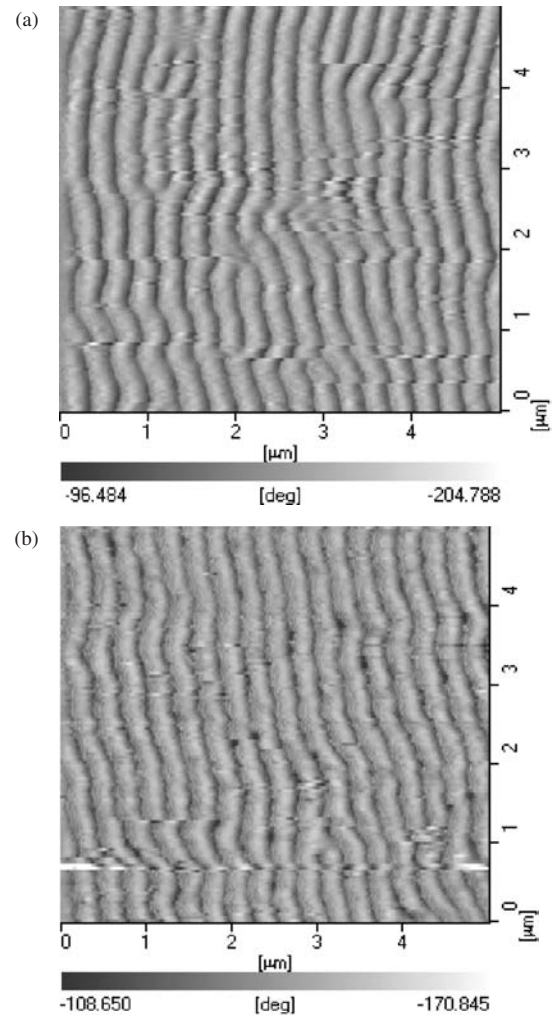


Figure 33. Figures represented the MFM images with a $5\ \mu\text{m} \times 5\ \mu\text{m}$ size of magnetic domains for a 100 nm-thick Ni film (a) virgin, (b) with a magnetic field parallel to the strip line, and (c) with field perpendicular to the strip line, respectively. Reprinted with permission from [224], C. T. Hsieh et al., *Appl. Surf. Sci.* 252, 1899 (2005). © 2005, Elsevier.

changed to a labyrinth shape for the applied field along the z -direction (perpendicular to the surface), respectively. The MFM images for the 800 nm-thick Co film are shown in Figure 2 with domain structures as given by (a) straight lines distributed along the y -direction, and (b) the stripe domain became a bubbly shape under a bias magnetic field of 1.5 T in the y -direction, respectively.

The temperature dependence on the resistivity for the Ni film with a thickness of 250 nm measured at 20 to 100 K with a DC current of 1 mA is shown in Figure 34. The upper curve a shows the resistivity with the beam current transverse to the domain walls (CPW) without applying external magnetic fields. The conductance is 15% smaller than when the current is parallel to the domain walls (CIW) as sketched in curve b. The CPW value is even 32% smaller than that under an applied magnetic field of $H = 1.5\ \text{T}$ as dictated in curve c. Here the transverse current in the legend refers to the current perpendicular to the domain walls and the longitudinal current refers to the current parallel to the domain walls, respectively.

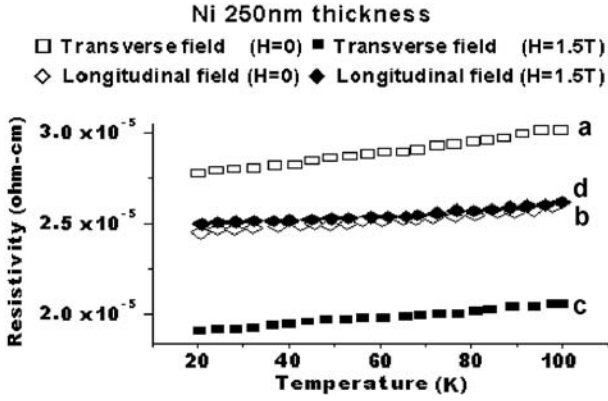


Figure 34. The R–T curves of the 250 nm-thick Ni film with different domain-wall structures and current flow directions. The magneto-resistivities reduce by 15% when the current is parallel instead of transverse to the domain wall and reduces by 32% in the transverse current when the width of stripe domain is increased under a magnetic field of 1.5 T.

Cabera and Falicov [24612] considered the paramagnetic and diamagnetic effects that introduce additional resistance beyond that present in the domains. The parametric effect arisen from the reflection of incoming electron waves by the ferromagnetically ordered domains as they entered the twisted spin structure of a wall, and the diamagnetic effect due to the zigzag character of the orbital motion of electrons when they pass between the up and down spin regions of the domain. This diamagnetic effect is the source of a negative MR. The resistivities of current parallel to the domain wall (CIW) and perpendicular to the domain wall (CPW) are given theoretically on account of boundary scattering as given by [250, 251]

$$\rho_{\text{CIW}} = \rho_0 \left[1 + \frac{\xi^2 (\rho_0^\uparrow - \rho_0^\downarrow)^2}{5 \rho_0^\uparrow \rho_0^\downarrow} \right] \quad (30)$$

$$\rho_{\text{CPW}} = \rho_0 \left[1 + \frac{\xi^2 (\rho_0^\uparrow - \rho_0^\downarrow)^2}{5 \rho_0^\uparrow \rho_0^\downarrow} \left(3 + \frac{10\sqrt{\rho_0^\uparrow \rho_0^\downarrow}}{\rho_0^\uparrow + \rho_0^\downarrow} \right) \right] \quad (31)$$

The magneto resistance ratio R due to walls, which is defined as

$$R_{\text{CIW}} = \frac{\rho_{\text{CIW}} - \rho_0}{\rho_0} = \frac{\xi^2 (\rho_0^\uparrow - \rho_0^\downarrow)^2}{5 \rho_0^\uparrow \rho_0^\downarrow} \quad (32)$$

$$\frac{R_{\text{CPW}}}{R_{\text{CIW}}} = 3 + \frac{10\sqrt{\rho_0^\uparrow \rho_0^\downarrow}}{\rho_0^\uparrow + \rho_0^\downarrow} \quad (33)$$

where ρ_0^s is the resistivity for spin states s of the ferromagnetic material, $\rho_0^{-1} = 1/\rho_0^\uparrow + 1/\rho_0^\downarrow$ is the conductivity of the ferromagnet without the appearance of domain walls, $\xi \equiv \pi \hbar^2 k_F / 4mdJ$, and d is the domain wall width.

To estimate the MR due to wall scattering, Levy [250] chose the commonly accepted values of Fermi wave vector $k_F = 1 \text{ \AA}^{-1}$, the exchange splitting energy $J = 0.5 \text{ eV}$, and

$\rho_0^\uparrow / \rho_0^\downarrow = 5\text{--}20$ for typical ferromagnetic materials of Co, Fe and Ni at room temperature.

The $MR_{\text{CPW}} = -32\%$ of the 250 nm-thick Ni film measured at temperature 100 K is shown in Figure 35(a) for the current transverse to the domain wall under zero magnetic field, when a saturation magnetic field $H = 1.5 \text{ T}$ is applied. Physically, several magnetization dependent scattering processes influence the electrical transport. This fact can be summarized in a general formula expressing the components of the electric field generated by a current density flowing through a homogeneous ferromagnet (providing the Matthiessen's rule is valid) by neglecting the extraordinary Hall effect and the possible deviation of the current lines while crossing different domains, such as that induced by the Hall effect [245]. The electric field is given by [252]

$$\vec{E} = \rho(B)\vec{J} + \rho_{\text{AMR}}(\vec{\alpha} \cdot \vec{J})\vec{\alpha} + \rho_0 \vec{B} \times \vec{J} + \rho_{\text{wall}}\vec{J} \quad (34)$$

with \vec{M} the magnetization, $\vec{\alpha}$ the unitary vector along the electric-field direction, and \vec{B} the internal magnetic induction vector. The first term represents the usual longitudinal resistance contribution, which varies like B^2 at low temperature (Lorentz contribution) and decreases almost linearly with B at higher temperatures (magnon damping [253]). The second term is the anisotropic magneto resistance (AMR) along the magnetization direction. Its projection perpendicular to the current lines is called the planar Hall effect. The third term is the standard Hall effects composed of the ordinary effect proportional to B and the last contribution is related to the resistance due to spin scattering in domain walls. All of these items contribute to the negative GMR by 32%.

For the 800 nm-thick Co film as shown in Figure 36 (a), the $MR_{\text{CPW}} = 40\%$. From the MFM domain configuration, we can expect that the domains becoming bubbly shape increase the scattering probability and induce the positive GMR by 40%. The conductivities increase as the magnetic field increases when the magnetic field is applied along the electron transport direction at room temperature and 4 K as shown, respectively, in Figures 37(a) and (b). The conductivity increases steadily with the increase of magnetic field at high temperatures on account of the reduction of the radius

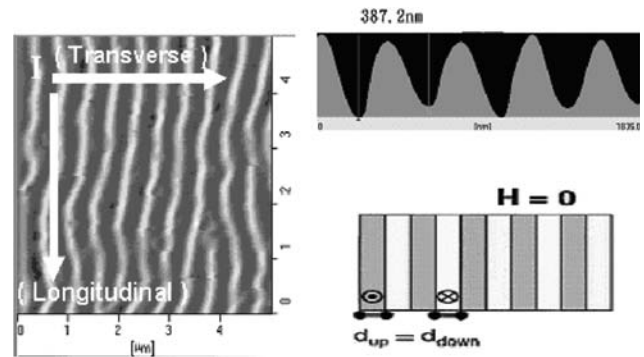


Figure 35. The MFM domain configuration of above Ni film for (a) $H = 0$, (b) along the y -direction (\uparrow) under a bias magnetic field of 1.5 T, respectively. The stripe domain-width increases and fewer domain walls are remnant.

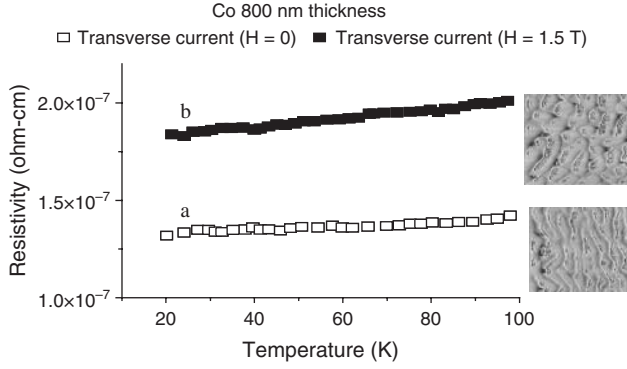


Figure 36. The R-T curve of the 800 nm-thick Co film with different domain wall structures under a transverse current. The resistivity increases 40% when the domain wall becomes bubbly shape from a straight line under a bias magnetic field of 1.5 T.

of the spiral motion of electrons that escape from surface scattering implying elongation of the mean free path. The MR measured at 4 K decreases rapidly at the beginning, which is presumed to be arising from the largely enhancement of electron scattering with the boundaries of Co wire at the presence of a small magnetic field at low temperatures.

Figures 37(c) and (d) show the M-R measurement when the magnetic field was applied along the y-direction at room temperature and at 4 K. The conductivity does not change obviously as the magnetic field increases. The Sondheimer oscillation appears for magnetic field being nearly normal to

the surface due to periodic striking the surface for electrons traveling in circular motion on a plane canting to the surface [254]. Figure 37(e) shows the MR measurement when the magnetic field was applied along the z-direction at room temperature. The conductivity decreases slightly as the magnetic field increases in comparing with the result for the field being applied along the transverse direction. Apparently the MR curve as portrayed in Figure 37(e) is not always smooth but with bumps with the aperiodic oscillation much slower and irregular than the Aharonov-Bohm oscillation [254]. At this time we are unable to address this phenomenon clearly, which is tacitly assumed this fact to be arisen from the quantum size effect that results from the phase coherence in the electron waves scattered by different defects, and the distribution of the phase relationships by the magnetic field [254] and the domain-wall trap as reported in [247].

Concerning the reduction of the radius of the electron spiral motion under magneto size effect, the ratio of the conductivities for thin and thick films as the magnetic field is applied longitudinal to the current are [255]

$$\frac{\sigma_f}{\sigma_0} = 1 - \frac{3}{16k} \left[2 - \frac{k_r^2}{4k^2 + k_r^2} (1 + e^{-2\pi k/k_r}) \right] \quad (35)$$

$$\frac{\sigma_f(B) - \sigma_f(B=0)}{\sigma_f(B=0)} = \frac{1 - \frac{3}{16k} \left[2 - \frac{k_r(B)^2}{4k^2 + k_r(B)^2} (1 + e^{-2\pi k/k_r(B)}) \right]}{1 - \frac{3}{16k} \left[2 - \frac{k_r(B=0)^2}{4k^2 + k_r(B=0)^2} (1 + e^{-2\pi k/k_r(B=0)}) \right]} - 1 \quad (36)$$

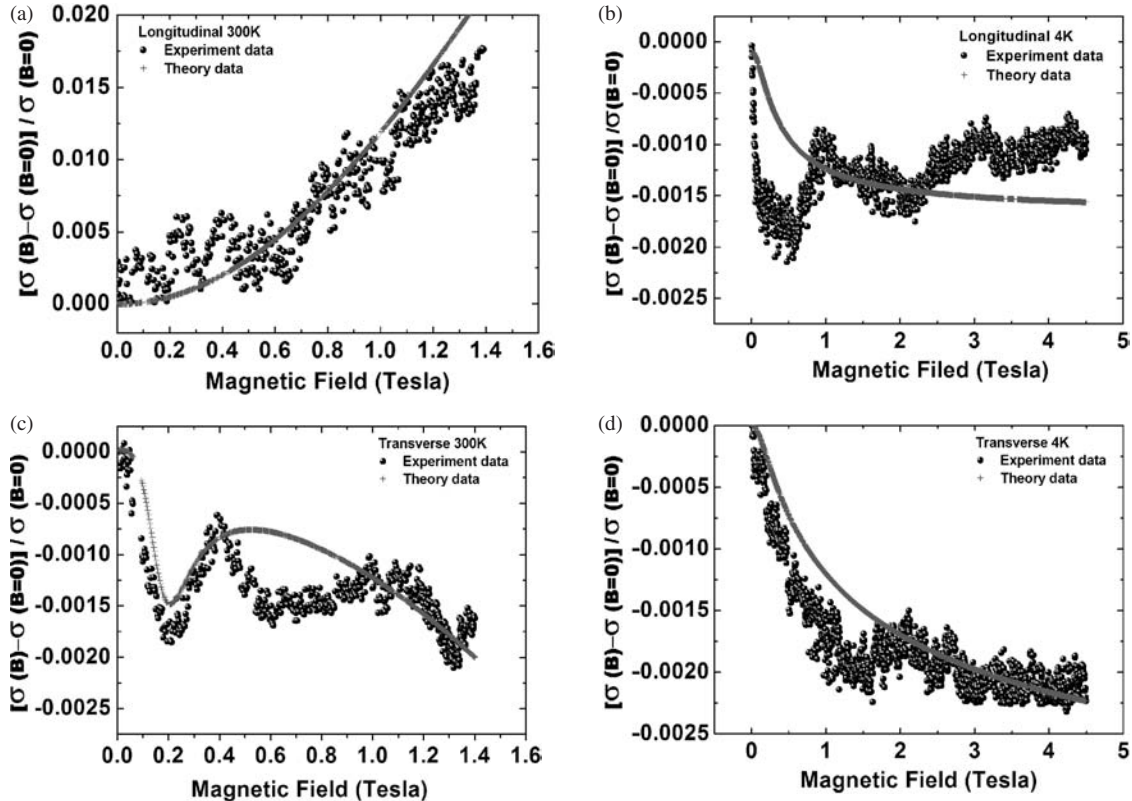


Figure 37. The experimental and theoretical values of the ratio of $\sigma_f(B) - \sigma_f(B=0)/\sigma_f(B=0)$ for (a) the magnetic field being applied along the transport x-direction at 300 K, (b) at 4 K, (c) the magnetic field being along the y-direction at 300 K, and (d) at 4 K, respectively.

where $k = d/\lambda_0$, and $k_r = d/D$, D is the radius of electron spiral motion, and λ_0 is the electron transport mean free path. We suppose $\lambda_0 \cong 10$ nm and 100 nm, at room temperature 300 K and 4 K, respectively. Samples studied in this work have the Co wire thickness of 15 nm, which implies the reduction of k from 1.5 to 0.15 as temperature decrease from 300 K to 4 K resulting from the increase of mean free path at low temperatures. The solid lines in Figure 37 show the experimental and theoretical data derived from Eq. (36) at temperature 300 K and 4 K, respectively. We can see that the experimental values are closed to the theoretical curves. The implemented theoretical data of the radius for the electron spiral motion is derived from the Faraday's law expressing as $D = (mv)/(qB) = m/(qB) \cdot q/m \cdot (\Gamma(s + 5/2))/(\Gamma(5/2)) \cdot \tau_o \cdot E$; where s is a characteristic exponent, and τ_o is a relaxation time constant.

For the case of applying the transverse magnetic fields, the conductivity ratio is

$$\frac{\sigma_f}{\sigma_0} = \frac{A^2 + \xi^2 B^2}{A} \quad (37)$$

The conductivity deviation ratio is

$$\frac{\sigma_f(B) - \sigma_f(B=0)}{\sigma_f(B=0)} = \frac{\frac{A(B)^2 + \xi(B)^2 B(B)^2}{A(B)}}{\frac{A(B=0)^2 + \xi(B=0)^2 B(B=0)^2}{A(B=0)}} - 1 \quad (38)$$

where

$$A = \frac{3}{2} \left\{ -\frac{1}{2} \mu + \mu^2 + \frac{\mu}{2} (1 - \mu^2 + \xi^2 \mu^2) \ln \left[\frac{(1 - \mu^{-1})^2 + \xi}{1 + \xi^2} \right] \right. \\ \left. - 2\xi \mu^3 \tan^{-1} \left\{ \frac{\xi}{\mu} \cdot \frac{1}{\xi^2 + 1 + \mu^{-1}} \right\} \right\} \\ B = \frac{3}{2} \left\{ -\mu^2 + \mu^3 \ln \left[\frac{(1 - \mu^{-1})^2 + \xi}{1 + \xi^2} \right] \right. \\ \left. + \frac{\mu}{\xi} (1 - \mu^2 + \xi^2 \mu^2) \tan^{-1} \left\{ \frac{\xi}{\mu} \cdot \frac{1}{\xi^2 + 1 + \mu^{-1}} \right\} \right\} \\ \xi = \lambda_0/D \quad \mu = k[\ln(1/p)]^{-1}$$

With the parameters giving by $p = 0.13$, $\mu = 0.75$ and $p = 0.004$, $\mu = 0.018$ at temperature 300 K and 4 K, respectively, we can calculate the conductivity deviation ratio. The theoretical curves derived from Eq. (38) were illustrated in Figure 37(c) and 37(d), which agree satisfactorily with the theory except the bending curve that occurs near at $B = 0.6$ T at temperature 300 K. This smallness of the specularly parameters p is attributed to the strong surface scattering for the ion-sputtered films. The largely reducing of the p values at low temperatures results from the surface diffusion of the catastrophic molecular desorption.

2.4.4. Magnet Micro-Strips and Ferromagnetic Resonance for Magnetic Films

The large demand in communication and video applications intrigues us an impetus to develop the design of monolithic microwave micro-strip circuits. Microwave techniques allow high sensitivity measurement of the dependence of the conductivity of thin magnetic films on temperature [256–258]

and magnetic field [259–261]. A permissive investigation on the resonance frequency tunable by magnetic or electric field for filters is desired [259]. Measurement of the magnetic field dependence of the resonant frequency shift of a microwave micro-strip has been performed by Tsutsumi et al. [260]. There have been a lot of studies on the measurement of the complex permeability over a broad frequency band [262]. The dynamic susceptibility deduced from the ferromagnetic resonance spectra in magnetic films with a non-uniform magnetic configuration is reported [263].

The response of the magnetic moment M under an effective field H_{eff} is described by the Landau-Lifshitz equations of motion [264] as

$$\frac{dM}{dt} = -\gamma(M \times H_{\text{eff}}) - \frac{4\pi\mu_0\lambda}{M^2} M \times (M \times H_{\text{eff}}) \quad (39)$$

where γ is the gyromagnetic ratio, and λ is the damping factor [265] in units of s^{-1} . In the static case the total magnetic moment has to be parallel to the total effective field, the magnetic anisotropy energy density E_a is related to the effective field by [266]

$$H_{\text{eff}} = -\frac{\partial E_a}{\partial M} \quad (40)$$

where $E_a = K_{u1}(\alpha_1^2\alpha_2^2 + \alpha_2^2\alpha_3^2 + \alpha_3^2\alpha_1^2) + K_{u2}\alpha_1^2\alpha_2^2\alpha_3^2 + \dots$, and $\alpha_1, \alpha_2, \alpha_3$ are the direction cosines of the saturation magnetization with respect to the [100], [010], and [001] crystallographic axes respectively, and K_{u1} and K_{u2} are the second and fourth order terms of the perpendicular uniaxial anisotropic energy. For cubic anisotropy with the easy axis along the [111] direction, the in-plane effective field [267] is approximated as $H_{\text{eff}} \approx 4K_{u1}/3M_s$ where M_s is the saturation magnetization. Consider a specimen of a cubic ferromagnetic crystal with ellipsoid anisotropic magnetization, the Lorentz field $(4\pi/3)M$ and the exchange field λM do not contribute to the torque because their vector product with M vanishes identically [268]. In applying a field parallel to the film (the xz plane), we can derive the ferromagnetic resonance (FMR) frequency from Eq. (39) as

$$\omega = \gamma \sqrt{(H_0 + H_a)(H_0 + H_a + 4\pi M)} \quad (41)$$

where H_0 is the external field. Here we have implied the demagnetizing factor [269] for an infinite plane of thin film to be $N_x = N_z = 0$, $N_y = 4\pi$ for the external magnetic field along the xz plane.

A typical micro-strip transmission line is shown in Figure 38 where the geometrical parameters are also described there. For the micro-strip with small insertion loss, a matched 50 ohm transmission line should be considered. In this design we follow the well-known quasi-TEM formulae derived from Wheeler's and other workers [270, 271]. The substrate is a sapphire plate with (0001) orientation and a thickness of 500 μm . The calculated line width w is 430 μm , and the effective dielectric constant ϵ_{eff} is 7.27. The frequency dependence of the effective dielectric constant $\epsilon_{\text{eff}}(f)$ reported by Kobayashi [272] will be incorporated to obtain a more accurate result.

The surface resistance R_s of metallic films is related to the attenuation constant α_c of a stripling, which has been given

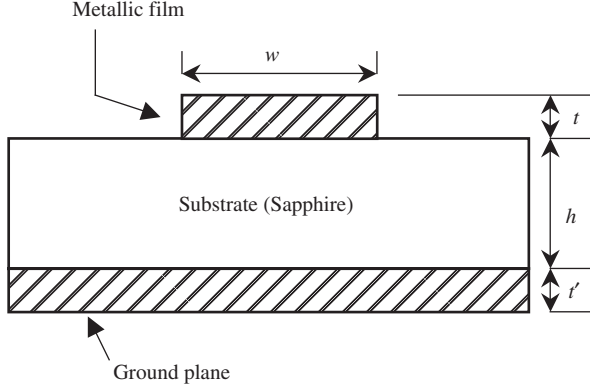


Figure 38. The front view of a micro-strip transmission line. The line width is w , thickness is t , substrate thickness is h , and thickness of the ground plane is t' .

by Pucel et al. [273]. The other losses of the micro-strip resonator are the dielectric loss and the radiation loss. Sapphire is a good insulating dielectric material with loss tangent usually being less than 0.0001. The radiation loss increases with the square of frequency and gap discontinuity of the micro-strip.

A T -junction micro-strip, which has a lower radiation loss than other kinds of microstrips is depicted in Figure 39. Here, the open-ended stub represents a quarter-wave resonator. The resonance condition is

$$f_{\text{res}} = \frac{nc}{4(L + \Delta L)\sqrt{\epsilon_{\text{eff}}(f)}}, \quad n = 1, 3, 5, 7, \dots \quad (42)$$

where ΔL is the effective length of an open end effect. The measured unloaded quality factor, Q_0 , is related to α by

$$Q_0 = \frac{\beta}{2\alpha} \quad (43)$$

where

$$\beta = \frac{2\pi}{\lambda_g} \quad (44)$$

and

$$\alpha = \frac{8.686}{Q_0 \lambda_g} = \frac{8.686 f_{\text{res}} \sqrt{\epsilon_{\text{eff}}(f)}}{c Q_0} \quad (\text{dB/m}) \quad (45)$$

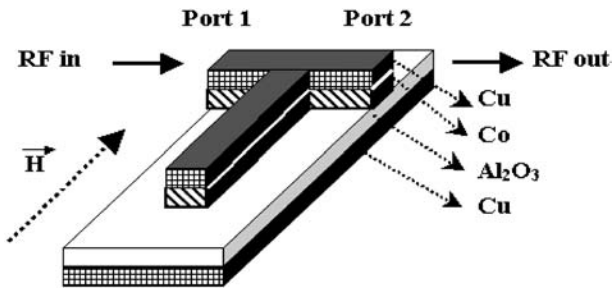


Figure 39. Schematic diagram of a T -junction. The length of the stub is L , and the arrow indicates the direction of the applied magnetic field.

The input impedance of the quarter-wave stub resonator can be characterized as

$$Z_{\text{in}} = R_0 (1 + j2Q_0\Delta) \quad (46)$$

where Δ is defined by

$$\Delta \equiv \frac{\omega - \omega_0}{\omega_0} \quad (47)$$

At resonance, the input impedance will be reduced to the bare dc resistance R_0 . The absolute value of S_{21} thus is given by,

$$|S_{21}| = \frac{2R_0/(2R_0 + Z_c)\sqrt{1 + (2Q_0\Delta)^2}}{\sqrt{1 + (2R_0/(2R_0 + Z_c))^2(2Q_0\Delta)^2}} \quad (48)$$

where Z_c is the characteristic impedance of the micro-strip. The upper and the lower frequencies deviated from the resonant frequency f_0 define the bandwidth $\Delta f = f_2 - f_1$. The resonance peak of S_{21} versus frequency is readily applicable for the determination of the quality factor.

A plot of the resonant frequencies of the co-existed FMR and micro-strip structure modes with respect to the applied fields [274] reveals a nearly straight line making a clue of Eq. (41). The Q factor decreases firstly with the applied fields and then increases at 257 mT as shown, respectively, in Figures 40(a) and 40(b). This field implies that the FMR frequency coincides with the S_{21} resonance frequency that leads the largest microwave field to be dissipated in the side arm.

From the values of the Q factor, we can evaluate the loss due to FMR for resolving the change of attenuating constants at several S_{21} resonance frequencies when sweeping the magnetic fields. The fields at the peak loss correspond to the occurrence of the FMR is the closest to that of the transmission resonance. The sheet resistance can be calculated readily from the transmission loss and is depicted in Figure 41. The conductivity of the nickel film can be accessed accordingly from the multiplication of the film thickness and the sheet resistance Ω/\square . The magneto resistances also have resonant peaks occurring at the FMRs where the attenuation of microwave field is a maximum.

The value of the magnetization M depending on the demagnetization factor that varies with different orientations of the external magnetic field. The demagnetization factors are $N_x = 4\pi$, $N_y = N_z = 0$, for the field parallel to the surface. The resonant frequency $f = \omega/2\pi$ can be plotted almost linearly proportional to the field as shown in Figure 42. In this case, the simulated anisotropic field $H_a \approx 533$ Gauss, while the $M_1 \approx 149$ Gauss. On the other hand for the external field perpendicular to the surface, we have $N_z = 4\pi$, and $N_x = N_y = 0$.

The calculated FMR frequency at different magnetic field for cobalt films is plotted in Figure 43 by the simulated electronic circuits. The linear plot can be fitted with Eq. (41) to solve the anisotropic field H_a and the saturation magnetization M_s . The same plot for nickel film with silver film over coated on nickel films to reduce the radiation loss is shown in Figure 44. The low field region has a better linearity than that plot in Ref. [1] without considering the FMR at zero applied fields. Table 1. dictates the saturation magnetization and anisotropic field for bulk and thin film of Co, and Ni in

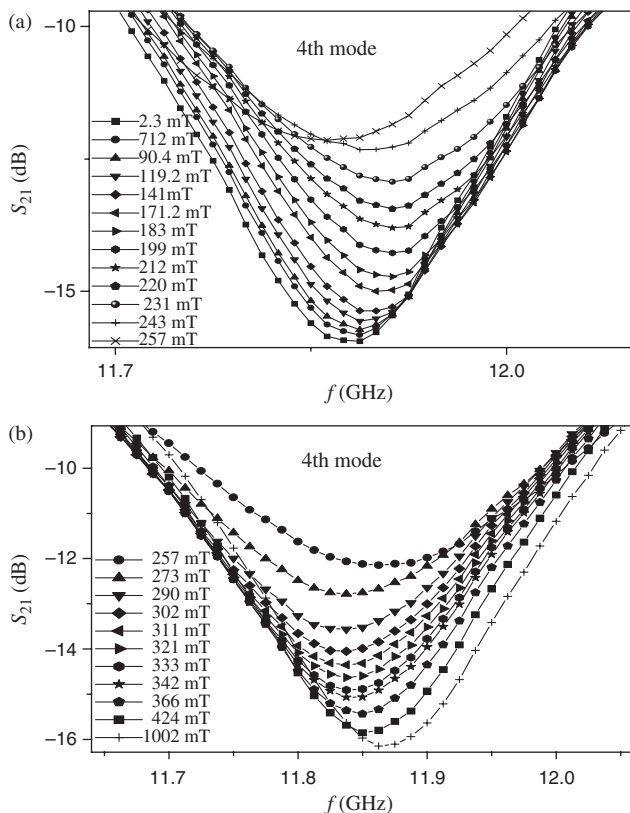


Figure 40. The spectra of the 4th structure mode peak under applied magnetic field for (a) peak rises up under increasing magnetic field, and (b) peak falls down under increasing the magnetic field. Reprinted with permission from [274], S. W. Chang et al., *Meas. Sci. Technol.* 14, 583 (2003). © 2003, IOP Publishing Limited.

which the bold-faced data are measured in this work. This experiment results for thin films are in congruent with the reported bulk values [275].

In this scenario, we found the co-existence of the ferro-magnetic resonance and the structure resonance of a

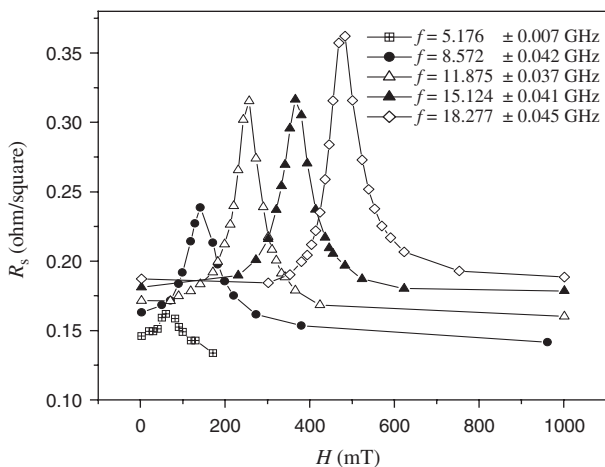


Figure 41. Surface resistance versus applied magnetic field at different structure resonate modes. Reprinted with permission from [274], S. W. Chang et al., *Meas. Sci. Technol.* 14, 583 (2003). © 2003, IOP Publishing Limited.

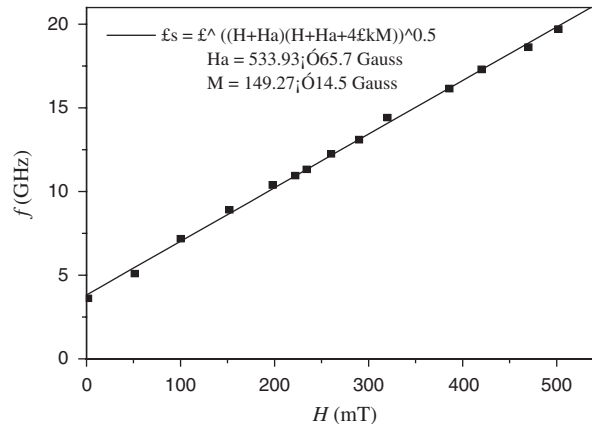


Figure 42. The FMR peak and fitting curve of a meander micro-strip line.

T-microwave micro-strip transmission line under proper values of magnetic fields. The conductivity, the anisotropic field, and the magnetization factor of the magnetic film can be simultaneously determined from the same spectrum. The physical properties of metallic magnetic films can be determined preceding to lay out the spintronic devices. This work advocates a fertilized method to study the magnetic properties of thin films with a simple microwave network analyzer without implementing an involved microwave cavity for the conventional FMR.

2.5. Linear Optical Properties

2.5.1. Quantum Optical Size Effect on Linear Absorption Spectra

Recently, many scientists [276–282] have developed their efforts to the study of the physical properties of metallic nanoparticles and ultra thin films, expecting to obtain a right perspective to the essential features of quantum confined

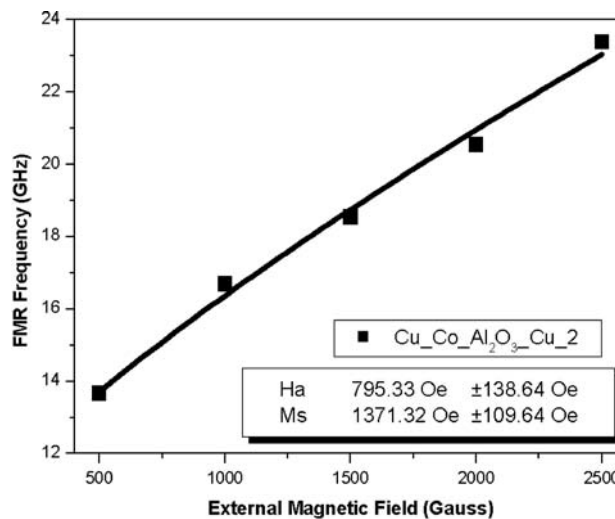


Figure 43. The magnetic field dependence on FMR frequencies for Co films. Reprinted with permission from [274], S. W. Chang et al., *Meas. Sci. Technol.* 14, 583 (2003). © 2003, IOP Publishing Limited.

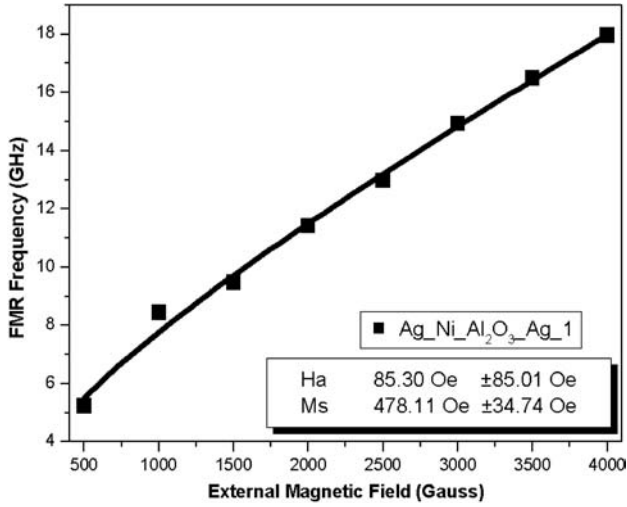


Figure 44. The magnetic field dependence on FMR frequencies for nickel films. Reprinted with permission from [274], S. W. Chang et al., *Meas. Sci. Technol.* 14, 583 (2003). © 2003, IOP Publishing Limited.

electronic systems. Photoluminescence and Raman shift are frequently employed to detect the dependence of resonance frequency shift on the particle sizes. Classical size effect [283–289] embodies in the sample size, which approaches or is smaller than the carrier mean-free-path therein the scattering of carriers with the surface manifests. As the size for metallic particles reduces, the uncertainty principle implies an intrinsic kinetic energy $E_k \sim \hbar^2/m_c^*r^2$, where r is particle diameter; and m_c^* is the mass of electrons, respectively. Whereas, an excess electron induces image charges on the particle surface introducing a Coulomb attractive potential which is proportional to $e^2/\epsilon r$ where ϵ is the dielectric constant. The Bohr radius $r_B = \hbar^2\epsilon/m^*e^2$ for nanoparticles will be defined as that the attractive Coulomb energy is equal to the repulsive kinetic energy. Quantum size effect prevails the classical size effect as the particle is smaller than the Bohr radius.

Many exotic physical properties intrigue with quantum size effect such as the splitting of the continuum conduction band into discrete levels, the electromagnetic field enhancement on the surface, the magnetic properties changes from diamagnetic into paramagnetic, and from ferromagnetic into super paramagnetic. In the linear optical properties, the surface plasma absorption peak reveals blue-shift [277, 290] as the particle size decreases, which can be fully elucidated

Table 1. The saturation magnetization and anisotropic field for bulk and thin films of Co, and Ni [267, 268]. The bold-faced data are measured in this work.

	M_s	H_a
Bulk		
Co	1400 Oe	6470 Oe
Ni	485 Oe	157 Oe
Thin film		
Co	1371 Oe	795 Oe
Ni	478 Oe	85 Oe

by the hard spherical model in inert environment, which appraises the enlargement of energy splitting as the particle size decreases. The abnormal red-shift [291] for metallic nanoparticles embedded in a reactive matrix is retrieved due to the electron diffusion outside the surface. The electromagnetic field can be enhanced at the shallow surface of the nanoparticles, therefore it greatly pronounces the nonlinear optical susceptibility [292–293].

In the visible and near visible light absorption spectra of bulk metals can be satisfactorily expressed by the free electron Drude model [294], which yields high reflectivity and reveals white surface. To a dispersed metallic nanoparticles, the random distribution of normal surface direction of the particles implying the excitation of surface plasmon requiring phase matching condition [295] can be easily complied with. The surface plasmon in resonance to the discrete energy level due to the splitting of quantum size confinement will be absorbed. The shift of absorbed surface plasmon frequency ω_s is inversely proportional to the particle size and thus recounted as the blue-shift. The blue-shift has been observed experimentally by Doremus [296]. The classical size effect presumes the correction to the dielectric function to be due to the scattering of electrons with a spherical boundary, with a reduction of the effective relaxation time by V_F/R [276], which prejudices a red shift. We have proposed a quantum sphere model (QSM), which can successfully portray the dielectric function [297] for metallic nanoparticles. Small particles prepared by inert gas evaporation or chemical sol-gel process usually present a spherical shape under surface tension. The ultra short Thomas-Fermi screen length ($\sim 1 \text{ \AA}$) [298] insures the conduction electron gas confined in the sphere to be non-interaction with each other. We can consider a free electron gas confined in a potential well with $V(r) = V_0$ for r smaller than the radius R and $V(r) = \infty$ for $r > R$. The normalized one-electron wave function is solved to be

$$\begin{aligned} \psi_{nlm}(r, \theta, \varphi) &= \left(\frac{2}{R}\right)^{1/2} \frac{1}{j_{l+1}(\alpha_{nl})} j_l(\alpha_{nl}, r/R) Y_l^m(\vartheta, \varphi) \\ &= R_{nl}(r) Y_l^m(\vartheta, \varphi) \end{aligned} \quad (49)$$

where the Y_l^m 's are the spherical harmonics, and j_l is the Bessel function of order l with the n -th root α_{nl} . The energy of the eigenstate ψ_{nlm} is

$$E_{nl} = (\alpha_{nl})^2 E_0 \quad (50)$$

where $E_0 = \hbar^2/2m_c^*R^2$, m_c^* is the effective electron mass. The asymptotic approximation of the roots of the spherical Bessel function are

$$\alpha_{nl} \cong (2n+1)\frac{\pi}{2}, \quad \text{for large } n. \quad (51)$$

The spacing of neighboring energy levels can be simplified to

$$\begin{aligned} \Delta E_l &= E_l - E_{l-1} \\ &\approx E_0 [(2n+l)^2] \left(\frac{\pi}{2}\right)^2 - E_0 [(2n+l-1)^2] \left(\frac{\pi}{2}\right)^2 \\ &\approx (2l+4n)E_0 \left(\frac{\pi}{2}\right)^2 = \pi(E_0 E_l)^{1/2} \end{aligned} \quad (52)$$

The spacing of neighboring levels depends on $E_0^{1/2}$ which is inversely proportional to the particle radius R , clearly establishes the basic premise of the theory that the absorption light frequency increases as the particle size reduces.

Since the number of conduction electrons in the metallic sphere may be much larger than those occupied in the splitting levels in the quantum well, most of electrons will stay in the continuum band above the well. The dielectric function $\varepsilon(\omega)$ will be contributed from the classical continuum band and from the discrete quantum levels as given as

$$\varepsilon^{\text{total}}(\omega, R) = [\varepsilon_1^f(\omega) + i\varepsilon_2^f(\omega)] + [\varepsilon_1^{QM}(\omega, R) + i\varepsilon_2^{QM}(\omega, R)] \quad (53)$$

The real and imaginary parts of the dielectric function contributed from the quantum levels are

$$\begin{aligned} \varepsilon_1^{QM}(\omega, R) &= \text{Re}[\varepsilon^{QM}(\omega, R)] \approx -\frac{64}{3\pi} \frac{e^2 E_f^{5/2}}{R^2 (\hbar\omega)^4 \sqrt{2m_e^*}} \\ \varepsilon_2^{QM}(\omega, R) &\approx \frac{16}{3\pi} \frac{e^2 E_f^2}{R(\hbar\omega)^3} F(\nu) \end{aligned} \quad (54)$$

where $\nu = E_f/\hbar\omega$ and $F(\nu) = \frac{1}{\nu} \int_{1-\nu}^1 x^{2/3} (x+\nu)^{1/2} dx$.

In general the optical dielectric function cannot be directly measured from experiment, while the absorption spectra can be readily detected. For a composite system, metallic nanoparticles are embedded uniformly in a nonabsorbent glass with dielectric ε_m . The absorption coefficient of metallic spheres embedded in matrix can be derived from Mie's scattering as given by [299, 300]:

$$\alpha = \frac{9\varepsilon_m 3/2f}{c} \frac{\omega\varepsilon_2(\omega, R)}{[2\varepsilon_m + \varepsilon_1(\omega, R)]^2 + [\varepsilon_2(\omega, R)]^2} \quad (55)$$

where α is in units of cm^{-1} and f is the filling factor defined as the ratio of the volume of small particles to the total volume of particles and matrix. A first glance of the maximum absorption occurs when

$$2\varepsilon_m + \varepsilon_1(\omega, R) = 0 \quad (56)$$

The true resonance frequency ω_R will be solved from the differential equation $\partial\alpha/\partial\omega|_{\omega=\omega_R} = 0$. With the classical Drude-like dielectric function substituted into Eq. (55), it can satisfy the experimental data for an average particle diameter above 10 nm [301], however the size dependence of the peak wavelength and half width of the spectra can not be predicted satisfactorily, especially when the particle size is smaller than 10 nm.

The blue shift of the absorption light as the particle size reduces is not the sole experimental results. Recently, Charles et al. [301] observed a remarkable phenomenon containing both the blue and red shifts when the size of small silver particles is below 50 Å. Their results are similar to that of sodium particles on NaN_3 observed by Smithard [302] and by Smithard and Tran [303] for sodium on NaCl. Some authors [304] interposed two surface response functions d_θ and d_r to explain the occurrence of both the blue and red shifts in the same matrix. The authors [277] provided a new approach based on a diffused quantum sphere model to address the conflicted phenomena. The main

strategy of this model is that the energy splitting is larger as the particle size is reduced and the absorbed photon increases. There are some probabilities to find the electron density beyond the spherical boundary (i.e., electron diffusion). The diffusion of electron becomes severe as the particle size squeezed further or the particle are embedded in an active matrix and the dipole transition matrices are reduced to bring out a red shift. There occurs a compromised radius where the shift is at an extreme value.

For a modified QSM with a diffused surface as discussed in the spherical jellium background model (SJBm) [305] with a slight spreading of electron charges outside the boundary, the electron density usually behaves with a Friedel-like oscillation toward the center of the sphere. The total potential $V_T(r)$ evaluated by self-consistent method consists of an electrostatic V_{er} and exchange correlation energies V_{xc} which are expressed as

$$V_{\text{er}}[\vec{r}\rho(\vec{r})] = \int d\vec{r}' \frac{\rho(\vec{r}') - n^+(\vec{r}')}{|\vec{r} - \vec{r}'|} \quad (57)$$

$$V_{\text{xc}}[\rho(\vec{r})] = -\frac{0.611}{r_s(\vec{r})} - 0.033 \ln \left[1 + \frac{11.4}{r_s(\vec{r})} \right] \quad (58)$$

$$\text{and } \rho(\vec{r}) = \sum_i |\psi_i(\vec{r})|^2 \quad (59)$$

In general, the potential near the surface is relevant to the surrounding dielectric medium, which can suppress or diffuse electrons outside the surface. The diffuseness around the spherical boundary of free metallic particles (e.g. Ag/vacuum) is different from that of a metallic surface adsorbed with other molecules. We simply assert that the potentials for weak interaction existing between the reacting metallic particles and the inert matrix such as Ag/Ar [301, 306] system and those for the strong interaction such as Ag/Co and Na/NaCl [302, 304] system, respectively. The corresponding surface plasmon frequency for Na in NaCl matrix is shown in Figure 45. The weak interaction potential is a deep well inside the particle and turns sharply to zero when crossing the boundary. It is seen that the strong interaction across the boundary defined by the background of positive ions in the SBJM. Consequently a large portion of the electronic wave functions confined inside the well protrudes the sharp boundary.

2.5.2. Size Effect on Raman Spectra and Exciton Luminescence

The Raman shift depends on the nano-particle size can be expressed as follows. According to the uncertainty principle, the momentum of any excitation confined in size L will have an uncertainty of \hbar/L . Therefore the momentum conservation of Raman scattering process will relax. The wave-vector of phonons which are allowed in Raman scattering of nano-particles (e.g., the porous silicon) will not be restricted in $\vec{q} = 0$ for bulk phonons, but will be extended from $\vec{q} = 0$ to $\vec{q} = \hbar/L$. The Raman spectrum of nanocrystalline silicon is written as [307]

$$I(I(\omega)) = \int \frac{|C(0, \vec{q})|^2 d^3q}{[\omega - \omega(\vec{q})]^2 + \Gamma_0^2/4} \quad (60)$$

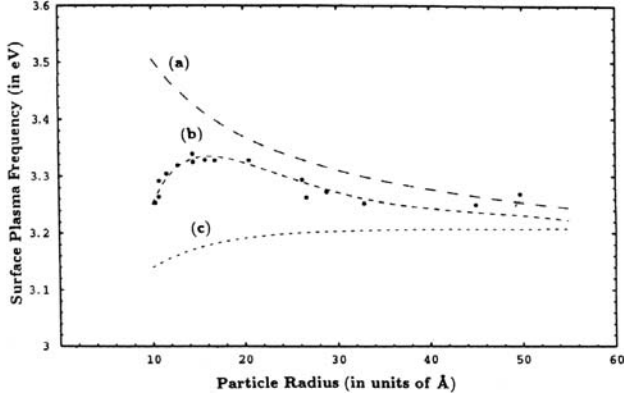


Figure 45. Numerical simulation for the surface plasma frequency ω_s versus particle size R for small sodium particles in NaCl with strong diffuse potentials.

Where $\omega(\vec{q}) = \omega_0 - \alpha \vec{q}^2$, $\alpha = 8.863 \times 10^{17}$ cm, $\omega_0 = 520$ cm^{-1} , and

$$C(0q) = \frac{1}{(2\pi)^{3/2}} \exp\left(-\frac{L^2 \vec{q}^2}{8}\right) \quad (61)$$

Assuming a spherical Brillouin zone with an isotropic phonon dispersion curve, the phonon frequency depends on the wavevector as

$$\omega(\vec{q}) = a + b \cos(\vec{\ell} \cdot \vec{q}) \quad (62)$$

with $\vec{\ell}$ the lattice constant. The calculated spectra of nano PS or various diameters are shown in Figure 46. We observed that the peak shifts from 520 down to 505 cm^{-1} , and the line-width broadens from 7 to 55 cm^{-1} , which are close to the experimental results.

Photoluminescence (PL) occurs when the electrons or atoms of the pumped upper energy levels transit down to the lower states. For semiconductors the PL comes from the recombination of electrons in the conduction band and the

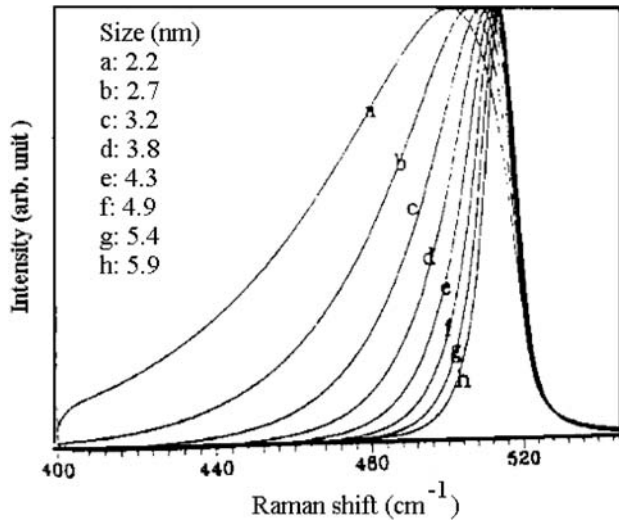


Figure 46. Theoretical Raman spectra for various sizes of porous silicon.

holes in the valence band. When the photon energy $h\nu$ of the incident light is larger than the energy gap E_g of the semiconductor, an electron will be excited to the conduction band and leaving a hole in the valence band forming an absorption bandedge. For photon energy smaller than E_g the emitted electron cannot reach the conduction band whilst attracted by the remnant hole to form an exciton similar to a hydrogen atom. The Hamiltonian of the exciton is

$$H = -\frac{\hbar^2}{2\mu} \nabla_r^2 - \frac{\hbar^2}{2M^2} \nabla_R^2 - \frac{e^2}{\epsilon r} \quad (63)$$

where μ is the reduced mass of electron and hole, M is the sum of the electron and hole masses, $r = r_e - r_h$, R is the coordinate of the center of mass. The exciton eigen energy at n 'th state is

$$E_n = E_G - \frac{\mu e^2}{2\hbar^2 n^2 \epsilon^2} + \frac{\hbar^2 k^2}{2M} \quad (64)$$

Therefore the exciton energies can be lower than the energy gap as shown in Figure 47. The kinetic energy K.E. of excitons increases inversely proportional to the spacing r as given by

$$\text{K.E.} = h\nu - E_g + e^2/\epsilon r \quad (65)$$

The different acceptor and donor levels (shallow or deep) impurity levels in semiconductors [308], yield various exciton spectra as shown in Figure 48. For nano-quantum wells and nano-wires, the exciton binding energy increases with the decreases of well spacing, the exciton spectra, which are usually detected only at low temperatures can be observed at room temperature.

2.5.3. Optical Transmission Through Lattice Tunable Photonic Crystal Composed of Ferrofluids

Faraday rotation is one of the magneto-optical effects profoundly studied for ferrofluids. The magnitude of the angle rotated crucially depends on the wavelength of incident

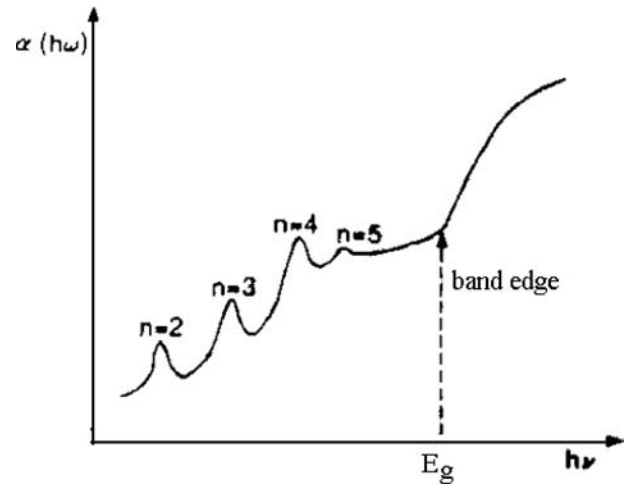


Figure 47. The exciton binding energy diagram and the exciton absorption spectrum.

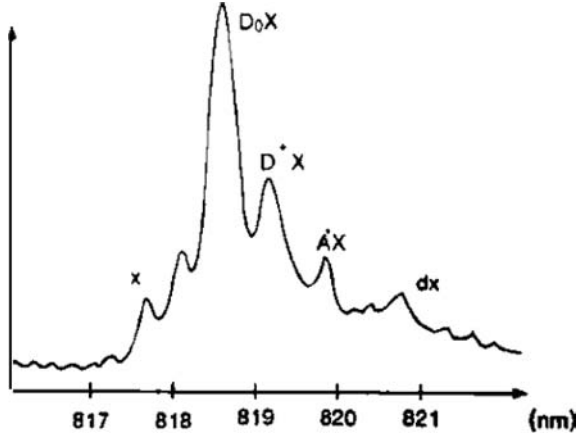


Figure 48. The spectra of various excitons arising from different impurity levels where X is the free exciton, D_0X is the shallow donor exciton, and A^0X is the shallow acceptor exciton.

light, and on the off-diagonal elements of the dielectric tensor for magnetic nanoparticles suspended in fluids. The values of the off-diagonal elements in general was derived from experiments of thin films and directly implemented to analyze the results for magnet fluids [309]. By combining the FMR and ATR experiments, the dielectric constant of magnetic nanoparticles suspended in ferrofluids can be derived by using the effective medium theory.

In this optical system, we have an interface of metal (ϵ_1) and ferrofluids (ϵ_{eff}), on which a p-polarized wave propagates along the x -direction. For a p-wave incident light, the Maxwell's equations in conjunction with the continuity equation yield the dispersion relation.

$$k_x \cong \frac{\omega}{c} \sqrt{\frac{\epsilon_1 \epsilon_{\text{eff}} \mu_{\text{eff}}}{\epsilon_1 + \epsilon_{\text{eff}} \mu_{\text{eff}}}} \quad (66)$$

where k_x is the wave vector along the interface, ω the angular frequency of incident light, μ_{eff} the effective susceptibility of ferrofluids. For a medium (metal) with $\epsilon_1 < 0$ and $|\epsilon_1| > 1$, then $k_x > \omega/c$ and k_{iz} becomes a complex value which is appropriate to excite a surface-propagating wave. The incident field has a maximum intensity on the surface $z = 0$ and decay exponentially in the $\pm z$ directions, which are characterized as surface waves.

Rasa [310] first defined the dielectric tensor for solid particle in its own frame as,

$$\epsilon_p = \begin{pmatrix} \epsilon_2 & i\gamma & 0 \\ -i\gamma & \epsilon_2 & 0 \\ 0 & 0 & \epsilon_2 \end{pmatrix} \quad (67)$$

where ϵ_p the complex dielectric, and the complex $\epsilon_2 = \epsilon'_2 + i\epsilon''_2$ and $\gamma_2 = \gamma'_2 + i\gamma''_2$. In the laboratory frame, with the aid of the rotational matrix [309] and a Boltzman-type averaging [311], the dielectric tensor becomes

$$\begin{aligned} \phi \langle \epsilon'_{p_{ij}} \rangle_L E_j + (1 - \phi) \epsilon_m E_i \\ = \epsilon_{ij} (\phi \langle \epsilon'_{jk} \rangle_L E_k + (1 - \phi) E_j) \end{aligned} \quad (68)$$

where ϵ_m is the scalar real dielectric constant of the basic liquid, E_j is the field along j -th axis, and ϕ is the volume fraction of the solid phase. The dielectric in the laboratory frame is

$$\epsilon_{\text{lab}} = \begin{pmatrix} \epsilon_{11} & i\Gamma & 0 \\ -i\Gamma & \epsilon_{11} & 0 \\ 0 & 0 & \epsilon_{33} \end{pmatrix} \quad (69)$$

where ϵ'_p and ϵ' are defined as $\epsilon'_{p_{ij}} E_j = \epsilon_{p_{ij}} E_{2j}$ and $\epsilon'_{ij} E_j = \delta_{ij} E_{2j}$. The field in the liquid matrix is approximated by the external field while the field within the particles is $E_{2i} = E_i \epsilon_m / [\epsilon_m + (\epsilon_2 - \epsilon_m) n_i]$. In which n_i is the depolarization factor with respect to x , y , and z axes.

Rasa derive the circular birefringence θ_F in the hypothesis of small imaginary parts of dielectric tensor components as given by:

$$\theta_F = \frac{\pi d \text{Re}(\Gamma) (\text{Re}(\epsilon_{11}))^{3/2} + 0.5 \text{Im}(\Gamma) \text{Im}(\epsilon_{11}) (\text{Re}(\epsilon_{11}))^{1/2}}{\lambda_0 (\text{Re}(\epsilon_{11}))^2 + 0.25 (\text{Im}(\epsilon_{11}))^2} \quad (70)$$

where d is the thickness of the sample and λ_0 is the light wavelength in vacuum, the other parameters will be defined in later. In case of linear chains parallel to the magnetic field, n_{\parallel} should be replaced by

$$\langle N \rangle = \frac{\sum_{k=0}^{\infty} k v_0 v_k N_k}{\phi} \quad (71)$$

where v_k is the density of chains with k particles, N_k the depolarization coefficient for a chain with k particles and v_0 the volume fraction of one particle. Equation (70) can be calculated via the effective dielectric elements under a volume fraction and depolarization factor as given by

The ferromagnetic resonance can be succinctly summarized as follows [312]. The resonance field H_r of a sample magnetized to an external field is a function of the g -factor, the magneto crystalline anisotropy field H_a , and the demagnetization field H_d . The anisotropy field can be expressed by $H_a = K/M$, where K is the anisotropy constant and M is the magnetization of the sample. The demagnetization field depending on the shape of the sample can be expressed as $H_d = -\Delta N M$, where ΔN is called the anisotropic form factor. The value of ΔN is positive for an oblate ellipsoid and is negative for a prolate ellipsoid. For a spherical shape, we have $\Delta N = 0$. The resonance frequency ν relates to the applied field H_r by

$$h\nu/g\beta = H_r + \alpha H_a + H_d \quad (72)$$

where α is the factor that depends on the inclined angle between the applied field and the crystal axis. The conditions that constrain this model to nanoparticle system are the non-interaction between particles. Consequently, the anisotropic field is enhanced by two or three orders of magnitudes for nanoparticles. Thermal fluctuations average out the anisotropy field and the demagnetization field is assumed to be zero for spherical nanoparticles.

The FMR spectrum of the sole solvent, cyclohexane, was checked to have a negligible signal while a broad and a

narrow lines have been observed in different concentrations of ferrofluids. The broad line centered at $g \sim 2.22$ with linewidth ~ 750 G is attributed to larger ferromagnetic particles presenting as ferromagnetic resonance. The narrow cusp centered at $g \sim 2$ with linewidth ~ 100 G is due to motional narrowing of ferromagnetic nanoparticles in liquid solvent. As the temperature decreases to 240 K where the fluid is frozen, the narrow cusp disappears adding that the spectrum is not originated from small nanoparticles. The amplitude of the FMR spectra increases with the concentration of ferromagnetic nanoparticles. The unusual narrow line of the densest sample exhibits particle aggregation. The particles become prolate ellipsoids with negative demagnetization fields to slim the FMR linshape.

The FMR spectra for various concentrations of magnetic particles are shown in Figure 49 from which we can evaluate the magnetic susceptibilities at various concentrations. The ATR experiment as shown in Figure 50 provides clues for the dielectric constants of ferrofluids. As we see, $\epsilon_{\text{eff},y}$ and $\epsilon_{\text{eff},x}$ differs slightly while $\epsilon_{\text{eff},z}$ is quite different from each other. This is because the light interacts strongly with the magnetic ellipsoid that aggregate under magnetic field with its main axis in z direction. The $\epsilon_{\text{eff},z}$ can therefore be considered as ϵ_{33} (in Rasa's notation), from which ϵ_3 can be derived by using the effective medium theory as

$$\epsilon_{\text{eff}} = (1 - \phi)\epsilon_m + \frac{\phi\epsilon_m\epsilon_2}{\epsilon_m + n_{x,y,z}(\epsilon_2 - \epsilon_m)} \quad (73)$$

The depolarization factor was determined by different $\epsilon_{\text{eff},z}$ and $\epsilon_{\text{eff},0}$, while the effective dielectric constant, $\epsilon_{\text{eff},x}$ in absence of fields, can be taken as ϵ_{11} . The difference between $\epsilon_{\text{eff},x}$ and $\epsilon_{\text{eff},y}$ can be taken as $i\Gamma$.

Although the expectation value from Rasa's formula is compatible to the experimental result, several remarks should be made. Firstly, the empirical result of Faraday rotation was obtained by fitting which is limited by the resolution of our goniometric system though it is high (0.0005° by implementing a 40:1 gear transformer). Secondly, a slight

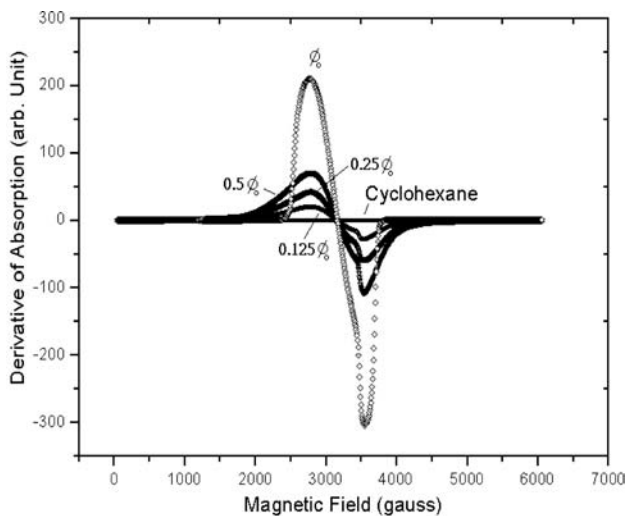


Figure 49. Ferrimagnetic resonance of Fe_3O_4 ferrofluid with different concentrations in terms of ϕ_0 .

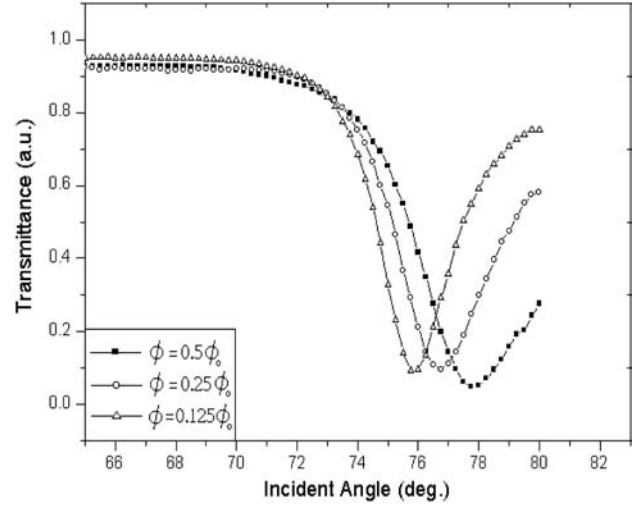


Figure 50. The ATR curve of surface plasma resonance. The position and the depth of the curve determine the real and imaginary part of effective dielectric constant, respectively.

change of the value ϵ_{eff} , a significant deviation of the simulated and experimental Farady angle arises. This impetus us to pursue the dielectric constants to a value of forth decimal points for the real part and third decimal points for the imaginary part, respectively. The accuracy of latter is reduced because of the relatively low reflectance being measured. The error bars shown in Figure 51 were determined by the uncertainty of these values and, as shown, they are proportional to volume fractions.

The ferrofluid of nanometer size appears transparent. The dispersed magnetic nanoparticles evoke to aggregate to form clusters or columns as an external ramp magnet field are applied resulting from achieving the thermal equilibrium state. The spacing of the regular magnetic columns is also controlled by the ramp of the applied field implying a tunable lattice for column arrays with the axis to be parallel to the external field. Column arrays of tunable 2-D photonic crystals with the axis parallel to the magnetic field were observed with column size and space depending on the ramp speed of the applied field. Characterizing with

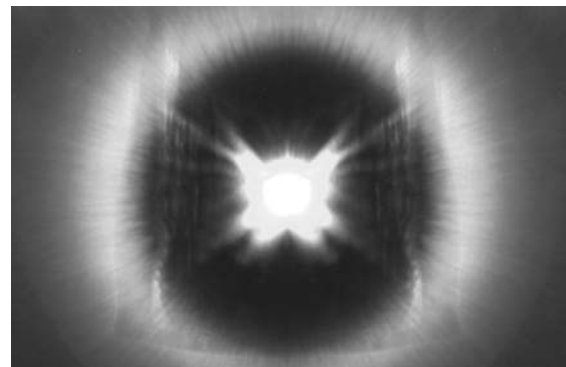


Figure 51. Experimental transmittance pattern with white light incident. The ferrofluid was a kerosene based Fe_3O_4 magnetic nanoparticles with Oleic acid as surfactant. The thickness of the cell was $10 \mu\text{m}$. The ramping rate of the field was 5 Oe/s and fixed at 600 Oe for equilibrium.

various spectroscopic dispersions are elucidated. Experimental transmittance patterns with white light illuminating on a ferrofluid are shown in Figure 51, which clearly reveal diffracted circles [313].

2.6. Nonlinear Optics

2.6.1. Non-Linear Optical Generation

For nanomaterials with particle size or film thickness much smaller than the coherent length, the phase matching condition is usually neglected and the surface nonlinearity makes a manifest contribution due to the enhanced surface to volume ratio. Surface second harmonic generation (SHG) from metals was established on the existence of the nonlinear $E(\nabla E)$ source term that has a large contribution at the boundary due to the discontinuity of the lattice structure and the presence of the bulk magnetic dipole term $E \times \partial H/\partial t$ arising from Lorentz force of electrons. Up to now, many stimulated theoretical and experimental SHG studies of bulk metals are expounded [315–318] that continually to be engaged much attention. Accordingly the theory of SHG from metal surface was built up and modified by the phenomenological parameters (a , b) which, respectively, express the components of current density that are normal and parallel to the surface as proposed by Rudnick and Stern [317]. However, the discussion of azimuthally scanned SHG depending on the interface relation of metal films and the formation of nanoparticles on silicon substrate is still rarely discussed [319].

For metal particles with structure of inversion symmetry, the electric quadrupole field within the selvedge region is the dominant source for the generation of second harmonic light [320–322]. The excitation of surface plasmon (SP), which couples the incident field to propagate along the surface, is thus a main strategy for the enhancement of second harmonic generation. The efficiency of generating surface plasmon depends on the momentum conservation of the electromagnetic waves, which has a rather narrow bandwidth of wave-vectors. The random orientation of the scattered light of the innumerable nanoparticles pursues the phase matching condition. Recently, a significant growth of the intensity of the second harmonic generation (SHG) reflected from metallic island films [323–325] have been reported.

The enhancement of the SHG of small metallic particles can be elucidated by evaluating, quantum mechanically, the quadrupole susceptibility with the exploiting of quantum sphere model [326]. The current source $J(2\omega)$ for the SHG in the α direction is related to the polarization $P(2\omega)$ by

$$J(2\omega) = \frac{\partial P(2\omega)}{\partial t} = -2i\omega P(2\omega) \quad (74)$$

We can write the second harmonic polarization by

$$P_\alpha(2\omega) = \frac{1}{2i\omega} \Delta_{\alpha\beta\gamma\delta} E_\beta^\omega \nabla_\gamma E_\delta^\omega = \chi_{\alpha\beta\gamma\delta}^Q E_\beta^\omega \nabla_\gamma E_\delta^\omega \quad (75)$$

where $\chi_{\alpha\beta\gamma\delta}^Q = (1/(2i\omega))\Delta_{\alpha\beta\gamma\delta}$ is the electric quadrupole, which can be evaluated quantum mechanically. Only the electrons at states near the Fermi energy can contribute to

quadruple transition. A tedious calculation with isotropic average of the polarization directions implies the values of electric quadrupole as given by

$$\begin{aligned} \chi_{\alpha\beta\gamma\delta}^Q = & \left[\frac{16A_{\alpha\beta\gamma\delta} e^3 \hbar E_F^{5/2}}{\sqrt{2}\pi^4 (m)^{1/2} (\hbar\omega)^5} \sum_k^{k_{\max}} \frac{1}{(2k+1)^2} \right] \\ & + \frac{1}{R} \left[\frac{24A_{\alpha\beta\gamma\delta} e^3 \hbar^2 E_F^2}{\pi^3 m (\hbar\omega)^5} \sum_k^{k_{\max}} \frac{1}{(2k+1)} \right] \\ & + \frac{1}{R^2} \left[\frac{16A_{\alpha\beta\gamma\delta} e^3 \hbar^2 E_F^{3/2}}{\pi^3 (m)^{3/2} (\hbar\omega)^5} \dots \right] \end{aligned} \quad (76)$$

where $A_{\alpha\beta\gamma\delta} = P \sum_{nks} \theta_\alpha^{nk} \theta_\beta^{ks} \Omega_\gamma^{sn}$ is the total average value of the angular distribution in the $\alpha\beta\gamma\delta$ tensor components, θ_α^{nk} and Ω_α^{nk} are values of the angular distribution of π^{nk} in the α direction and Q^{nk} in the $\alpha\beta$ direction respectively, and P is the permutation operator of $\alpha\beta\gamma\delta$. The $\chi_{\alpha\beta\gamma\delta}^Q$ contains three terms which are independent, inverse linear dependent, and inverse quadratic dependent on the particle radius, respectively. The second and third terms of above equation clearly adduces the enhancement of the quadrupole susceptibility as the particle size R reduces. The real intensity of SHG should include the local response factor for light traveling in composite materials which implies

$$\frac{d\sigma}{d\Omega} = 2.8 \times 10^{-3} \text{ cm/MW} \quad (77)$$

The calculated SHG intensity dependence on the Ag particle radius R is depicted in Figure 52 that is consistent with the experimental results of Aktsipetrov et al. [327]. The experiment of gold nanoparticles by ion implantation in glass showing that the third-order optical susceptibility was proportional to the fourth power of the radius of the colloid

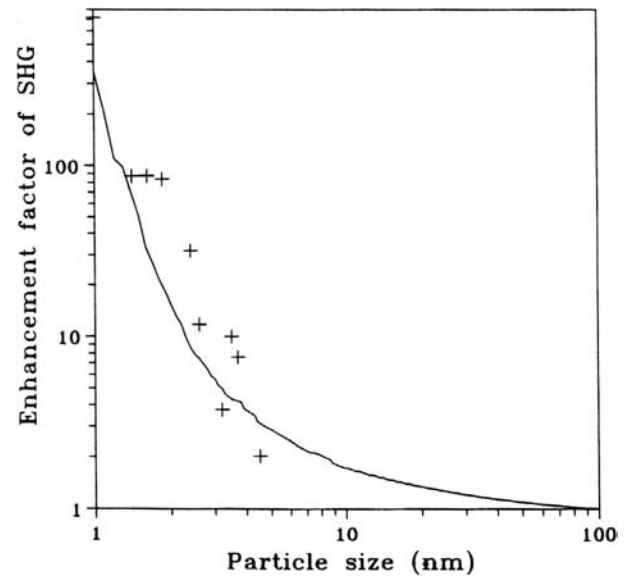


Figure 52. The theoretical work (solid line) and experimental data (crossed mark) of the ratio of enhanced SHG to the bulk value at various sizes of silver nanoparticles. Reprinted with permission from [326], K. Y. Lo and J. T. Lue, *Phys. Rev. B* 51, 2467 (1995). © 2005, APS.

particles [327] was not justified. For experiments performed in high vacuum, the SH intensity was found to decrease about three folds for oxygen exposure on the cleavage surface [328] and the anisotropic SH polarization disappears. The quantum mechanic two-band model [329] and the non-local response function [330] can properly provide a good description. We have also attempted to solve the isotropic system by the surface scattering of conduction electrons, which is more germane to follow classical size effect regime.

Surface second harmonic generation can be exploited as a very sensitive method to diagnostic the surface strain induced on semiconductors by a deposition of films. we found that the threefold symmetric SH patterns of Si(111) are distorted by deposition of silver films. The nonlinear surface polarization inherited by the Ag/Si interface is enhanced for the deposition of an ultra thin layer of silver films resulting in the distinguishable three lobes of the SH pattern. The same results are found for the Ag/Si surfaces distributed with silver nanoparticles, while the three-fold pattern remains even the particle size increases to percolated islands. A strain layer existing in the interface induces additional anharmonic oscillation strength along a special crystal orientation, which results in an asymmetric pattern for the surface scan of SH intensity. Considering the small response of the s-polarized SHG for isotropic silver metal, the three-fold symmetric lobe is very prominent for granular silver films on a Si(111) surface. The symmetric surface SHG pattern induced by lattice-misfit strain can be illustrated by imposing an external force on a bare Si surface. The sensitive ψ -scan of surface SHG provides a clue to detecting the interface strain existing in multilayered films that cannot be elucidated by other surface analysis methods.

As far as the SH field of centrosymmetric material such as Si(111) substrate is concerned, the bulk contribution of electric dipoles is zero, and the lowest order nonlinear polarization density is embodied in bulk magnetic dipoles and electric quadrupoles. The surface contribution comes from the underneath term within the Thomas-Fermi screen length arising from the breaking of the lattice periodicity and the existence of dangling bonds caused by desorbed molecules. Sipe et al. [331] and Heinz et al. [332] have discussed the phenomenology of bulk and interface SHG from cubic centro-symmetric crystals in detail, which was verified by experiment. Concerning the dominated contributions of SH intensity on metal surfaces, three nonlinear sources originate from (1) the bulk current within the penetration depth embodied in magnetic dipoles and quadrupoles, and (2) two surface current sources within the selvedge region which are, respectively, parallel and normal to the metal-vacuum interface. When a thin silver film is deposited on silicon substrates, an additional SH field arises from the anharmonic oscillation induced by the strain existing in the interlayer. Consequently the symmetric pattern of the azimuthal SH intensity, contributed to by the zincblende silicon surface, will be distorted by the non-uniform interface strain.

For metallic films, the SH waves are essentially generated from the electric quadrupole of the bulk and dipole sheets within the selvedge region. The nonlinear optical reflectivity of SiO₂/Ag/SiO₂/Ag/SiO₂ multilayer structure was evaluated to characterize the interface structures [333, 334]. Later, we employed the hydrodynamic theory and observed the

dependence of incident-angles on the SHG intensity at various thicknesses of silver films deposited on glass substrates [335]. Also, the interface strains inherited by the molecular-beam-epitaxially (MBE) grown III-V compound films on silicon substrates were diagnosed by analyzing the ψ -scan of surface SHG patterns [336].

In this work we measured the surface ψ -scan of the SHG pattern for thin silver films and nanoparticles on Si(111) substrates. The Ag nanoparticles were obtained by rapid thermal annealing of a thin Ag film coated Si substrates. The particle sizes are strongly related to the thickness of deposited thin films. The nonlinear optical susceptibility is attributed to polycrystalline Ag nanoparticles in ellipsoidal shapes [337]. For an Ag/Si system with a film thickness less than the penetration depth, the SH nonlinear susceptibility is due to many factors such as the difference in normal polarizations between the top and bottom sides, the electron-plasmon oscillation, the field enhancement due to non-spherical shape, and the possible dipole field arising from the breaking of inversion symmetry induced by interface-strain [338]. A weaker SH intensity of the annealed Ag/Si film than that of the virgin film results from the small filling factor of the aggregated nanoparticles and their spherical shape. The non-uniform interface strain relaxes during the thermal annealing process resulting in the 3 m-symmetry behavior of the condensed nanoparticles. In addition, we introduced the SH intensity patterns of an artificially imposed force on Si(111) substrates to adduce the evidence of the asymmetric distribution of surface SHG induced by interlayer strain.

For centro-symmetric media such as silicon substrates, the remnant electric dipoles that contribute to the SHG are the surface terms within a selvedge region of several angstroms such as

$$P_{iS}^{2\omega} = \chi_{S,ijk}^{(2)} : E_j(\omega)E_k(\omega) \quad (78)$$

where $\chi_{S,ijk}^{(2)}$ is the second-order susceptibility tensor relevant to the surface symmetry structure and electric polarization of the surface layer arising from dangling bonds and adsorbed molecule. Below the selvedge region, but within the penetration depth, the bulk terms receive contributions from electric quadruples and magnetic dipoles that yield the i -th component of the nonlinear bulk polarization as given, respectively, by [339]

$$\begin{aligned} P_{b,i}^{2\omega} &= \gamma \nabla_i (\vec{E} \cdot \vec{E}) + s (\vec{E} \times \vec{\nabla} \times \vec{E})_i \\ &= \gamma \nabla_i (\vec{E} \cdot E) + s \frac{j\omega}{c} (\vec{E} \times \vec{H})_i \end{aligned} \quad (79)$$

where γ and s are non-zero isotropic and anisotropic parameters, respectively. The first term represents a gradient vector that is independent of the orientation of principal crystallographic axes, and the second term shows an anisotropic contribution relating to the crystal symmetry depending on the azimuthal angle φ . For either the p- or s-polarized fundamental radiation, the phenomenological theory given by Sipe et al. [340] delineates the variation of the SH field on azimuthal angles for the Si(111) crystal

surface with $3m$ symmetry as given by

$$E_p^{2\omega} = a_p(\theta) + c_p \cos(3\varphi) \quad (80)$$

$$E_s^{2\omega} = b_s \sin(3\varphi) \quad (81)$$

where a_p , b_s , and c_p are linear combinations of the surface and bulk nonlinear susceptibilities including the combination of isotropic constant γ and the non-vanished susceptibility tensor elements. For the coefficient $a_p = 0$, which is a function of the incident angle θ , the generated scan of the surface SH is a symmetric six-fold pattern and for $a_p \neq 0$, an asymmetric six-fold lobe is observed. For a thin silver film deposited on a Si(111) substrate, the total SH field originates separately from the above described magnetic dipole and electric quadrupole terms of the thin silver film, and the interface-strain induced nonlinear polarization.

Elastic strain is evoked near the interface resulting due to a misfit of the lattice constant of the film with the substrate. This asymmetric distribution of the second-order nonlinear optical susceptibility induced by the strained layers has also been found in other systems [339, 341]. The misfit factor can be expressed as $f = (a_f \cdot a_s)/a_s$, where a_s and a_f are the lattice constants of the substrate and film, respectively. In Eq. (2), the interface strain not only contributes to the extra nonlinear polarization to the isotropic term γ but also enhances the anisotropic term ζ due to the increased thickness of silver films [342]. Goverkov [343] expressed the azimuthally angular dependence on the p-polarized SHG for a p-wave incident beam by

$$I_{p-p} \sim [\chi_{xxx}^{(2)IH} \cos 3\varphi + \delta]^2 \quad (82)$$

where $\chi_{xxx}^{(2)IH}$ means the inhomogeneous strain induced contribution to the nonlinear optics (NLO) susceptibility, and δ is a linear combination of the $\chi_{ijk}^{(2)IH}$ elements. Accordingly, the isotropic and an-isotropic terms in eq. (82) increase with the inhomogeneous strain. In Ref. [339], the non-vanished elements of the second-order NLO susceptibility of the Si(111) strained lattice have been demonstrated. In addition, the surfaces of thin metal film excited by external irradiation can generate the second-order nonlinear optical response that consists of a “surface” current density penetrating only a few Thomas-Fermi screening lengths below the metal surface (the so-called selvedge region) and a “volume” current density that extends over the skin-depth. Theoretically, the “bulk” contribution depends on the thickness of the film, as the thickness is less than the skin depth. The “surface” contribution is less affected by the film thickness. In principle, the two parts of SH contributions are based on a free-electron gas or hydrodynamic model so that we can speculate that the SHG depending on the azimuth-angle yields the isotropic term γ .

We tacitly assumed that the crystalline structure of silver nanoparticles is the same as that of the original metal film. In our previous work [344] we had predicted that the magnitude of the quadrupole susceptibility is inversely proportional to the particle size attributed to the quantum size effect as the particle size diminishes smaller than 10 nm. Aussenegg et al. [341] published a practical consideration of SHG arising from nanoparticles by assuming that a simple model of a real island film is a collection of rotational ellipsoids resting on the substrate with their long axis parallel

to the surface. On account of the shape and size effect, different polarized input beams can excite different intensities of SH light. Considering that the s-polarized incident field is unable to drive the surface electron-plasmon oscillations, only the “bulk” contribution needs to be concerned. This is because the surface dipole susceptibility for each dipole is compensated by its opposite dipole when illuminated by a uniform light. However the field for the p-polarized input beam can be divided into parallel and normal components to the substrate surface. The normal component not only drives the electron-plasmon oscillation along the short axis of the oblate ellipsoid, it also excites surface dipole susceptibilities arising from the top and bottom interfaces of silver particles. All of these SH fields measured in the ψ -scan imply an isotropic distribution except the contribution from interface strain which yields asymmetric pattern.

To elucidate the strain induced nonlinear second-order susceptibility, we draw a schematic diagram of the interface between the thin silver films with cubic symmetry on a thick cubic silicon substrate, which is located in the xy plane with the z -axis perpendicular to the interface as shown in in Figure 53. The strain tensor in the film can be expressed as [342]

$$U_{lm}(r) = U_{lm,mis}(r)\theta(h_c - z) + U_{lm,disl}(r)\theta(z - h_c) \quad (83)$$

where $\theta(z - h_c)$ is a step function with h_c being the critical thickness of the film for the demarcation of a pure lattice misfit and a mixture of the dislocation misfit. The strain tensor induced by the lattice misfit is written as

$$U_{lm,mis}(r) = f\delta_{lm} \quad (84)$$

where $f = (a_f - a_s)/a_s$ with a_f and a_s being the lattice constants of the film and the substrate, respectively, and δ_{lm}

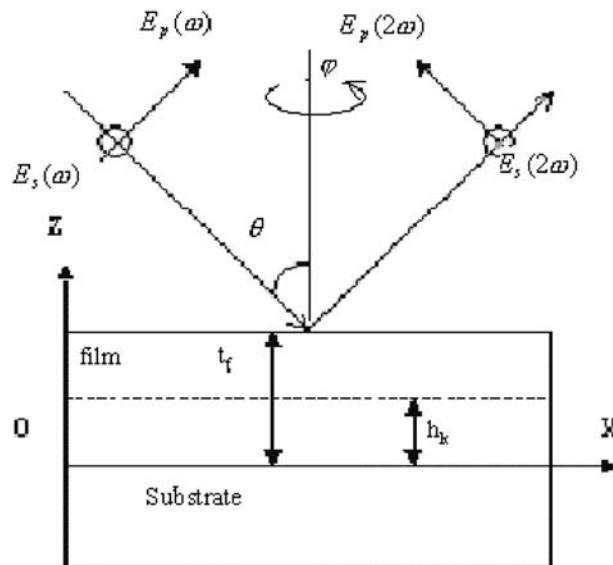


Figure 53. A schematic diagram of the interface between the thin silver film, with cubic symmetry, and a thick cubic silicon substrate that is located in the xy plane with the z -axis perpendicular to the interface. Reprinted with permission from [345], C. S. Chen and J. T. Lue, *European Phys. J. B* 46, 367 (2005). © 2005, EDP Sciences.

being the Kronecker delta function with $l, m = x, y$. For a deposited silver film, with thickness, d_f , much smaller than the critical thickness h_c , we can neglect the strain induced by the misfit of dislocation, wherein the second-order nonlinear susceptibility can be expressed totally as

$$\chi_{ijk}^{(2)}(r) = \chi_{ijk}^{(2,0)}(r) + p_{ijklm} U_{lm}(r) \quad (85)$$

where $\chi_{ijk}^{(2,0)}(r)$ is the original value of the free surface, and p_{ijklm} is a nonlinear photoelastic tensor. For both s- and p-polarized input light, the second-harmonic radiation will be p-polarized.

Thin silver films were deposited on Si(111) substrates in a high vacuum chamber by thermal deposition. The film thickness was monitored *in situ* by a quartz oscillator with the frequency-shift versus thickness calibrated by an α -stepper. The experimental set-up for the SHG measurement is illustrated in our previous work [336]. The source of the fundamental radiation for the SH generation measurement is a passively mode-locked, Q-switched Nd:YAG laser (wavelength at 1064 nm) with a typical FWHM of 100 ps at a Q-switch repeating rate of 1 KHz. Due to the extremely narrow pulse width, the single pulse energy can be reduced to as low as 0.5 mJ to immunize from thermal radiation. The fundamental laser beam passing through a glass beam-splitter, which reflects 5% of the laser intensity on an AT-cut quartz plate, is employed as a reference SHG signal. The straight light beam on passing through a Schott glass filter illuminates the sample surface which is mounted on a computer-controlled step-motor with a focused beam spot size of 1~2 mm². Firstly, the light reflected from the sample surface passes through a set of blocking filters, which only allows the SH wave to pass through. As depicted in Figure 53, the incident angle θ was kept at 45° during the azimuthally angular rotation (or φ -scan). A computer controlled stepping motor provides an automatic scanning of the ψ angles for the sample surface orientation in every step of 0.9°. The rotation axis for the φ -scan is checked to be parallel to the incident beam as verified by observing the fixed output spot whilst rotating the silicon wafer. The precision of the orientation of the polarizer is $\pm 0.5^\circ$.

After measuring the SHG of the silver film coated silicon wafers [345], the same samples were subjected to a rapid thermal annealing at 150 °C for ten minutes. Because the surface tension of Ag grains is greater than the cohesive force of Ag/Si interface, the silver film tends to aggregate to form nanoparticles as displayed in Figure 54, which were examined by a scanning electron microscope (SEM). The particle size crucially depends on the film thickness, the evaporation conditions, and the annealing temperature and duration.

To certify that the rotation axis of the ψ -scan is parallel to the incident beam, the p- and s-polarized SH fields with the fundamental p-polarized input beam for the ψ -scan on a clean Si(111) substrate were first measured. The symmetry distribution of the sixfold pattern verifies this evidence. The SHG for various thicknesses of Ag films on Si(111) substrates for the p-input and p-output are shown in Figure 55(a). In all of following Figures, the intensity scales are incongruent. The reduction to three-lobe distribution of the p-in and p-out occurs for the ultra-thin silver

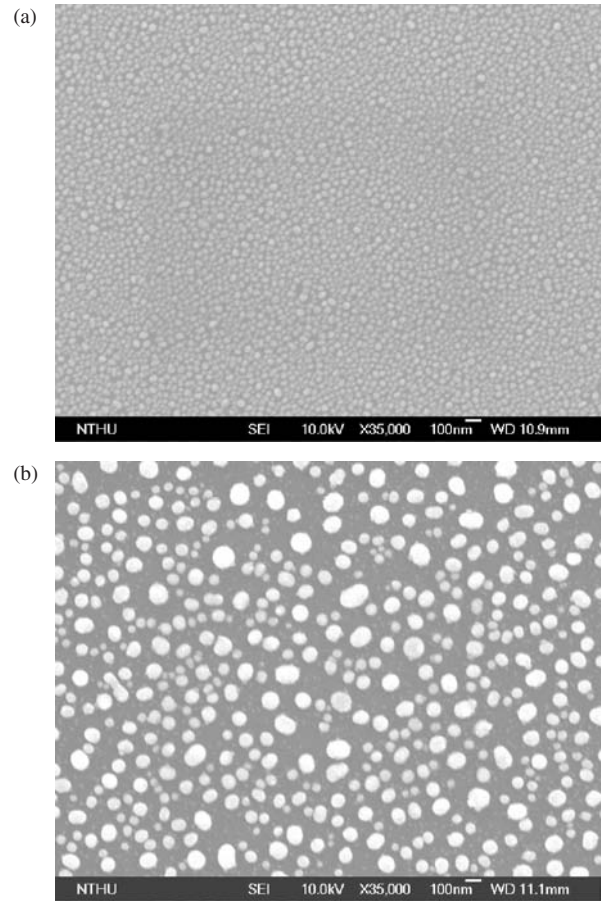


Figure 54. SEM pictures of silver nanoparticles formed through a rapid thermal annealing at 150C for ten minutes of thin Ag films of thicknesses (a) 24 nmA, and (b) 45 nm, respectively. Reprinted with permission from [345], C. S. Chen and J. T. Lue, *European Phys. J. B* 46, 367 (2005). © 2005, EDP Sciences.

film (~5.0 nm) even the isotropic second-order nonlinear susceptibility of silver is ten times larger than that of silicon suggesting that the non-linear susceptibility due to the interface contribution inherited by the silicon substrates is enhanced by depositing silver films. The isotropic contribution of second-order nonlinear optical response for silver films progressively increases to overwhelm the anisotropic surface terms of silicon as the thickness of the silver film increases.

Eventually, the thin silver film not only provides the isotropic contribution, but also introduces a strain at the Ag/Si(111) interface to generate an extra non-linear susceptibility to its original anisotropic susceptibility. Furthermore, increasing the silver-film thickness within the skin depth increases the isotropic term contributed from silver resulting in a homogeneous spherical SH pattern. The lattice misfit at the interface Ag/Si(111) causes a strain that induces a strong interface dipole, which distorts the symmetric patterns of the SHG by the surface ψ -scan. Meanwhile the anisotropic coefficients increase with the film thickness. As the film thickness increases to 9.7 nm which is larger than the optical penetration depth of silver, the isotropic term attributed to the deposited silver is greater than that of the

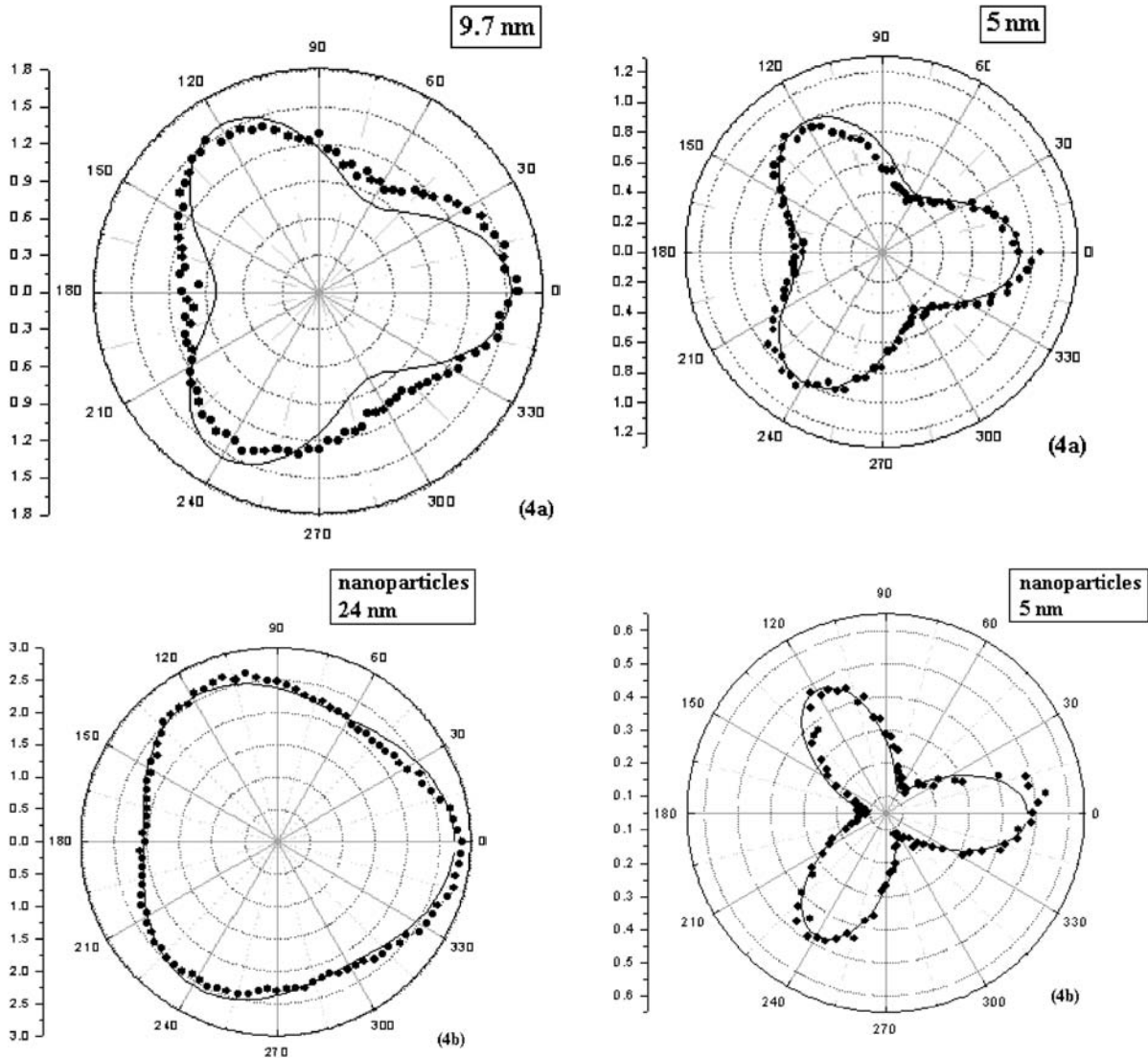


Figure 55. The ψ -scan of the p-polarized input and the SH p-polarized output for (a) various thicknesses of silver films on Si(111) substrates, and (b) various particle sizes of the nanoparticles formed by the annealing of above films.

anisotropic term arising from the interface strain of silicon surface, which results in a uniform distribution of the surface SHG by the ψ -scan.

For comparison, the ψ -scanned SHG for Ag nanoparticles aggregated from the annealed silver films are shown in Figure 55(b). For ultra-thin nanoparticles (<5.0 nm), the surface scan illustrates a much distinguished three-fold symmetry resulting from the enhanced non-linear anisotropic polarization induced by the Ag/Si strain below the silver islands. As the film thickness increases further the isotropic susceptibility of silver overwhelms the anisotropic terms of Si and the ψ -scanned SHG becomes uniformly distributed. It needs to be mentioned that nanoparticles aggregated from rapid thermal annealing (RTA) of thin silver films enhance the anisotropic surface non-linear susceptibility of Si to form a distinguished 3 m symmetry of Si(111). The particle size is closely related to the original film thickness which is not in accord with the size dependence on the SH intensity as portrayed in Refs. [344, 345]. Since the thickness of an ultra thin

metal film is much less than the penetration length, the total effective volume will overcome the value of quadrupole susceptibility which is inversely proportional to the nanoparticle size.

However, the non-symmetric behavior, because of strain induced nonlinear polarization imposes an excess contribution $g_s + P_s \sin(\psi)$ to the ψ -scan of the SH field pattern. The parameter g_s is a constant, which represents the isotropic contribution from the interface strain. In fact, the ψ -scan of p-polarized SH field patterns also have a superposition factor $g_p + P_p \cos(\psi)$ on them. For simplification, we incorporate this into the factor a_p . The coefficient $P_{s(p)}$ is the strain-induced, non-symmetric constant intrigued from the s(p)-polarized SHG. The angle ψ is defined as $\psi - \psi_0$, where ψ_0 depends on the strain orientation. The parameter $P_{s(p)}$, dependent on the film quality and thickness, represents the degree of non-uniform inhomogeneous strain. The presence of this factor will curtail the isotropic and anisotropic contributions from the crystal structure and

interface. The threefold asymmetric pattern for the condensed island films becomes more prominent than that of the virgin films plausibly arising from the crystalline alignment of silver islands at the interface with the 3 m symmetry of Si(111) substrates. The RTA method relaxes the nonuniform inhomogeneous strain.

The bending direction parallel to the primary-edge flat-cut of the *p*-type Si(111) wafer was defined as the initial zero angle. The six fold SHG patterns are largely distorted for both the *p*- and *s*-polarized SH responses as shown in Figure 53, which also reveals that the distortion increases with the point press. The alternation from six fold pattern to asymmetric two fold is clearly manifested for the *s*-polarized SH due to its independence of on the surface isotropic contribution a_p . The wafer was then rotated every thirty-degrees and we then measured the ψ -scanned SH intensity with three kinds of pressure imposed by the screw. To confirm the SH intensity was closely related to the azimuthal angle ψ , the incident angle θ was precisely calibrated. The SH intensity was measured with the fundamental input beam impinging on the bending direction.

In this experiment, we observed that the SH intensity decreases with the increase of the imposed force by the screw, implying a loss of phase coherence in the SH fields generated by the strained layers. The asymmetric SH pattern appears as the strain increases. Sophisticatedly, the anharmonic oscillating strength arising from the bulk covalent bonds changes with the bending of the wafer. This force-induced strain has a different effect on the SHG in comparison to that generated from the lattice misfit of interface layers because the latter induces interface dipoles providing excess SH contribution without destroying the bulk crystalline structure. However, the non-uniform stress provides an evidence of a strain induced asymmetric SH field distribution for the surface ψ -scan of the SHG pattern for thin silver films and nanoparticles on Si(111) substrates.

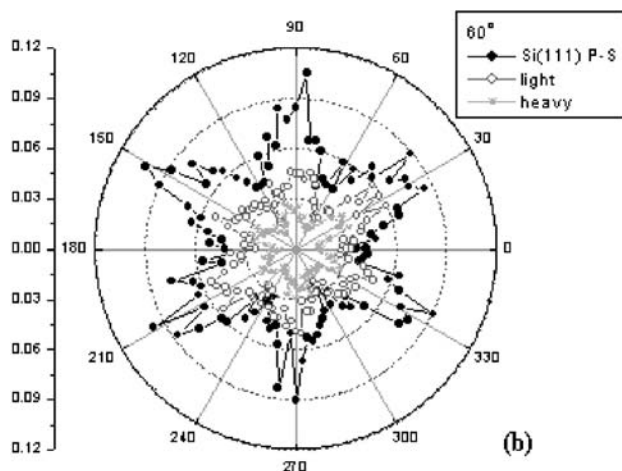


Figure 56. The *p*-wave input and *s*-wave output SHG for Si(111) with various imposed forces and incident azimuthal angles Figure 54 SEM pictures of silver nanoparticles formed through a rapid thermal annealing at 150C for ten minutes of thin Ag films of thicknesses (a) 24 nmA, and (b) 45 nm, respectively. Reprinted with permission from [345], C. S. Chen and J. T. Lue, *European Phys. J. B* 46, 367 (2005). © 2005, EDP Sciences.

The stress induced strain can be either isotropic or anisotropic along different directions depending on the uniformity of modulus along various directions, therefore affecting the symmetric or asymmetric distributions of the SHG loops during the ϕ -scan. However, the SH intensity will be largely affected by the surface strain. Increasing the incident light too high might changing the surface composition to be nonuniform implying an asymmetric distribution of the SHG patterns.

3. NANODEVICES

3.1. Silicon Single-electron Transistors and Electron

To reduce the size of current devices beyond the limit of hundred nm, the metal single electron transistor (SET), using the Coulomb blocket effect, has been promptly developed. The scaling of such devices down to atomic scaling is expected to replace the customary semiconductor logic or analog devices. Due to the narrowing of the distance to several nanometers between isolated gate from the drain and source, tunneling current surmounts the conventional conduction currents readily. The tunneling of a single electron to the nanosized gate can build a high potential drop on account of the extremely smallness of the capacitance of the gate. There are several constraints that limit the size of SET arising from the physical principles and device structure. Accordingly, thermodynamic principle requires the on-off threshold energy $E = 0.5C/V^2$, where C is the gate capacitance and V is the gate-control voltage, must be larger than the thermal energy $(\ln 2)kT$, and the uncertainty principle limits the switching time $\tau_d = L_{ch}/v_s$, where L_{ch} is channel width and v_s is the saturation velocity, to be smaller than E/\hbar . Many excellent reviews on SET [346–349] were reported. In electron-beam lithography, the well-known proximity effect refers to variation in the width of patterned lines with the density of other shapes nearby, which variation of course makes increasing the resolution difficult. The electron proximity effect has been a major obstacle to achieving fine resolution in electron beam lithography. The distribution of intensity of exposure has a Gaussian intensity profile, because electrons are forward scattered and back scattered. The main method to compensate for the proximity effects are to adjust the dosage of electron beams according to the density of the patterns, or to anticipate the changes in dimensions of the features and make compensating adjustments in advance. Nevertheless, this work reports the fabrication of single electron transistors (SETs), made by exposing different shapes in the pattern to incident electrons with various intensities. Figure 57 schematically depicts the mechanism used in this work for forming nano structures [350].

The nano-constriction between the quantum dot of the Si-SET and the source (or drain) electrode was formed by overlapping the distribution of the electron dosages of two separately written nano-dots on a silicon oxide insulating (SOI) wafer. By adjusting the exposure conditions, we can make the width of the nano-constriction smaller compared with the diameter of the quantum dot, thus the nano-constriction can form the barrier of the electron transport

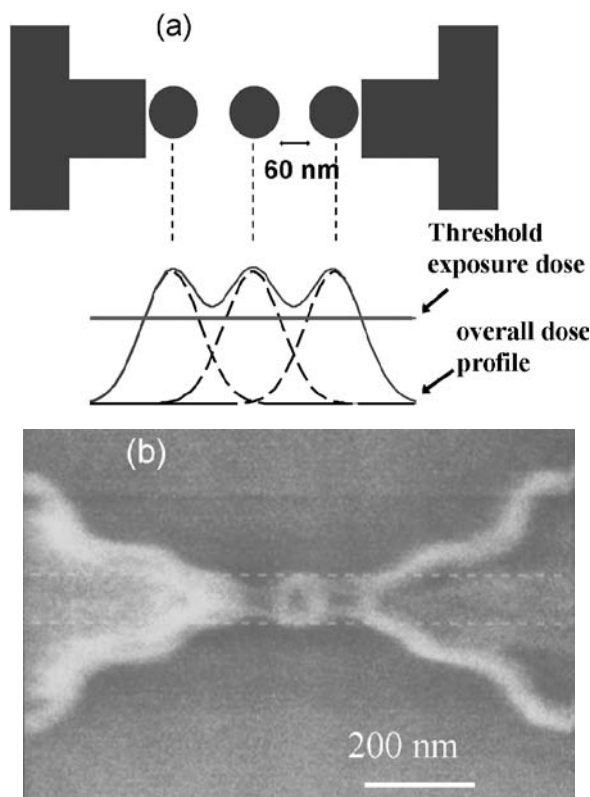


Figure 57. (a) Schematics of the mechanism of SET fabrication. The overlap of the dosage profile, with excess dosage above the threshold exposure dose will form a narrow exposed region between the two dots written with e-beam writer. The SEM image of the developed pattern is shown in (b). Reprinted with permission from [349], S. F. Hu et al., *Appl. Phys. Lett.* 85, 3893 (2004). © 2004, American Institute of Physics.

required for SET operation [346]. Our method of producing Si-SET is very flexible, increasing the number of circles between the two electrodes, can be applied to make complicated nano-devices with multiple quantum dots. For one-dot device, the device shows typical MOSFET $I-V$ characteristics at room temperature [347, 348]. At low temperature, I_D exhibits series of peaks when V_{CG} is varied (Fig. 58).

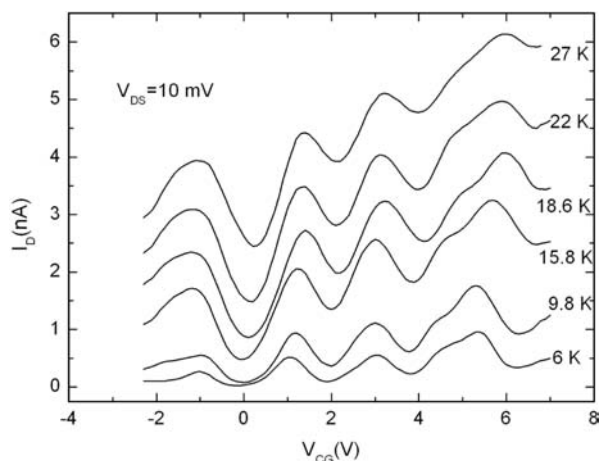


Figure 58. I_D-V_{CG} measurements at different temperatures. The V_{DS} is kept at 10 mV during the measurements.

Moreover, bi-directional pump current as well as single electrons transport is observed in a silicon dual-gate bi-directional electron pumps. Quantized current was observed in a silicone dual-gate bi-directional electron pump. The polarity of the pump current can be altered either by the dc voltages applied on the two gate electrodes, or by the phase difference of the ac modulations added to the gate voltages (Fig. 59). The pump current exhibits stepwise jumps as the amplitude of the ac modulation is increased, and the step height of the current jump is quantized in unit of ef , where f is the frequency of the ac modulation [349].

3.2. Surface Modification by Electric Discharge with Electrodes Implemented with Carbon Nanotubes

We demonstrate a promising nanofabrication method to fabricate a fine pattern, by employing multi-wall carbon nanotubes (MWCNT). The MWCNTs were grown on a tungsten tip by the hot-filament chemical-vapor-deposition method (see Fig. 60) as the miniature electrodes to oxidize silicon nitride with advantages of long-life, are arranged to arbitrary arrays by computer controlling of a 3D step motor on which the tungsten tip is loaded as shown in Figure 61. A study of surface plasmon polariton (Σ SPP) resonance enhancement using Kretschmann configuration to detect the dielectric properties of the 2D photonic crystal is illustrated.

The inheriting of a high aspect ratio of carbon nanotubes (CNTs) leads to a large electric field enhancement for electron emission at low applied electric fields. Recently, it is largely demanded to develop a precise micro-electric discharge machining (EDM) process to produce wire electrodes as tiny as $2 \mu\text{m}$ in diameter [351–353] by using etching or wire electric discharge guiding (WEDG) method to

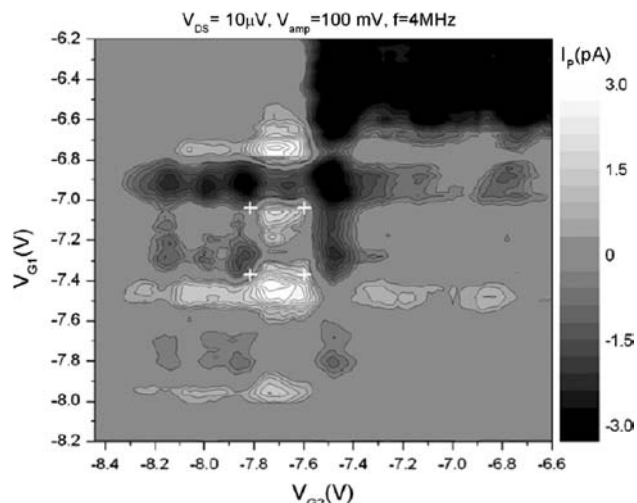


Figure 59. Contour plot of the pump current I_P as a function of V_{G1} and V_{G2} with 4 MHz at $V_{DS} = 10 \mu\text{V}$. White marks are the positions of the current peaks, which is the DC result without AC signal applied. The polarity of the pump current is changed at different V_{G1} and V_{G2} . Reprinted with permission from [350], Y. C. Chou et al., *Appl. Phys. Lett.* (2005/06), submitted. © American Institute of Physics.

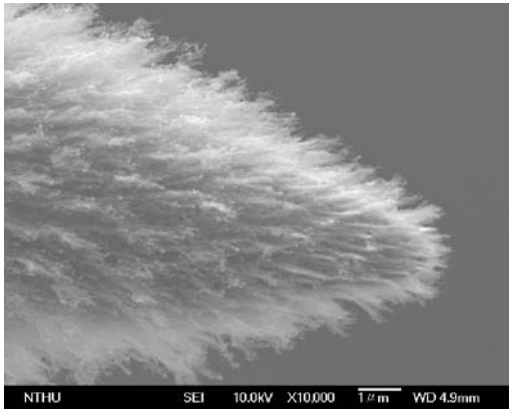


Figure 60. The SEM picture of MWCNTs grown on a tungsten tip, which was sharpened by etching a tungsten filament in a 1 M KOH solution. The tip was catalyzed with nickel film by electrolytic plating.

control the precision of work-pieces. On taking the advantages of the straight up-right, durability and strong electron field emission, The multi-wall carbon tubes grown on copper based alloys can replace the micro sized electrodes for surface modification.

The circuit for performing the micro-EDM is shown in Figure 62 where the integrated circuit SG3524 produces the controlling square clocks which are amplified by the high voltage transistor IRF640 to control the switching voltage for embarking the discharge electrodes D6 to start or close. The photo coupler TLP250 isolates the controlling gate from the power output to immunize the noise feedback. Variable resistance R7 controls the demanded current during EDM.

The surface modifications of the *n*-type Si substrate [354] before and after the electric discharge machining (EDM) under a pressure of 10^{-3} torr are shown in Figures 63(a) and 63(b) respectively. A nano-scaled EDM polishing process for 20 minutes clearly shows the improvement of the surface roughness to be about 600 nm. The surface-eliminating rate is 30 nm/min for implementing the MWCNTs cathode in the nano-scale EDM polishing process. SEM micrograph as shown in Figure 63(b) clearly reveals a burned trace of diameter 120 nm corresponding to the size of MWCN tubes. The highlight on the surface [355] of the MWCNTs cathode after several EDM processes is expressed in Figure 64. Due to the non-perfect flatness of the electrode surface, the

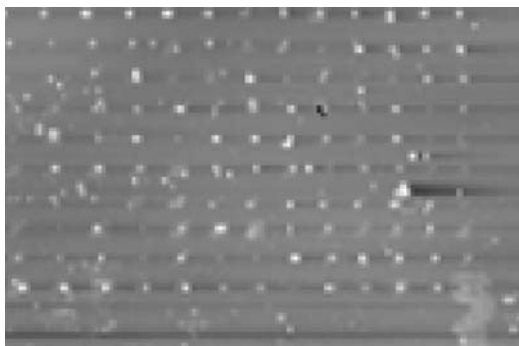


Figure 61. SiO₂-dot arrays performed by a computer controlled selective-area oxidization of silicon-nitrides films grown on Si wafers.

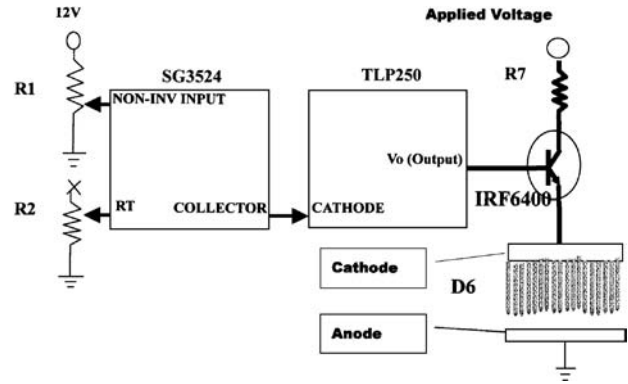


Figure 62. The schematic diagram of the electronic circuit to perform the micro-EDM process that generates the desired on and off cycles.

discharge chance of each nanotube at repeatedly EDM process is not equal.

The outlooks of the MWCNTs with the discharge gap filled with air at high voltages are shown in Figure 65. Increasing the applied voltage, the carbon tubes are twisted

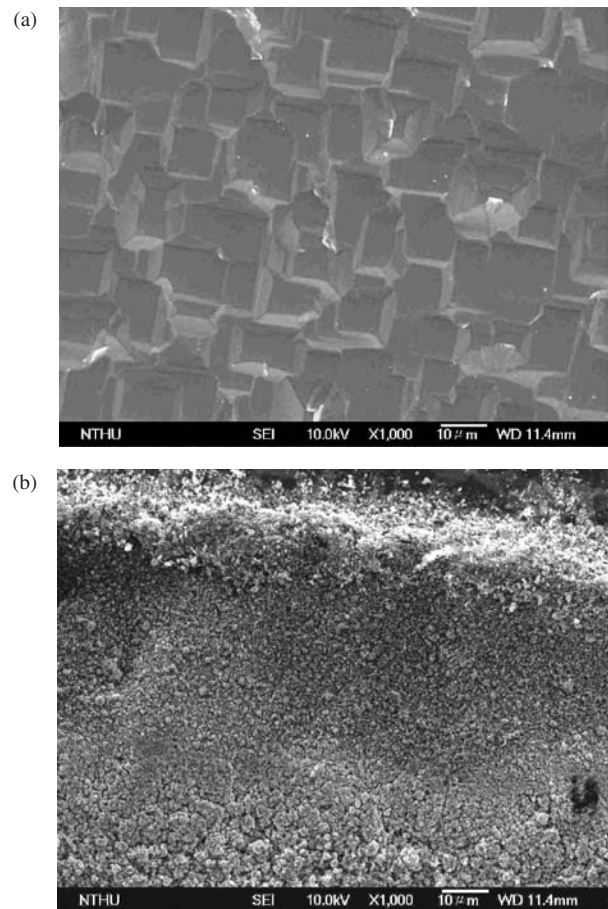


Figure 63. The surface modifications of the *n*-type Si substrate (a) before and (b) after the electric discharge machining (EDM) under a pressure of 10^{-3} torr, respectively. Reprinted with permission from [355], H. Y. Miao et al., *J. Nanosci. Nanotechnol.* 6, (2006). © 2006, American Scientific Publishers.

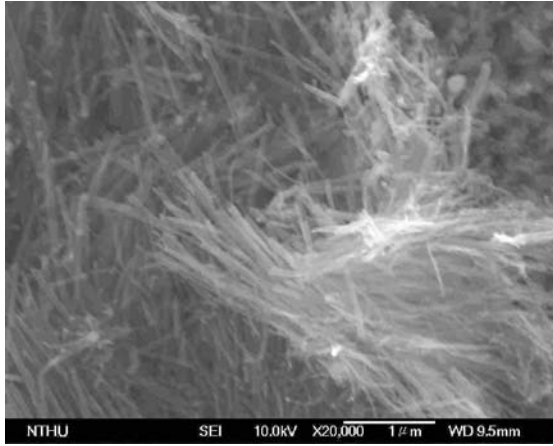


Figure 64. The SEM photographs for the highlight of the MWCNTs cathode after nano-scale EDM processes.

by the airflow generated by the explosion of arc discharge. The CNTs even twisted and conjunct together at the tips by the whirlpool of the water stream for the electrodes embedded in de-ionized water.

3.3. Nanolithograph and Nanothickness Measurement

The processing technology of nano energy beam lithography is generally implemented by means of exposure methods such as electron beam, ion beam, and laser beam etching on thin film for micro circuit manufacturing. The minimum line width less than 100 nm can be achieved by these technologies. As the demand for high resolution electron (or optic) beam lithography capacity continually grows, nano fabrication technologies are being driven to obtain higher device densities. The spatial resolution of conventional optical microscopy is restricted by the diffraction limit of a focused spot in far-field optics. No optical image with the fine structure beyond the diffraction limit can be acquired.

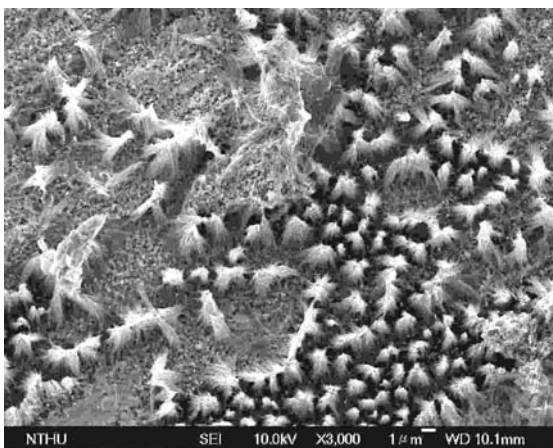


Figure 65. The erosion of the MWCNT cathode after the EDM process with the gap embedded in air discharged at high voltages. Reprinted with permission from [355], H. Y. Miao et al., *J. Nanosci. Nanotechnol.* 6, (2006). © 2006, American Scientific Publishers.

Recently, the development of near field scanning optical microscopy (NSOM) provides a new path to obtain high spatial resolution optical images without diffraction limited. Because they produce small spot size, near-field optical techniques using evanescent light are being developed to overcome the diffraction limit of far-field optics and have been applied to Nano fabrication. In this case, small aperture, scattering points or solid immersion lens (SIL) have been used to record or retrieve small marks beyond the diffraction limit [355–362].

A new nano energy beam lithography exploiting near field optical fiber probe are developed, which has been demonstrated to create components at 0.03 microns (or 30 nm), compared to present 0.18 micron by optical lithography. It can be scaling down to 100 or 50 nm readily. The fabrication of nano probe [363] is capable of producing nano energy beam with near field optical fiber probe, which adopts both the advantages of high transmission efficiency with no absorption of the dielectric tip and local enhancement of the metallic coating (the tip coated with a metallic thin film which could be used to produce spots smaller than those generated with the dielectric tip) to design a new type of tip. The illustrated type of the improved tip is a metal tip that combines with a local dielectric tip, as shown in Figure 66. In the process of coating the metal tip with aluminum thin film (by vacuum evaporation), the tip apex was exposed to the fabricated local noncoated dielectric tip. That is, the tip bases on the metal-coated tip and extends the internal dielectric material outside the metal-coated tip. The diameter of the tip apex is 50 nm and the length of the noncoated part is 25 nm. A hollow tip apex with a radius of 25 nm forms a semispherical lens surface. Figures 67(a) and 67(b) show the calculated results in the x - z and y - z sectional planes by p-polarization illumination; in particular, The light emerges from the top of the metal-coated part into the dielectric medium of tip apex end. It is expected that the optical transmission will be enhanced at the interface between the coated and noncoated parts of the tip apex. The field-enhanced effect is due to the dipole polarization on the metal aperture rim and the beam blocking by the metal layer (coated part). The high transmission effect at the top of the tip apex is due to the effect of the nonabsorptive properties of the dielectric medium (noncoated part). Because of the use of both metal-coated and noncoated parts, the

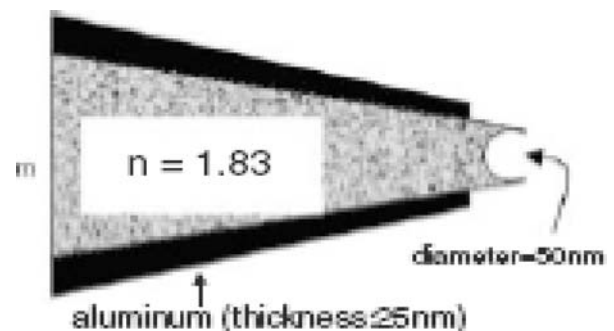


Figure 66. Sectional plane diagram of 3D improved tips: the metal-coated tip com Figure 66 Sectional plane diagram of 3D improved tips: the metal-coated tip combines with the dielectric tip that a hollow tip apex forms a semispherical lens surface.

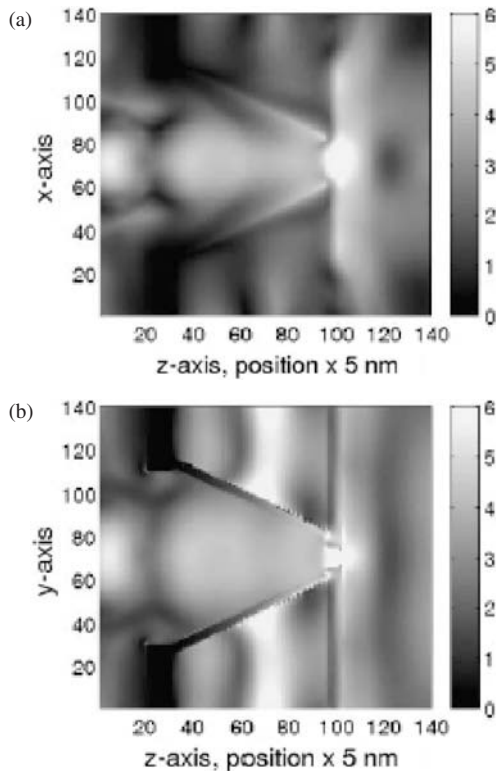


Figure 67. Distribution of the electric field intensity modulus around the tip-sample coupling zone (improved tip) for p-polarization: (a) in x - z plane, and (b) in y - z plane. Reprinted with permission from [363], G. W. Chern et al., *J. Appl. Phys.* 95, 1114 (2004). © 2004, American Institute of Physics.

light transmission from the tip apex is higher than that of the noncoated tip and the spot size is smaller than that of the metal-coated tip used alone. These results lead to the improvement of transmission and the decrease in the spot size of the light emerging from the tip apex. The light coming from the base of the objective lens (semispherical at the tip apex) is focused at output end of the tip apex in front of the sample surface. Because of the use of a semispherical lens at the tip apex, the focus spot at the hollow tip apex is expected to be smaller than that of the metal-coated tip used alone, thus causing a smaller spot emerging from the tip apex. Due to the small distance (about 15 nm) between the tip and sample, a smaller spot is produced. The spot size is reduced to 30 nm as shown in Figure 68. It exhibits the advantages of both high throughput light efficiency and small beam spot size, and yields a better type of tip pattern from the viewpoint of fabrication. Moreover, it is possible to reduce the recording marks below the laser beam spot by controlling the input beam power.

A novel probe structure combining a metallic probe with a local dielectric tip, and a structure using a semispherical lens at the tip apex were carried out. The phenomena of optical enhancement and beam confinement are due to the effect of surface atoms and plasmon resonances in the region of nanodimensions and leads to propagation mainly in forward direction, i.e., the dipole polarization on the surface of the aperture rim and the beam blocking by the metal film of the conic surface. We also verified the designs of field-enhancing

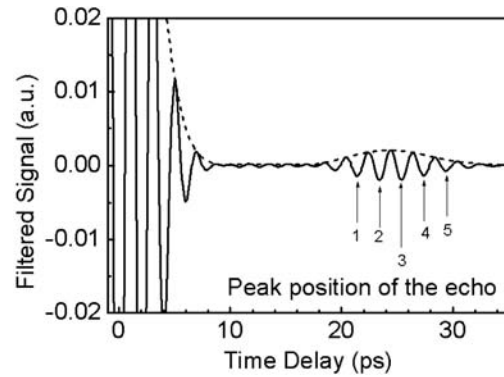


Figure 68. A demonstration of 1D nano-ultrasonic scans measurement. By resolving the acoustic echo signal, the thickness of thin nano film can be measured. Reprinted with permission from [365], G. W. Chern et al., *Phys. Rev. B* 67, 121303(R)-1 (2003). © 2003, The American Physical Society.

NSOM probes that are experimentally feasible and provided a suggestion for fabricating an optimal probe. Using the improved tips with a size of 30 nm, we can obtain a very small spot size of approximately the same dimensions as the tip apex. We expect this to bring the minimum line width less than 30 nm can be made by the processing technology of nano energy beam lithography with near-field optical fiber probe.

Piezoelectric semiconductor strained layers such as multiple quantum wells can be treated as piezoelectric transducers to generate nanometer-wavelength and THz-frequency acoustic waves. The mechanism of nano-acoustic wave (NAW) generation in strained piezoelectric layers, induced by femtosecond optical pulses, can be modeled by a macroscopic elastic continuum theory. The optical absorption change of the strained layers modulated by NAW through quantum-confined Franz-Keldysh (QCFK) effects allows optical detection of the propagating NAW. Based on these piezoelectric based optical principles, Sun and his coworkers [363–365] have designed an optical piezoelectric transducer (OPT) to generate NAW. The optically generated NAW is then applied to one-dimensional (1-D) ultrasonic scan for thickness measurement, which is the first step toward multi-dimensional nano-ultrasonic imaging (see Fig. 68). Launching a NAW pulse and resolving the returned acoustic echo signal with femtosecond optical pulses can measure the thickness of the studied layer measured with <1 nm resolution. This nano-structured OPT technique will provide the key toward the realization of “nano-ultrasonics,” which is analogous to the typical ultrasonic techniques but in a nanometer scale.

4. CONCLUSIONS

In this review, we have illustrated several methods to prepare nanoparticles including insulators, semiconductors, carbon nanotubes, and metals and magnetic ferrofluids. Aligned and random aligned carbon nanotubes grown on copper based iron alloys, respectively, by radio frequency induced self-bias hot-filament method and by microwave enhanced plasma CVD were specially illustrated. Temperature dependence on the field emission of CNTs is successfully expressed

by semiconductor thermionic emission theory. The physical properties of nanomaterials, comprising structure, electrical and magnetic characters, linear optical and nonlinear optical properties subjecting to classical size and quantum size effects are succinctly described. Nano-ferro fluids are illustrated to behave the unusual quantum phase transition. The dielectric constants of metallic nano-particles are measured within the microwave frequency ranges. Nanofabrication for tackling nanodevices are portrayed. It is impossible to meticulously display every detail of this newly developed complex system in this scenario review.

ACKNOWLEDGEMENTS

The author is indebted to his previous outstanding students Drs. C. C. Tzeng, S. Y. Chen, C. P. Pang, H. Y. Miao, J. H. Liu, C. L. Chen, H. T. Lue, C. S. Chen, C. T. Hsieh, W. C. Huang, C. S. Chang, R. W. Chang, and Y. C. Yeh, for their delicate and exhausted works on performing the theoretical and experimental approaches. Professors S. Gwo, C. K. Sun, T. J. Yang, and S. F. Fu, for providing their new fabrication method of nanotechniques in this review article are greatly appreciated. Copyright permission for producing part of the materials the author's papers published by Elsevier, American Scientific, American Physics Society, the Institute of Physics, International Union of Crystallography, IUCr journals, EDP Sciences, Springer-Verlag GmbH and World Scientific Publishers are acknowledged.

REFERENCES

- Gleiter, *Progress in Meter. Sci.* 33, 323 (1989).
- N. Wada, *Jap. JK. Appl. Phys.* 8, 551 (1969).
- K. Tanaka, K. Ishizaki, and M. Uda, *J. Mater. Sci.* 22, 2192 (1987).
- J. S. Haggerty, W. R. Cannon, and J. I. Steinfeld, "Laser Induced Chemical Process." Plenum Press, New York, 1981.
- A. Roosen and H. Hausner, "Ceramic Powders." Elsevier, Amsterdam, 1983.
- J. Eckert, J. C. Halzer, and C. E. Krill III, *J. Appl. Phys.* 73, 2794 (1993).
- S. K. Ma and J. T. Lue, *Solid State Commun.* 97, 979 (1996).
- W. Stober, A. Fink, and E. J. Bohn, *J. Colloid Interf. Sci.* 26, 62 (1968).
- S. P. Mukherjee, "Sol-Gel Technology for Thin Films, Fibers, Preforms, Rlctronics and Specialty Shapes" (I. C. Klein, Ed.). Noyes Pub., Park Ridge, New York, 1988.
- T. Lopez, J. Mendez, T. Z. Mudio, and M. Villa, *Mater. Chem. Phys.* 30, 161 (1992).
- R. F. Marzke and W. S. Glaunsinger, *Proceedings of the Symposium on the Characterization of Materials with Submicron Dimensions*, Philadelphia, (1983).
- R. V. Upadhyay, D. Srinivas, and R. V. Mehta, *J. Magn Magn. Mater.* 214, 105 (2000).
- V. K. Sharma and F. Waldner, *J. Appl. Phys.* 48, 4298 (1977).
- R. E. Cavicchi and R. H. Silsbee, *Phys. Rev. Lett.* 52, 1453 (1984).
- F. Frank, W. Schulze, B. Tesche, J. Urban, and B. Winter, *Surf. Sci.* 156, 90 (1985).
- L. C. Klein, "Sol-Gel Technology for Thin Films, fibers, Preforms, Electronics, and Specialty Shapes." Noyes Publications, 1988; C. J. Brinker and G. W. Scherer, "Sol-Gel Science." Academic Press, San Diego, 1990.
- M. J. Lochhead and K. L. Bray, *Chem. Mater.* 7, 572 (1995).
- W. Stober, A. Fink, and E. Bohn, *J. Colloid Interf. Sci.* 26, 62 (1968).
- G. H. Bogush and C. F. Zukoski, *J. Colloid Interf. Sci.* 142, 1 (1991).
- R. Mayoral, J. Requena, J. S. Moya, C. Lopez, A. Cintas, H. Miguez F. Meseguer, L. Vazquez, M. Holgado, and A. Blanco, *Adv. Mater.* 9, 257 (1997).
- B. Karmakar, G. De, and D. Ganguli, *J. Non-Cryst. Solids* 272, 119 (2000).
- C. E. Moran, G. D. Hale, and N. J. Halas, *Langmuir* 17, 8376 (2001).
- Y. Q. Lue, T. K. Ho, C. P. Pang, and J. T. Lue, *Nonlinear Optic. Mater.* 14, 93 (2005).
- D. Bimberg, M. Grundmann, and N. N. Ledensov, "Quantum Dot Heterostructures." John Wiley & Sons, New York, 2001.
- S. Fujita, S. Maruno, S. Miyazaki, and M. Hirose, *Appl. Phys. Lett.* 70, 2291 (1995).
- M. Komuro, H. Hiroshima, H. Tanou, and T. Kanayama, *J. Vac. Sci. Technol. B* 4, 98 (1983).
- T. Brnner, "Technical Digest of International Electron Devices Meeting." Washington, IEEE Catalog 97CH36103, IEEE, Picataway, 1997, p. 9.
- IBM, *J. Res. Develop.* 37, 288 (1993).
- V. A. Shchukin, A. I. Vorovkov, P. S. Kop'ev, and D. Binberg, *Phys. Rev. B* 51, 10104 (1995); et al., B51, 2968 (1995).
- R. Leon, T. J. Senden, C. Jagadish, and A. Clark, *Phys. Rev. Lett.* 4942 (1997).
- M. Kitamura, M. Nishiota, J. Oshinowo, and Y. Arakawa, *Appl. Phys. Lett.* 66, 3663 (1995).
- C. F. Chen, S. D. Tzeng, H. Y. Chen, and S. Gwo, *Optics Lett.* 30, 652 (2005).
- D. W. Johnson, *Am. Ceram. Soc. Bull.* 60, 221 (1981).
- J. L. Shi, J. H. Gao, and Z. X. Lin, *Solid State Ionics* 32/33, 537 (1989).
- A. Roosen and H. Hausner, "Ceramic Poeders." Elsevier, Amsterdam, 1983.
- J. T. Lue, W. C. Huang, and S. K. Ma, *Phys. Rev. B* 51, 14570 (1995).
- F. G. Cherkasov, A. Ya. Vitol, and M. F. Galyautdinov, *JETP Lett.* 49, 431 (1989).
- W. C. Huang and J. T. Lue, *Phys. Rev. B* 59, 69 (1999).
- S. Wang and J. Zhao, *Ferroelectrics* 154, 289 (1994).
- H. J. Williams, R. M. Bozorth, and W. Shockley, *Phys. Rev.* 75, 155 (1949).
- A. Sacco, Jr., P. Thacker, T. N. Chang, and T. S. Chiang, *J. Catal.* 85, 224 (1984).
- I. Stewart, M. J. Tricker, and J. A. Cairns, *J. Catal.* 94, 360 (1985).
- Y. Saito, *Carbon* 33, 979 (1995).
- A. Thess et. al., *Science* 273, 483 (1996).
- H. Kanzow and A. Ding, *Phys. Rev. B* 60, 11180 (1999).
- Kataura et. al., *Carbon* 38, 1691 (2000).
- A. Gorbunov, O. Jost, W. Pompe, and A. Graff, *Appl. Surf. Sci.* 197-198, 563 (2002).
- Y. C. Choi et al., *J. Appl. Phys.* 88, 4898 (2000).
- Ph. Buffat and J.-P. Borel, *Phys. Rev. A* 13, 2287 (1976).
- A. Gorbunov, O. Jost, W. Pompe, and A. Graff, *Appl. Surf. Sci.* 197-198, 563 (2002).
- T. Guo, P. Nikolaev, A. Thess, D. T. Colbert, and R. E. Smalley, *Chem. Phys. Lett.* 243, 49 (1995).
- M. J. Yacaman, M. M. Yoshida, L. Rendon, and J. G. Santiesteban, *Appl. Phys. Lett.* 62, 202 (1993); Z. F. Ran et al., *Science* 282, 1105 (1998).
- S. Y. Chen, H. Y. Miao, J. T. Lue, and M.S. Ouyang, *J. Phys. D.: Appl. Phys.* 37, 273 (2003).
- S. Y. Chen and J. T. Lue, *Phys. Lett. A* 309 114 (2003).
- S. Y. Miao, J. T. Lue, S. K. Chen, C. H. Tsau, and M. S. Ouyang, *Eur. Phys. J. Appl. Phys.* 29, 153 (2005).
- S. Y. Chen, L. W. Chang, C. W. Peng, H. Y. Miao, and J. T. Lue, *J. Nanosci. Nanotechnol.* 5, 1987 (2005); L. W. Chang and J. T. Lue, *ibid* 5, 1672 (2005).
- B. A. Korggel and D. Fitzmaurice, *Adv. Mater.* 10, 66 (1998).

58. M. Mertig, R. Kirtsch, and W. Pompe, *Appl. Phys. A* A66, S723 (1998).
59. B. A. Korggel and D. Fitzmaurice, *Adv. Mater.* 10, 66 (1998).
60. Morlaes, C. M. Lieber, *Semiconductor Nanowires Science* (1998)
61. M. Mertig, R. Kirtsch, and W. Pompe, *Appl. Phys. A* A66, S723 (1998).
62. S. Shingbara, O. Okino, Y. Sayama et al., *Jpn. J. Appl. Phys. Part I* 36, 7791 (1997).
63. D. P. Yu, Q. L. Hang, Y. Ding et al., *Appl. Phys. Lett.* 73, 3076 (1998).
64. G. W. Zhou, Z Zhang, D. P. Yu et al., *Appl. Phys. Lett.* 73, 677 (1998).
65. A. Uhliir, *Bell System Tech. J.* 35, 33 (1956).
66. D. R. Turner, *J. Electrochem. Soc.* 105, 402 (1958).
67. C. S. Chang and J. T. Lue, *Thin Solid Films* 259, 275 (1995); T. Z. Lin, Master Thesis, National Tsing Hua University, Materials Science Eng. Dep. (1997).
68. P. T. Liu, K. J. Chao, X. J. Guo et al., *J. Appl. Cryst.* 38, 211 (2005).
69. C. M. Yang, H. S. Sheu, and K. J. Chao, *Adv. Funct. Mater.* 12, 143 (2002).
70. D. Briggs and M. P. Seah, "Practical Surface Analysis by Auger and X-ray Photoelectron Spectroscopy." John Wiley & Sons, New York, 1983.
71. B. D. Cullty, "Elements of X-ray Diffraction." Addison Wiley, 1978, 2 Edn.
72. S. Y. Miao, J. T. Lue, S. K. Chen C. H. Tsau, and M. S. Ouyang, *Eur. Phys. J. Appl. Phys.* 29, 153 (2005).
73. M. S. Dresselhaus, G. Dresselhaus, and R. Saito, *Phys. Rev. B* 45, 6234 (1992).
74. S. J. V. Frankland and D. W. Brenner, *Chem. Phys. Lett.* 334 18 (2001).
75. S. J. Hans, J. Doerr, and R. F. Bunshah, *Thin Solid Films* 280, 256 (1996).
76. S. P. Bozeman, P. K. Baumann, M. J. Powers, J. J. Cuomo, R. J. Nemanich, and D. L. Dreifus, *Diamond Relat. Mater.* 5, 802 (1996).
77. K. Okano and K. K. Glwason, *Electron lett.* 35, 74 (1995).
78. R. H. Fowler and L. W. Nordheim, *Proc. Roy. Lond. A* 119, 173 (1928).
79. J. W. Glesener and A. A. Morrish, *Thin Solid Films* 290–291, 153 (1996).
80. J. W. Glesener and A. A. Morrish, *Appl. Phys. Lett.* 69, 785 (1996).
81. R. Gomer, "Field Emission and Field Ionization." Harvard University Press, 1961, p. 19.
82. Z. H. Huang, P. H. Cutler, N. M. Miskovsky, and T. E. Sullivan, *Appl. Phys. Lett.* 65, 2562 (1994).
83. R. G. Forbes, *J. Vac. Sci. Technol. B* 17, 526 (1999).
84. T. Sugino, K. Kuriyama, C. Kimura, Y. Yokota, S. Kawasaki, and J. Shirafuji, *J. Appl. Phys.* 86, 4635 (1999).
85. T. Sugino, K. Kuriyama, C. Kimura, and S. Kawasaki, *Appl. Phys. Lett.* 73, 268 (1998).
86. C. L. Chen, C. S. Chen, and J. T. Lue, *Solid State Electron.* 44, 1733 (2000).
87. C. S. Chen, C. L. Chen, and J. T. Lue, *Eur. Phys. J. A. P.* 11, 3 (2000).
88. J. T. Lue, *Solid State Electronics* 23, 263 (1980).
89. V. C. Bandis and B. B. Pate, *Phys. Rev. B* 52, 12056 (1995).
90. J. T. Lue, S. Y. Chen, C. L. Chen, and M. C. Lin, *J. Non-Cryst. Solids* 265, 230 (2000).
91. G. Zhou, W. Duan, B. Gu, and Y. Kawazoe, *Appl. Phys. Lett.* 80, 1999 (2002).
92. O. M. Kuttel, O. Groning, C. Emmenegger, and L. Schlappbach, *Appl. Phys. Lett.* 73, 113 (1998); A. M. Rao, E. Richter, S. Bandow et al., *Science* 275, 187 (1997).
93. L. Henrard, E. Hernandez, F. Bernier et al., *Phys. Rev.* 60, R8521 (1999).
94. D. L. Carroll, P. Redlich, P. M. Ajayan, J. C. Charlier, X. Blase, A. DeVita, and R. Car, *Phys. Rev. Lett.* 78, 2811 (1997).
95. K. A. Dean, P. von Allmen, and B. R. Chalamala, *J. Vac. Sci. Technol. B* 17, 1959 (1999).
96. G. Vitali, M. Rossi, M. L. Terranova, and V. Sessa, *J. Appl. Phys.* 77, 4307 (1995).
97. D. G. McCulloch, S. Praver, and A. Hoffman, *Phys. Rev. B* 50, 5905 (1994); V. Barbarossa, F. Galluzzi, R. Tomaciello, and A. Zanobi, *Chem. Phys. Lett.* 185, 53 (1991).
98. S. Y. Chen, H. Y. Miao, J. T. Lue, and M. S. Ouyang, *J. Phys. D: Appl. Phys.* 37, 273 (2004).
99. W. Li, H. Zhang, C. Wang, Y. Zhang, X. K. Zhu, and S. Xie, *Appl. Phys. Lett.* 70, 2684 (1997).
100. P. C. Eklund, J. M. Holden, and R. A. Jishi, *Carbon* 33, 959 (1995).
101. C. J. Lee, D. W. Kim, T. J. Lee, Y. C. Choi, Y. S. Park, W. S. Kim et al., *Appl. Phys. Lett.* 75, 1721 (1999).
102. L. J. Chen, J. H. Tyan, and J. T. Lue, *Phys. Chem. Solids* 55, 871 (1994).
103. G. Reiss, J. Vancea, and H. Hoffmann, *Phys. Rev. Lett.* 56, 2100 (1986).
104. T. Fujita, K. Ohshima, and T. Kuroishi, *J. Phys. Soc. Jpn.* 40, 90 (1976).
105. B. Roy and D. Chakravorty, *J. Phys. Condens. Matter* 2, 9323 (1990).
106. A. Chatterjee and D. Chakravorty, *Electrical, J. Mater. Sci.* 27, 4115 (1992).
107. W. C. Huang and J. T. Lue, *Phys. Rev. B* 59, 69 (1999); J. T. Lue, W. C. Huang, and S. K. Ma, *Phys. Rev. B* 51, 14570 (1995).
108. J. Kondo, "Solid State Physics" (H. Ehrenreich and Turnnbull, Eds.), Vol. 23, p. 184. Academic, New York, 1969.
109. G. R. Grimmett, "Percolation." Springer-Verlag, New York, 1989.
110. M. Stadermann, S. J. Papadakis, M. R. Falvo, J. Novak, E. Snow, Q. Fu, J. Liu, Y. Fridman, J. J. Boland, R. Superfine, and S. Washburn, *Phys. Rev. B* 69, 201402 (2004).
111. Z. K. Tang, H. D. Sun, and J. Wang, *Physica B* 279 200 (2000).
112. M. S. Fuhrer, A. K. L. Lim, L. Shih, U. Varadarajan, A. Zettl, and P. L. McEuen, *Physica E* 6, 868 (2000).
113. F. Wakaya, K. Katayama, and K. Gamo, *Microelectronic Engineering* 67–69, 853 (2003).
114. J. Appenzeller, R. Martel, V. Derycke, M. Radosaljevic, S. Wind, and D. Neumayer, *Ph. Avouris, Microelectronic Eng.* 64, 391 (2002).
115. G. Park, G. T. Kim, J. H. Jhang, and Y. W. Park, *Thin Solid Films* 393, 161 (2001).
116. K. Lin, M. Burghard, S. Roth, and P. Bernier, *Appl. Phys. Lett.* 75, 2494 (2000).
117. J. Lefebvre, R. D. Antonov, M. Radpsavljevic, J. F. Lynch, M. Liaguno, and A. T. Johnson, *Carbon* 38, 1745 (2000).
118. Y. Y. Wei and G. Eres, *Appl. Phys. Lett.* 76, 3759 (2000).
119. L. W. Chang and J. T. Lue, *J. Nanosci. Nanotechnol.* 5, 1672 (2005).
200. H. Haug and S. W. Koch, "Quantum Theory of the Optical and Electronic Properties of Semiconductors." World Scientific Publishers, Singapore, 1990.
201. J. H. Liu, C. L. Chen, H. T. Lue, and J. T. Lue, *IEEE Microwave Wireless Components* 13, 181 (2003).
202. Y. S. Yeh, J. T. Lue, and Z. R. Zheng, *IEEE trans. TMTT* 53, 1756 (2005).
203. J. T. Lue and Y. S. Hor, *J. Opt. Soc. Am. B* 6, 1103 (1989).
204. W. C. Huang and J. T. Lue, *Phys. Rev. B* 49, 17279 (1994).
205. W. C. Huang and J. T. Lue, *J. Phys. Chem. Solids* 58, 1529 (1997).
206. B. W. Hakki and P. D. Coleman, *IEEE Trans. Microwave Theory Technol.* 8, 402 (1960).
207. T. C. Choy, "Effective Medium Theory: Principles and Applications." Oxford University Press, New York, 1999.
208. D. M. Wood and N. W. Ashcroft, *Phys. Rev. B* 25, 6255 (1982).
209. J. T. Lue and C. S. Chang, *J. Nonlinear Phys. Mater.* 8, 503 (1999).
210. C. S. Chang and J. T. Lue, *Surface Science* 393, 231 (1997).
211. J. A. Hertz, *Phys. Rev. B* 14, 1165 (1976); M. A. Contentino, *ibid* 47, 11587 (1993); A. J. Millis, *ibid* 48, 7183 (1993).

212. S. A. Carter, T. F. Rosenbaum, J. M. Honig, and J. Spalek, *Phys. Rev. Lett.* 67, 3440 (1991); *Phys. Rev. B* 48, 16841 (1993).
213. H. V. Lohneysen, T. Pietrus, G. Portisch, H. G. Schlager, A. Schroder, M. Sieck, and T. Trappmann, *Phys. Rev. Lett.* 72, 3262 (1994); B. Bogenberger and H. V. Lohneysen, *ibid* 74, 1016 (1995).
214. M. B. Maple, C. L. Seaman, D. A. Gajewski, Y. Dalichaouch, V. B. Barbeta, M. C. de Andrade, H. A. Mook, H. G. Lukefahr, O. O. Berna, and D. E. MacLaughlin, *J. Low. Temp. Phys.* 99, 223 (1995).
215. S. Chakravarty, B. I. Halperin, and D. R. Nelson, *Phys. Rev. B* 39, 2344 (1989).
216. S. Sachdev and J. Ye, *Phys. Rev. Lett.* 69, 2411 (1992).
217. J. Miller and D. A. Huse, *Phys. Rev. Lett.* 70, 3147 (1993).
218. J. T. Lue, W. C. Huang, and S. K. Ma, *Phys. Rev. B* 51, 14570 (1995).
219. E. M. Chudnovsky and J. Tejada, "Macroscopic Quantum Tunneling of the Magnetic Moment." Cambridge, 1998, p. 94.
220. C. Paulsen, L. C. Sampaio, R. Tachoueres, B. Barbara, D. Fruchart, A. Marchand, J. L. Tholence, and M. Uehara, *J. Magn. Magn. Mater.* 116, 67 (1992).
221. X. X. Zhang, J. M. Hernandez, J. Tejada, and R. F. Ziolo *Phys. Rev. B* 54, 4101 (1996).
222. J. Tejada, L. Balcells, S. Linderth, R. Perzynski, B. Barbara, and J. C. Bacri, *J. Appl. Phys.* 73, 6952 (1993).
223. R. H. Kodama, C. L. Seaman, A. E. Berkowitz, and M. B. Maple, *J. Appl. Phys.* 75, 5639 (1994).
224. C. T. Hsieh, C. C. Liu, and J. T. Lue, *Appl. Surf. Sci.* 252, 1899 (2005).
225. R. H. Kodama, A. E. Berkowitz, E. J. McNiff, Jr., and S. Foner, *Phys. Rev. Lett.* 77, 394 (1996).
226. S. Sachdev, "Quantum Phase Transitions." Cambridge, 1999, p. 8.
227. C. T. Hsieh and J. T. Lue, *Phys. Lett. A* 36, 329 (2003).
228. A. Garvin and C. L. Chien, *J. Appl. Phys.* 67, 938 (1990).
229. G. Xiao, S. H. Liou, A. Levy, J. N. Taylor, and C. L. Chien, *Phys. Rev. B* 34, 7573 (1986).
230. V. K. Sharma and A. Baiker, *J. Chem. Phys.* 75, 5596 (1981); C. T. Hsieh, W. L. Huang, and J. T. Lue, *J. Phys. Chem. Solids* 63, 733 (2002).
231. R. S. de Biasi and T. C. Devezas, *J. Appl. Phys.* 49, 2466 (1978).
232. C. T. Hsieh and J. T. Lue, *European J. Phys. B* 35, 357 (2003); C. T. Hsieh and J. T. Lue, *Phys. Lett. A* 300, 636 (2002).
233. M. Stampanoni, A. Vaterlaus, M. Aeschlimann, and F. Meier, *Phys. Rev. Lett.* 59, 2483 (1987).
234. B. N. Engle, C. D. England, R. A. Van Leeuwen, M. H. Wiedemann, and C. M. Falco, *Phys. Rev. Lett.* 67, 1910 (1991).
235. F. J. A. de Broeder, D. Kuiper, A. P. Van de Mosselaer, and W. Hoving, *Phys. Rev. Lett.* 60, 2769 (1988).
236. G. Bochi, H. J. Hug, D. I. Paul, B. Stiefel, A. Moser, I. Parashikov, H.-J. Guntherodt, and R. C. O'Handley, *Phys. Rev. Lett.* 75, 1839 (1995).
237. L. Prejbeanu, L. D. Buda, U. Ebels, and K. Ounadjela, *Appl. Phys. Lett.* 77, 3066 (2000).
238. H. N. Lin, Y. H. Chiou, B. M. Chen, H. P. D. Shieh, and Ching-Ray Chang, *J. Appl. Phys.* 83, 4997 (1998).
239. M. Lohndorf, A. Wadas, H. A. M. van den Berg, and W. Wiesen-danger, *Appl. Phys. Lett.* 68, 3635 (1996).
240. H. S. Cho, C. Hou, M. Sun, and H. Fujiwara, *J. Appl. Phys.* 85, 5160 (1999).
241. L. J. Heyderman, H. Niedoba, H. O. Gupta, and I. B. Puchalska, *J. Magn. Magn. Mater.* 96, 125 (1991).
242. S. Chikazumi, "Physics of Magnetism, John-Wiley Series on the Science and Technology of Materials." New York, 1964, p. 238.
243. C. T. Hsieh and J. T. Lue, *Appl. Surf. Sci.* 252, 1899 (2005).
244. M. Pratzner, H. J. Elmers, M. Bode, O. Pietzsch, A. Kubertzka, and R. Wiesendanger, *Phys. Rev. Lett.* 87, 12701 (2001).
245. L. Berger, *J. Appl. Phys.* 49, 2156 (1978).
246. G. G. Cabrera and L. M. Falicov, *Phys. Status Solidi B* 61, 539 (1974).
247. T. Kimura, F. Wakaya, and K. Gamo, *J. Magn. Magn. Mater.* 236, 262 (2001).
248. A. O. Adeyeye, J. A. C. Bland, C. Daboo, Jaeyong Lee, U. Ebels, and H. Ahmed, *J. Appl. Phys.* 79, 6120 (1996).
249. K. Shigeto, T. Okuno, T. Shinjo, Y. Suzuki, and T. Ono, *J. Appl. Phys.* 88, 6636 (2000).
250. P. M. Levy and S. Zhang, *Phys. Rev. Lett.* 79, 5110 (1997).
251. U. Rüdiger and J. Yu, L. Thomas, S. S. S. P. Parkin, and A. D. Kent, *Phys. Rev. B* 59, 11914 (1999).
252. R. Danneau, P. Warin, J. P. Attané, I. Petej, C. Beigné, C. Fermon, O. Klein, A. Marty, F. Ott, Y. Samson, and M. Viret, *Phys. Rev. Lett.* 88, 157201-1~4, (2002).
253. B. Raquet, M. Viret, P. Warin, E. Sondergard, and R. Mamy, *Physica (Amsterdam)* 294B, 102 (2001).
254. A. B. Pippard, "Magnetoresistance in Metals." Cambridge University Press, Cambridge, 1989, pp. 212-236.
255. E. Koenigsberg, *Phys. Rev.* 91, 8 (1953).
256. H. T. Lue, J. T. Lue, and T. Y. Tseng, *IEEE Trans. Instrum. Meas.* 51, 433 (2002).
257. J. H. Liu, Y. C. Lin, J. T. Lue, and C. J. Wu, *Meas. Sci. Technol.* 13, 1 (2002).
258. L. Bonalde, B. D. Yanoff, M. B. Salamon, D. J. Harlingen, E. M. Chia, Z. Q. Mao, and Y. Macno, *Phys. Rev. Lett.* 85, 4775 (2000).
259. N. Chen, S. Tsai, and Jun Su, 87, 6911 (2000).
260. M. Tsutsumi and S. Tamura *IEEE Trans. Microw. Theory Tech.* 40, 400 (1992).
261. T. C. Edwards, "Foundations for Microstrip Circuit Design." John Wiley & sons, New York, 1983.
262. D. Spenato, A. Fessant, J. Gieraltowski, J. Loaec, and H. Legall, *J. Magn. Magn. Mater.* 140, 1979 (1995).
263. N. Vukadinovic, M. Labruno, J. Ben Youssef, A. Marty, J. C. Toussaint, and H. Le Gall, *Phys. Rev. B* 65 (2002).
264. Soshin Chikazumi, "Physics of Magnetism" (S. H. Charap, English Ed.), p 338. (1966).
265. George Rado, "Magnetism." Academic press, Vol. 1, p. 465.
267. B. Heinrich, "Ultrathin Magnetic Structure." Springer-Verlag, Berlin, 1994, p. 216.
268. C. Kittel, "Introduction to Solid State Physics." John Wiley & Sons, New York, 1986, p. 480, 6th edn.
269. S. Chikazumi, "Physics of Magnetism" (Stanley H. Charap, Ed.), p. 138. (1966).
270. H. A. Wheeler, *IEEE Trans. MTT-25*, 631 (1977).
271. W. J. Getsinger, *IEEE Trans. MTT-21*, 34 (1973).
272. M. Kobayashi, *IEEE Trans. Microwave Theory Tech.* MTT-30, 2057 (1982).
273. R. A. Pucel et al., *IEEE trans. MTT*, MTT-16, 342 (1968).
274. S. W. Chang, J. H. Liu^a, and J. T. Lue, *Meas. Sci. Technol.* 14, 583 (2003).
275. A. Dubey, etc., *Electron. Lett.* 37, 1296 (2001).
276. W. P. Halperin, *Rev. Modern Phys.* 58, 533 (1986).
277. W. C. Huang and J. T. Lue, *J. Chem. Solids* 58, 1529 (1997).
278. J. T. Lue, W. C. Huang, and S. K. Ma, *Phys. Rev. B* 51, 14570 (1995).
279. K. Y. Lo and J. T. Lue, *Phys. Rev. B* 51, 2467 (1995).
280. W. C. Huang and J. T. Lue, *Phys. Rev. B* 59, 69 (1999).
281. Berger, J. Kliava, J. C. Bissey, and V. Baietto, *J. Appl. Phys.* 87, 7389 (2000).
282. L. Zhang, G. C. Papaefthymiou, and J. Y. Ying, *J. Appl. Phys.* 81, 6892 (1997).
283. J. Szczyrbowski, K. Schmalzbauer, and H. Hoffmann, *Phys. Rev. B* 32, 763 (1985).
284. Y. S. Hor and J. T. Lue, *Surf. Sci.* 304, 375 (1994).
285. L. Genzel, T. P. Martin, and U. Kreibig, *Z. Phys. B* 21, 339 (1975).
286. A. Kawabata and R. Kubo, *J. Phys. Soc. Jpn.* 21, 1765 (1966).
287. M. Fujii, T. Nagareda, S. Hayyashi, and K. Yamamota, *Phys. Rev. B* 44, 6243 (1991).
288. R. H. Doremus, *J. Chem. Phys.* 40, 2389 (1964).

289. R. H. Doremus, *J. Chem. Phys.* 42, 414 (1965).
290. B. B. Dasgupta and R. Fuchs, *Phys. Rev. B* 24, 554 (1981).
291. K. P. Charle, W. Schultz, and b. Winter, *Z. Physics, D* 12, 471 (1989).
292. R. W. Boyd, "Nonlinear Optics Academic." San Diego, 1992, p. 148.
293. J. J. Maki, M. S. Malcuit, J. E. Sipe, and R. W. Boyd, *Phys. Rev. Lett.* 67, 972 (1991).
294. J. N. Hodgson, "Optical Absorption and Dispersion in Solids." Chapman and Hall Ltd., London, 1970.
295. H. Raether, "Surface Plasmons on Smooth and Roughing Surfaces and on Gratings." Springer-Verlag, Heiderberg, 1986.
296. R. H. Doremus, *J. Chem. Phys.* 42, 414 (1965).
297. W. C. Huang and J. T. Lue, *Phys. Rev. B* 49, 17279 (1994).
298. N. H. March, "Theory of the inhomogeneous Electron Gas" (S. Lundqvist and N. H. March, Eds.). Plenum Press, New York, 1983.
299. M. Born and E. Wolf, "Principles of Optics." Pergamon Press, London, 1980, pp. 633-644.
300. A. A. Lushnikov and A. J. Simonov, *Z. Physic* 270, 17 (1974).
301. K. P. Charles, W. Schultz, and B. Winter, *Z. Physics D* 12, 471 (1989).
302. A. Smithard, *Solid State Commun.* 14, 407 (1974).
303. M. A. Smithard and M. Q. Tran, *Hebv. Physics Acta* 46, 869 (1974).
304. P. Apell and A. Ljungbert, *Solid State Commun.* 44, 1367 (1982).
305. N. D. Lang, *Phys. Rev. B* 4, 4234 (1971).
306. W. Eekardt. D. B. Tran Thai, F. Frank, and W. Schulze, *Solid State Commun.* 46, 571 (1983).
307. C. S. Chang and J. T. Lue, *Thin Solid Films* 259, 275 (1995).
308. G. J. Davies and D. Williams, "The Technology and Physics of Molecular Beam Epitaxy" (E. H. C. Parker, Ed.), Chap. 2. Plenum, NY, 1985.
309. C. P. Pang, C. T. Hsieh, and J. T. Lue, *J. Phys. D: Appl. Phys.* 36, 1764 (2005).
310. C. H. Kao and J. T. Lue, *Appl. Phys. A* 64, 439 (1997).
311. M. Abe and M. Gomi, *Jpn. J. Appl. Phys.* 23, 1580 (1984).
312. S. Taketomi, *Jpn. J. Appl. Phys.* 22, 1137 (1983).
313. M. Rasa, *J. Magn. Mater.* 201, 170 (1999).
314. C. P. Pang and J. T. Lue, *Appl. Phys. A* 81, 561 (2005).
315. R. Murphy, M. Yeganeh, K. J. Song, and E. W. Plummer, *Phys. Rev. Lett.* 63, 318 (1989)
316. C. C. Tzeng and J. T. Lue, *Phys. Rev. A* 39, 191 (1989).
317. J. Rudnick and E. A. Stern, *Phys. Rev. B* 4, 4274 (1971).
318. A. Chizmeshya and E. Zaremba, *Phys. Rev. B* 37, 2805 (1988)
319. C. S. Chang and J. T. Lue, *Surf. Sci.* 393, 231 (1997).
320. S. S. Jha and C. S. Warke, *Phys. Rev.* 153, 751 (1967).
321. J. C. Quial and H. J. Simon, *J. Appl. Phys.* 56, 2589 (1984).
322. J. C. Quial and H. J. Simon, *J. Appl. Phys.* 56, 2589 (1984).
323. C. H. Kao and J. T. Lue, *J. Nonlinear Opt. Phys. Mater.* 7, 497 (1998).
324. C. K. Chen, A. R. de Castro, and Y. R. Shen, *Phys. Rev. Lett.* 46, 145 (1981).
325. J. T. Lue and C. S. Chang, *J. Nonlinear Opt. Phys. Mater.* 8, 503 (1999).
326. K. Y. Lo and J. T. Lue, *Phys. Rev. B* 51, 2467 (1995).
327. A. A. Aktsipetrov, I. M. Baranova, E. M. Dubinina, S. S. Elovikov, P. V. Elyutin, D. A. Nikullin, and N. N. Fominykh, *Phys. Lett. A* 117, 239 (1986).
328. K. Fukumi, A. Chauahara, K. Kadono, T. Sakaguchi.,Y. Horino, M. Miya, K. Fujii, J. Hayakawa, and M. Satou, *J. Appl. Phys.* 75, 3075 (1994).
329. S. Janz, K. Pedersen, and H. M. van Driel, *Phys. Rev. B* 44, 3943 (1991).
330. A. V. Petukhov and A. Liebsch, *Surf. Sci.* 294, 381 (1993).
331. J. E. Sipe, D. J. Moss, and H. M. van Driel, *Phys. Rev. B* 35, 1129 (1987).
332. T. F. Heinz, "Nonlinear Surface Electromagnetic Phenomena" (H. E. Ponath and G. I. Stegeman, Eds.), p. 353. Elsevier, Amsterdam, 1991.
333. J. T. Lue, K. Y. Lo, and C. C. Tzeng, *IEEE J. Quantum Electron.* 38, 302 (1992).
334. J. T. Lue and C. Dai, *Phys. Rev. B* 47, 13653 (1993).
335. F. R. Aussenegg, A. Leitner, and H. Gold, *Appl. Phys. A* 60, 95 (1995).
336. C. S. Chen, J. T. Lue, C. L. Wu, S. G. Gwo, and K. Y. Lo, *J. Phys. Condens. Mater.* 15, 6537 (2003).
337. I. L. Lyubchanskii, N. N. Dadoenkova, M. I. Lyubchanskii, Th. Rasing, Jae-W. Jeong, and S.C. Shin, *Appl. Phys. Lett.* 76, 1848 (2000).
338. S. V. Govorkov, V. I. Emel'yanov, N. I. Koroteev, G. I. Petrov, I. L. Shumay, and V. V. Yakolev, *J. Opt. Soc. Am. B* 6, 1117 (1989).
339. J. Y. Huang, *Jpn. J. Appl. Phys.* 33, 3878 (1994).
340. F. R. Aussenegg, A. Leitner, and H. Gold, *Appl. Phys. A* 60, 95 (1995).
341. I. L. Lyubchanskii, N. N. Dadoenkova, M. I. Lyubchanskii, Th. Rasing, Jae-W. Jeong, and S. C. Shin, *Appl. Phys. Lett.* 76, 1848 (2000).
342. S. V. Govorkov, V. I. Emel'yanov, N. I. Koroteev, G. I. Petrov, I. L. Shumay, and V. V. Yakolev, *J. Opt. Soc. Am. B* 6, 1117 (1989).
343. K. Y. Lo and J. T. Lue, *Phys. Rev. B* 51, 2467 (1995).
344. A. M. Malvezzi, M. Allione, M. Patrini, A. Stella, P. Cheyssac, and R. Kofman, *Phys. Rev. Lett.* 89, 087401 (2002).
345. C. S. Chen and J. T. Lue, *European Phys. J. B* 46, 367 (2005).
346. K. Liu, Ph. Avouris, J. Bucchignano, R. Martel, and S. Sun, *J. Michl. Appl. Phys. Lett.* 80, 865 (2002).
347. Y. Takahashi, Y. Ono, A. Tujiwara, and H. Inokawa, *J. Phys. Condens. Matter* 14, R995 (2002).
348. S. F. Hu, G. J. Hwang, Y. P. Fang, Z. Y. Pan, and Y. C. Chou, *Chinese J. Phys.* 42, 636 (2004).
349. S. F. Hu, K. D. Huang, Y. M. Wan, and C. L. Sung, *Appl. Phys. Lett.* 85, 3893 (2004).
350. Y. C. Chou, and Y. P. Fang, Gwo-Jen Hwang, and S. F. Hu, *Appl. Phys. Lett.* (2005/06), submitted.
351. Z. Y. Yu, T. Masuzawa, and M. Fujino, *Annals CIRP* 47, 169 (1998).
352. K. Egashira and T. Masuzawa, *Annals CIRP* 48, 131 (1999).
353. D. Y. Sheu and T. Masuzawa, *Inter. J. Electrical Machining* 8, 15 (2003).
354. H. Y. Miao, J. T. Lue, and M. S. Ouyang, *J. Nanosci. Nanotechnol.* (2005), in press.
355. E. Betzig, J. Trautman, R. Wolfe, E. Gyorgy, P. Finn, M. Kryder, and C. Chang, *Appl. Phys. Lett.* 61, 142 (1992).
356. Y. Martin, S. Rishton, and H. Wickramasinghe, *Appl. Phys. Lett.* 71, 1 (1997).
357. F. Issiki, K. Ito, K. Etoh, and S. Hosaka, *Appl. Phys. Lett.* 76, 804 (2000).
358. T. Yatsui, M. Kouroggi, K. Tsutsui, M. Ohtsu, and J. Takahashi, *Opt. Lett.* 25, 67 (2000).
359. H. Yoshikawa, Y. Andoh, M. Yamamoto, K. Fukuzawa, T. Tamamura, and T. Ohkobo, *Opt. Lett.* 25, 1296 (2000).
360. B. D. Terris, H. J. Mamin, and D. Rugar, *Appl. Phys. Lett.* 68, 141 (1995).
361. B. D. Terris, H. J. Mamin, and D. Rugar, *Appl. Phys. Lett.* 65, 388 (1994).
362. Y. F. Chau, T. J. Yang, and D. P. Tsai, *Jap. J. Appl. Phys.* 43, 8115 (2004).
363. G. W. Chern, K.-H. Lin, and C.-K. Sun, *J. Appl. Phys.* 95, 1114 (2004).
364. C. L. Hsieh, K.-H. Lin, S. B. Wu, C.-C. Pan, J. I. Chyi, and C. K. Sun, *Appl. Phys. Lett.* 85, 4735 (2004).
365. G. W. Chern, K.-H. Lin, Y.-K. Huang, and C. K. Sun, *Phys. Rev. B* 67, 121303(R)-1 (2003).